Doctoral Dissertation

Extended Isogeometric Analysis for Structure Sensing and Anisotropic Hardening Material Model

Thein Lin Aung

June 2023

Department of Naval Architecture and Ocean Engineering
Division of Global Architecture
Graduate School of Engineering
Osaka University

A Dissertation for Doctor of Engineering Degree submitted to

Osaka University

Graduate School of Engineering

Division of Global Architecture

Department of Naval Architecture and Ocean Engineering

in

June 2023

Supervised by

Professor Ninshu Ma

Thesis review committee

1. Professor Ninshu Ma (Chair)
   Joining and Welding Research Institute,
   Graduate School of Engineering, Osaka University
2. Professor Kazuhiro Iijima
   Department of Naval Architecture and Ocean Engineering,
   Graduate School of Engineering, Osaka University
3. Professor Naoki Osawa
   Department of Naval Architecture and Ocean Engineering,
   Graduate School of Engineering, Osaka University

Abstract

Isogeometric analysis (IGA) is a computational method that uses the same basis functions for both geometry and analysis. In particular, non-uniform rational B-Spline (NURBS) functions which are common in computer-aided design (CAD) are used to represent the solution fields. This allows for a seamless transfer of geometry data to numerical analysis. First invented by Hughes et al. in 2005, IGA has been widely applied in various engineering fields such as structural analysis, fluid dynamics and electromagnetism due to its high efficiency. But the study and application of IGA in the field of structural health monitoring (SHM) is still in its infancy.

SHM is a process of monitoring the real-time structural state using on-site sensors, data processing and numerical algorithms. Unlike non-destructive testing (NDT) which usually requires human expertise, SHM relies on permanently mounted sensors and digital models to continuously analyze the operational conditions. Among the types of sensors used in SHM, fiber optic sensors are gaining popularity due to their small size, high sensitivity, ease of use and immunity to electromagnetic interference. Distributed fiber optic sensors (DFOS) use laser light and backscattering phenomena to detect strain and temperature along the entire length of the fiber. The length of the fiber can be up to tens of kilometers and the spatial resolution can be as small as a few centimeters, which makes DFOS an excellent choice for distributed sensing. But the sensing system needs to be paired with a digital model to calculate useful information from the raw data.

Inverse sensing is a process of using sensor data to estimate unknown parameters of the structure such as deformation, stress distribution or loading conditions. In the first part of this thesis, an inverse sensing method of IGA and DFOS is developed to combine the efficiency of IGA and versatility of DFOS in an integrated framework. The method consists of two components: the fiber model to represent the properties of DFOS fiber, and the formulation to solve the inverse problem. The fiber model is based on the parametric NURBS geometry and strain projection equations are derived to map the surface strains to one-dimensional fiber strains. The properties of the fiber model are validated with a numerical model and simulated fiber strains are compared with

experiment data. A case study to estimate loading conditions from measured fiber strains is also presented.

The analytical formulation of inverse IGA is derived from the least-squares functional and minimum strain energy principle. The resulting equations are used to solve unknown displacement and stress fields from input fiber strains for linear elastic structures. The proposed formulation is validated with four numerical examples and then sensitivities on sampling resolution and measurement noise are investigated. Finally, the method is applied to an experimental model of a rotating impeller plate.

Accurate material modelling is essential for large deformation analysis such as metal forming or automobile crash simulations. The second part of the thesis focuses on the nonlinear material modelling for elastoplastic IGA. Specifically, the mechanical response of high strength steel DP980 after it was subjected to prestrain is experimentally studied. The observed history-dependent anisotropic hardening behavior is modelled with an empirical formula and implemented as a constitutive model in IGA. The model is validated with numerical simulations and comparison with experiment data. The proposed methodologies in this thesis are implemented in the in-house IGA code JWRIAN-IGA and as user-subroutines for commercial software LS-DYNA.

Contents

1 Introduction **1**

1.1 Background 1

1.1.1 Geometry and analysis 1

1.2 Distributed Sensing and Structural Monitoring 3

1.2.1 Integration of IGA and DFOS 4

1.3 Nonlinear Material Models 6

1.4 Structure of the Thesis 6

2 Theory and Development of Isogeometric Analysis **8**

2.1 Geometry representation 8

2.2 Coordinate systems 9

2.3 Basis functions and their derivatives 11

2.4 IGA mesh and refinement 13

2.4.1 Knot vectors 13

2.4.2 Mesh refinement 14

2.4.3 Applying boundary conditions 15

2.5 Linear elastic IGA 17

2.6 Coupling of multi-patch geometries 19

2.7 Summary 21

3 Integration of IGA and Distributed Fiber Optic Sensing **22**

3.1 Introduction 22

3.2 Development of Fiber Mesh Model for IGA 22

3.2.1 Fiber curve 23

3.2.2 Conversion from strain tensor to fiber strains 24

3.2.3 Validation of the numerical code 25

3.2.4 Merits of Integrated IGA-DFOS 28

3.3 Application of Integrated IGA and DFOS 29

3.3.1 Experimental setup 29

3.3.2 Experimental procedure . . . 30
3.3.3 Experimental results . . . 31
3.3.4 Simulation model . . . 32
3.4 Results and Discussion . . . 33
3.5 Estimation of loading conditions from DFOS measurements . . . 34
3.6 Summary . . . 37

4 Development of Inverse IGA for Structural Monitoring 39
4.1 Introduction . . . 39
4.1.1 Inverse Finite Element Method . . . 40
4.1.2 Drawbacks of iFEM, IGA as savior . . . 41
4.1.3 Proposed method . . . 41
4.2 Formulation of Inverse IGA-DFOS . . . 42
4.2.1 Revisiting DFOS fiber mesh model . . . 42
4.2.2 Least-squares objective . . . 42
4.2.3 Isogeometric least-squares fit . . . 43
4.3 Validation of Inverse IGA-DFOS with Simulated Examples . . . 44
4.3.1 Plate under twisting load . . . 45
4.3.2 Plate under bending load . . . 48
4.3.3 Pinched hemisphere . . . 49
4.3.4 Pinched cylinder . . . 51
4.4 Sensitivity analysis . . . 54
4.4.1 Sensitivity to sampling interval . . . 55
4.4.2 Sensitivity to noise . . . 57
4.5 Application of inverse IGA-DFOS to an impeller plate . . . 57
4.5.1 Experimental setup . . . 57
4.5.2 Experimental Results . . . 60
4.5.3 Inverse IGA Model . . . 61
4.5.4 Results and Discussion . . . 61
4.6 Summary . . . 66

5 Extension of IGA for Nonlinear Material Models 68
5.1 Introduction . . . 68
5.2 Mechanical properties of the raw material . . . 68
5.3 Uniaxial Tensile Tests of Prestrained Specimens . . . 70
5.3.1 Experiment results . . . 72
5.4 Development of Prestrain Induced Anisotropic Hardening Model . . . 74
5.4.1 Derivation of g and n^* . . . 74
5.4.2 Input parameters . . . 76

5.4.3 2D plane stress condition 76
5.5 Validation of the Material Model with Simple Nonlinear IGA 79
5.6 Results and Discussion 80
5.6.1 Simulation time history for LC configuration 80
5.6.2 Simulation time history for LL configuration 80
5.6.3 Comparison with experiments 80
5.6.4 Intermediate reloading angles 82
5.7 Summary 83

6 Conclusions and Outlook **85**
6.1 Conclusions 85
6.2 Outlook 87

Appendices **89**

A Integration of IGA and DFOS **89**
A.1 Modelling of DFOS fiber 89
A.2 Inverse analysis of the impeller plate 89

Publications **106**

Acknowledgments **107**

List of Figures

1.1 Decomposition of the time required for a typical FEM analysis 2
1.2 A simple example of IGA and FEM meshes 3
1.3 Block diagram of remote structural monitoring by DFOS and IGA 5

2.1 An example of a parametric spline curve 9
2.2 Coordinate systems and mappings 10
2.3 Parametrization for a bivariate surface 13
2.4 Illustration of 2D h-refinement 15
2.5 Different displacements of control points and geometry 16
2.6 Illustration of patch coupling 20

3.1 A second order NURBS curve showing control points and tangent vectors . 23
3.2 Illustration of fiber strain sampling points with sampling interval Δs . . . 25
3.3 Simple validation model for fiber strain calculation 26
3.4 Analytical fiber strains from uniform strain ε_{xx} 27
3.5 Fiber strains from biaxial strain $\varepsilon_{xx} = 100\,\mu\varepsilon$ and $\varepsilon_{yy} = -30\,\mu\varepsilon$. 27
3.6 Fiber strains from pure shear $\varepsilon_{xy} = 100\,\mu\varepsilon$. 28
3.7 Schematics of experiment setup 30
3.8 The pipe dimensions and experiment setup showing optical fiber, displacement sensors and threaded rod 30
3.9 Fiber strain measurement data from experiments 31
3.10 Response of fiber strains on applied displacement to the pipe 32
3.11 Pipe geometry and control points, IGA mesh, and fiber curve 32
3.12 Idealized Boundary conditions for the pipe model 33
3.13 Normal strains distributions on the pipe from IGA 34
3.14 (PVC pipe) Comparison of fiber strains for $u_x = 534\,\mu\mathrm{m}$ 34
3.15 (PVC pipe) Comparison of fiber strains for $u_x = 755\,\mu\mathrm{m}$ 35
3.16 Parametrization of pressure distribution on the PVC pipe 35
3.17 Optimized pressure distribution along the pipe 36

3.18 Fiber strains reproduced using the optimized pressure distribution 37

4.1 Illustration of plate twisting problem 45
4.2 Solutions of plate twisting problem 46
4.3 Comparison of fiber strains for plate twisting problem 47
4.4 Illustration of plate bending problem 48
4.5 Comparison of fiber strains for plate bending problem 49
4.6 Solutions of the plate bending problem 50
4.7 Distribution of stress-XX and stress-YY errors for the plate bending problem. 50
4.8 Illustration of the pinched hemisphere problem 51
4.9 Solutions of the pinched hemisphere problem 52
4.10 Illustration of the pinched cylinder problem 52
4.11 Solutions of the pinched cylinder problem 53
4.12 Sensitivity analysis of errors with respect to sampling interval 56
4.13 Sensitivity analysis of errors with respect to noise 58
4.14 Experimental setup of the mixer 59
4.15 Dimensions of the impeller plate 59
4.16 Fiber strain difference for the case with viscosity $5800\,\mathrm{mPa\,s}$ at $60\,\mathrm{RPM}$ . . 61
4.17 Fiber strains at the same positions on the front and back sides of the plate 62
4.18 CAD model of the impeller plate and fiber geometry 62
4.19 Deformation profiles from the inverse IGA-DFOS for variable RPMs (viscosity = $5800\,\mathrm{mPa\,s}$) 64
4.20 Experimental and reproduced fiber strains from inverse analysis for viscosity $5800\,\mathrm{mPa\,s}$ and $40\,\mathrm{RPM}$. 65
4.21 X-Stress contours from the inverse IGA-DFOS for viscosity $5800\,\mathrm{mPa\,s}$ and $40\,\mathrm{RPM}$. 65

5.1 Shear test specimen 68
5.2 Shear stress-strain and corresponding equivalent stress-strain curves . . . 69
5.3 Uniaxial stress-strain curves of the raw material 70
5.4 Preparation of prestrained specimens 71
5.5 Stress-strain curves of prestrained samples 72
5.6 Schematic illustration of reloading curves and model parameters 75
5.7 Validation model, boundary conditions and loading histories 79
5.8 Simulation results for 5LC case 81
5.9 Simulation results for 5LL case 81
5.10 Comparison of S-S curves from the experiments and simulation results . . 82
5.11 Tensile test specimens in 45° and 60° to 5L prestrain direction 83

5.12 Simulation and experimental reloading curves for $45°$ and $60°$ reloading directions after $5\,\%$ L-prestrain 83

A.1 Flow chart for the calculation of fiber strains from IGA linear elastic analysis 90
A.2 Simulated fiber strain distributions for pure tensile strain and pure shear strain states 91
A.3 Fiber strains from PVC pipe ovalization experiment for M1, M2 and M5 load cases 92
A.4 Measured fiber strains from the impeller experiment at fixed viscosity ($5800\,\mathrm{mPa\,s}$) and different RPMs. 93
A.5 Measured fiber strains from the impeller experiment at $40\,\mathrm{RPM}$ and different viscosities. 93
A.6 Deformation profiles from the inverse IGA-DFOS for variable viscosities at $40\,\mathrm{RPM}$. 94

List of Tables

3.1 Comparison of DFOS and strain gauges 28
3.2 Measurement parameters in the experiment 30
3.3 Comparison of errors between uniform and optimized loading conditions . 37

4.1 Error matrices for the numerical examples with pure fiber strain inputs . . 55

5.1 Mechanical properties of JSC980YL steel 69
5.2 Parameters of the reference curve and initial stress ratios 70
5.3 Measured elongation and equivalent plastic strain values after prestraining 70
5.4 Designation of experiment cases 71
5.5 Fitted parameters for the anisotropic hardening model 76

Nomenclature

$\bar{\sigma}$	Equivalent stress
$\bar{\varepsilon}_p$	Equivalent plastic strain
β	Nitsche penalty parameter for weak coupling
$\boldsymbol{\sigma}$	Stress vector (Voigt notation)
$\boldsymbol{\varepsilon}$	Strain vector (Voigt notation)
$\boldsymbol{\xi}$	Vector of parametric coordinates
$\boldsymbol{B}$	Strain-displacement matrix
$\boldsymbol{b}$	Body force vector
$\boldsymbol{c}$	Coordinate vector of a univariabe NURBS curve
$\boldsymbol{C}_i$	Coordinate vector of i^{th} control point
$\boldsymbol{D}$	Elasticity matrix
$\boldsymbol{d}$	Discretized displacement vector on control points
$\boldsymbol{e}_{pre}$	Unit vector along the prestrain direction
$\boldsymbol{e}_r$	Unit vector along the reloading direction
$\boldsymbol{f}$	Global force vector
$\boldsymbol{f}_e$	Element force vector
$\boldsymbol{h}$	Traction force vector
$\boldsymbol{K}$	Global stiffness matrix
$\boldsymbol{K}_c$	Matrix of Nitsche coupling coefficients
$\boldsymbol{K}_e$	Element stiffness matrix
$\boldsymbol{N}$	Basis function matrix

$\boldsymbol{s}$	Coordinate vector of a NURBS surface
$\boldsymbol{t}(s)$	Tangent vector of fiber curve at sampling point s
$\boldsymbol{u}$	Displacement vector of continuum
$\boldsymbol{v}$	Coordinate vector of a NURBS volume
Δs	Fiber strain sampling interval
δ	Prestrain activation factor (1 or 0 depending on the relative directions of prestrain and reloading)
Γ	Boundary of the physical domain
γ	moving average weight function of fiber strains
Γ_e	Boundary of e^{th} element
λ	Penalty parameter for the least-squares constraint of fiber strains
Ω	Physical domain of the structure
Ω_e	Physical domain of e^{th} element
$\overline{\varepsilon}_f$	Moving averaged fiber strains
Π	Total potential energy of the system
$\sigma^0(\bar{\varepsilon}_p)$	Reference stress-strain curve
σ^*, ε^*	Reloading yield stress and reloading plastic strain
$\sigma_{sat}, \varepsilon_{sat}$	Saturation stress and saturation strain of the reloading curve
$\sigma^y_{xx}(\bar{\varepsilon}_p), \sigma^y_{yy}(\bar{\varepsilon}_p), \sigma^y_{xy}(\bar{\varepsilon}_p)$	Stress-strain curves in material orthotropy axes
ε_f	One-dimensional fiber strains
ε_{pre}	Prestrain $\equiv$ equivalent plastic strain after prestraining
ξ, η, ζ	Parameteric direction or parameter value
Ξ, H, Z	Knot vectors in ξ, η, ζ direction respectively
e^r_f	relative root-means-square error of fiber strains
e^{RMS}_f	root-means-square error (RMSE) of fiber strains
e^r_u	relative root-means-square error of displacements
e^{RMS}_u	root-means-square error of displacements
K, ε_0, n	Swift hardening parameters of the reference curve

n, m, l	Number of basis functions in ξ, η, ζ direction respectively. n can also denote the total number of basis functions.
n^*, g	Coefficients of the reloading stress-strain curve after prestrain
N_i	(Univarite) basis function of index i
N_i, M_i, L_i	Univariate basis functions; N_i can also denote a basis functions without explicit cardinality.
n_s	number of fiber strain sampling points
p, q, r	Order of basis functions in ξ, η, ζ direction respectively
R_x, R_y, R_{xy}	Initial yield stress ratios
R_{sat}	Saturation stress ratio ($\sigma^*_{sat}/\sigma_{raw}$)
R_{xx}, R_{yy}	Yield stress ratios with respect to the reference stress-strain curve
Y_r	Ratio of yield stress between the reference stress-strain curve and actual yield stress after prestrain
s	fiber coordinate/sampling location

Chapter 1

Introduction

1.1 Background

1.1.1 Geometry and analysis

The Finite Element Method (FEM) is a crucial tool for numerical analysis in various fields such as solid mechanics, fluid mechanics, heat transfer, electromagnetism, and so on. It involves developing a mathematical model of the physical system based on fundamental laws of nature and verification with experimental data. The model is expressed as partial differential equations (PDEs) or boundary value problems (BVPs) that describe the system's behavior. However, solving these equations analytically is often complex or impossible for general cases and hence numerical methods are employed. FEM discretizes the system into smaller constituents called elements, which follow simpler equations compared to the parent domain [1]. The contributions of these elements are combined into a global system of equations that are solved to obtain the solutions. This allows for the approximation of the continuum from the discretized variables.

The development of the Finite Element Method and its variants dates back to the late 19^{th} century for aerospace applications and later expanded into other engineering fields. Nowadays, FEM is used as an analysis tool in conjunction with other tools in Computer Aided Engineering (CAE) workflow for the design cycle and/or maintenance after construction. Another essential tool in engineering is the Computer Aided Design (CAD), which helps in conceptualization, geometrical modeling, assembly and refining designs. Historically, CAD and FEM have evolved separately and only recently, some software packages include both in the same suite although they are still separate programs [2]. To represent and store geometries, CAD uses a variety of parametric and non-parametric forms such as primitive shapes, boundary representation (B-Rep), Non-uniform Rational

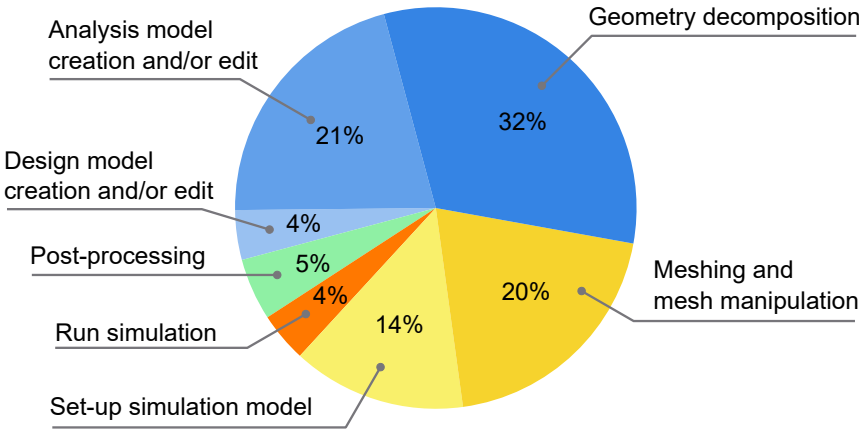

Figure 1.1: Decomposition of the time required for a typical FEM analysis. The preprocessing of geometry and mesh takes up a significant portion. [4]

B-Splines (NURBS) and trimmed surfaces. On the other hand, FEM uses shape functions to describe the geometry of elements, the most commonly used shape functions being Lagrange polynomials. An FEM "mesh" includes the positions of nodes and how they are connected together to form elements. The differences in geometry representation between CAD and FEM systems require conversions and preprocessing to create analysis meshes which can be tedious and time-consuming. In fact, the preprocessing step usually takes up a significant portion of the analysis time as shown in Fig. 1.1 and can create bottlenecks in the process, especially when multiple design iterations are required [3].

Isogeometric Analysis (IGA) is a relatively new numerical method that aims to bridge the gap between CAD and FEM. It was first proposed by Prof. Hughes et.al. in 2005 [4] and has since been developed by many researchers. IGA uses the same basis functions as CAD, namely Non-Uniform Rational B-Splines (NURBS), to represent the geometry and the solution fields. This allows the direct use of CAD geometry in the analysis without the need for conversion or preprocessing. The use of the same functions also ensures the perfect geometric accuracy in the analysis mesh regardless of mesh size. In addition, IGA offers several advantages over traditional FEM such as higher order continuity (smoothness) in the solution between element boundaries, fewer degrees of freedom for the same mesh size, and the ability to incorporate design changes from CAD. These advantages lead to more accurate results with reduced computational cost [5]–[7].

An example of IGA and FEM meshes are shown in Fig. 1.2. A visible difference is that IGA mesh uses *control points* which may not exist on the surface of the geometry. The discretized solutions in IGA is computed on the control points in contrast to node

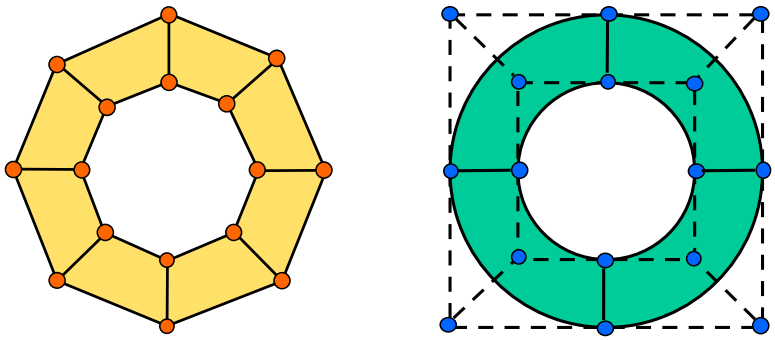

Figure 1.2: A simple example of IGA and FEM meshes

points in classical FEM.

1.2 Distributed Sensing and Structural Monitoring

At design stage, an engineering structure needs consideration of many factors such as mechanical strength, shape, material, cost and operating conditions. These can be called as known factors. The risk of failure after construction could be overloading, corrosion, environment and unpredicted events of impact or natural disasters. Countermeasures for these risks are based on the "best effort spirit", experience and a reasonable safety factor. Moreover, maintenance costs are often higher than initial construction costs, and the costs of maintenance are related to the how correctly the structure is deformed and aged [8].

Structural Health Monitoring (SHM) is an increasingly important concept in today's industry for maintenance and lifecycle management of engineering structures such as bridges, buildings, wind turbines, ships, airplanes, etc. Combining state-of-the-art sensors and analysis methods, digital twin and digital transformation are paid great attention not only for safety and maintenance but also for future design improvements. Digital Twin (DT) is a virtual representation of a physical system, which can be used to predict its current and future behavior without doing costly experiments or destructive testing. SHM paired with DT and a global network enables *remote sensing* which facilitates early detection of anomalies or deviation from the designed operation and prevents catastrophic failures by enabling interventions such as repairs or changing operating conditions [9]–[12].

In this context, IGA has a high potential to be a perfect SHM tool for its tight integration with CAD and FEM. That means a single model can be used for design, analysis and monitoring purposes, benefiting both design cycle and operation phase. However,

conventional IGA needs further development for SHM since it has to incorporate the real-world sensing data into the digital model. This is where the distributed fiber optic sensing (DFOS) technology fits the requirement.

DFOS is a sensing technology that uses an optical fiber and laser light to measure strain and temperature distribution along the fiber length [13]–[15]. There are several types of optical strain sensing technologies, namely fiber Bragg grating (FBG), or backscattering based sensors such as Brillouin, Rayleigh and Raman [14], [16]–[18]. FBG sensors have been widely used in the past studies, but backscattering based sensors have recently received attention for their improved spatial resolution. In addition, a backscattering based instrument can utilize an ordinary telecommunication type glass fiber without the need for any modification.

The sensing principle of backscattering-based DFOS is as follows. The interrogation instrument transmits a coherent laser pulse into the fiber which is backscattered by the Rayleigh scattering effect. A strain or temperature event on the fiber causes a shift in the backscattered light spectrum. The location of the event is determined from the time difference between the transmitted and backscattered light, and the speed of light in glass. All measurements are collected simultaneously along the fiber up to tens of kilometers in length which makes DFOS a distributed sensor.

Recent DFOS instruments can measure strain in centimeter spatial resolution with precision below $0.1\,\mathrm{microstrain}$ depending on the sensing cable, fiber interrogation and sample averaging counts [19]–[23]. Fiber optic (FO) cables are small, lightweight and resistant to electromagnetic radiation. Moreover, a fiber optical sensor does not need a power supply and has the ability for self-diagnostics in the case of breakage, which are the key factors of the cost in current systems. For these reasons, DFOS systems have been used in studies for monitoring concrete structures, power plants, aircraft wings and more [24]–[28].

1.2.1 Integration of IGA and DFOS

The physical sensing system is crucial in general but needs many other components apart from installing a FO sensor. Due to access conditions and FO bending properties, etc., the FO route cannot be freely designed and a CAD plan is necessary for installation. In addition, there is a gap in information between directly measured strains and necessary engineering data. The measurement data are usually sparse and limited in type of information, demanding the use of numerical analysis and finite element tools in order to translate data into insights [29]–[31]. For example, DFOS can be used to obtain distributed strain measurements along the optical fiber, and numerical tools are used to

estimate deformation, loading conditions and stress distributions in the structure [32]–[35].

The existing methodologies for structural monitoring mainly employ traditional FEM as a numerical tool [9]. But the application of IGA for SHM is very limited and there is no existing method which utilize both DFOS and IGA. Hence, there is prospect for efficiency improvement because CAD related data are standard for communication among different clusters of design and maintenance engineers. The utilization of CAD data resource is an elegant route which results in the focus on the IGA method. Combining the real-time distributed sensing capabilities of DFOS and high efficiency of IGA, a remote structural monitoring system can be developed as shown schematically in Fig. 1.3.

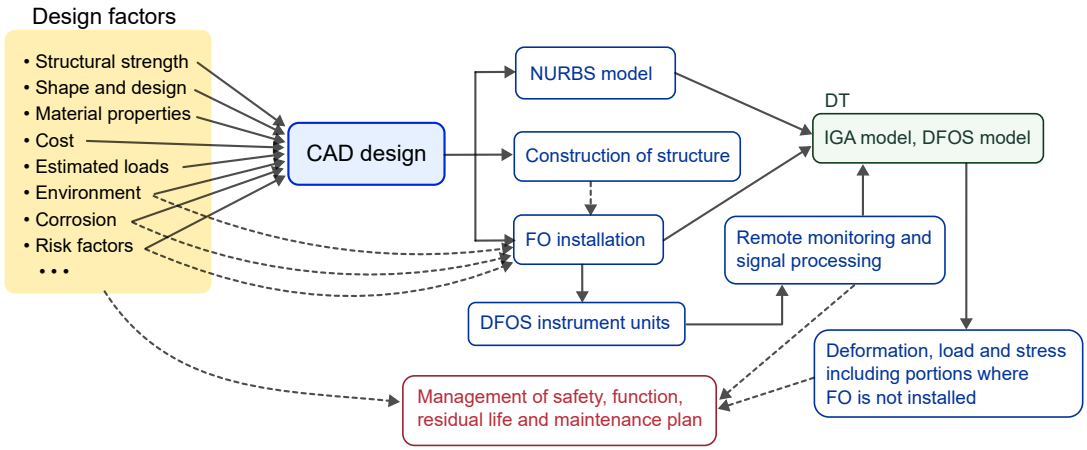

Figure 1.3: Block diagram of remote structural monitoring by DFOS and IGA. The solid lines indicate direct actions, and the dashed lines illustrate the links of solutions to the factors of concern.

Based on this status quo and literature gap, the first part of this thesis is dedicated to the development of a new DFOS-based IGA methodology for SHM. The developed method is based on the concept of *inverse IGA*, which is inspired from inverse FEM (iFEM) [32]. The inverse IGA reconstructs the deformation, strain and stress distribution in the structure from measured DFOS fiber strains. There are two main components of this method: the first one is the development of a fiber mesh model which represents the properties of optical fiber used for sensing, and the second is the inverse IGA algorithm which efficiently solves the aforementioned inverse problem.

The primary objective of the fiber mesh model is to simulate the DFOS measurements numerically. Firstly, the fiber route is defined in the geometry model from which the fiber mesh is generated. The fiber mesh consists of discrete sampling points along the fiber route and associated coordinate mappings to the surface of the host structure. It is

then is used to compute the fiber strains using IGA shape functions and the principles of DFOS sensing.

Based on the simulated fiber strains from fiber mesh model, a formulation of inverse IGA can be devised from the relationship between fiber strains and displacement field. The inverse problem is generally ill-posed, meaning that the number of unknowns is much larger than the number of observables, which makes calculation of exact solutions impossible. Hence, minimum energy principle is used as a regularization scheme to solve a constrained optimization problem in least-squares sense. This results in a general formulation which does not depend on the type of structure or fiber layout.

1.3 Nonlinear Material Models

IGA has been applied in nonlinear elastoplastic deformation and crash simulations of automobiles and ships, for example in commercial software LS-DYNA [36]. In elastoplastic simulations, not only the numerical method but also the material model is important for accuracy. Accurate material model is especially important for crash simulations, where the material is subjected to large deformation and high strain rate. Automobile structural parts are often made by press forming sheet metals. This process introduces large directional strains in the sheet metal. Hence, the properties of metal after forming may be different from those of the original metal due to strain history effects [37], [38]. The history dependent material properties are especially important for high strength steels used in automobile structural parts since they are subjected to large deformation and high strain rate during crash simulations.

In the second part of this thesis, a new material model is proposed which can capture the effect of unidirectional tensile prestrain in the sheet metal. Specifically, this model is intended to reproduce the differences in stress-strain response in orthotropic directions (anisotropic hardening) after the metal is subjected to prestrain. The anisotropic hardening effect is firstly investigated by tensile tests of prestrained specimens in different prestrain and reloading directions. The observed anisotropic hardening effect is then modelled using a modified Swift equation and anisotropic yield function.

The developed material model is implemented in the elastoplastic part of the in-house IGA code and validated with a comparison of numerical simulation and experimental results.

1.4 Structure of the Thesis

The remainder of the thesis is structured as follows.

Chapter 2 gives a theoretical background on isogeometric analysis method and necessary formulae for the later parts of the thesis. Specifically, it covers the main aspects of geometry representation, basis functions, IGA mesh generation, multi-patch coupling, Jacobians and numerical integration. This chapter also serves as the theoretical introduction for the in-house IGA code 'JWRIAN-IGA'.

Chapter 3 presents the development of a fiber mesh model which is a first step to integrate IGA and DFOS. The proposed fiber model is used with linear elastic IGA to simulate DFOS measurements. The properties of the model and their effects on the measurability are studied and numerically computed fiber strains are compared with experiment data. Finally, a case study on estimating unknown loadings on a structure is illustrated.

Chapter 4 proposes an analytical method of inverse IGA in which the displacement field is reconstructed from measured fiber strains. A detailed literature review on the existing inverse finite elements is given and the differences with the proposed method are explained. The developed method is validated with simulated examples, and sensitivity to practical DFOS parameters is studied. Then, the inverse IGA-DFOS is applied to estimate the deformation of a rotating impeller plate from the experimentally measured fiber strains.

Chapter 5 presents the experimental findings of anisotropic hardening behavior of prestrained high strength steel and formulation of a mathematical model the observed phenomena. The model is implemented in elastoplastic IGA code and validated with experimental data.

Chapter 6 summarizes the main outcomes of the research and gives an outlook on the future research directions.

Chapter 2

Theory and Development of Isogeometric Analysis

In this chapter, the detailed formulation of IGA will be described. We will begin with the parametric representation of geometry and fields, followed by the basis functions and their properties. Then, the concept of isogeometric analysis will be introduced in the context of solid mechanics by Galerkin method. We will also discuss important aspects of IGA such as coordinate systems, multi-patch coupling and material nonlinearity.

2.1 Geometry representation

The types of geometries used in IGA are based on splines which are commonly used for efficient representation of complex free-form shapes in CAD. The most common spline types are B-Splines and Non-Uniform Rational B-Splines (NURBS). There are other types of experimental splines in literature for unstructured meshes such as T-Splines [39], [40], S-Splines [41], LR-Bsplines [42], and truncated hierarchical B-splines (THB-splines) [43]–[45]. However, NURBS remains the simplest and most stable basis with well-studied properties [46] and hence it will be used for IGA in this research.

NURBS geometries are parametric, which means that the geometry is a function of parameters. Consider a curve $\boldsymbol{c}(\xi)$, where ξ is the parameter as illustrated in Fig. 2.1. The curve is defined by the product of univariate basis functions N_i and control point coordinates $\boldsymbol{C}_i$ of the following.

$$\boldsymbol{c}(\xi) = \sum_{i=1}^{n} N_i(\xi)\boldsymbol{C}_i,\ \xi \in \mathbb{R};\ \boldsymbol{c}, \boldsymbol{C}_i \in \mathbb{R}^3, \tag{2.1}$$

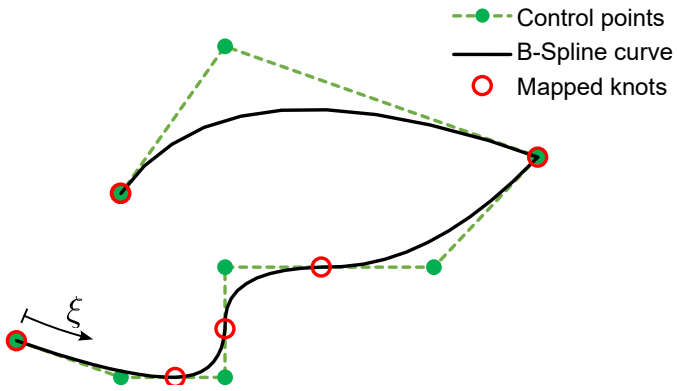

Figure 2.1: An example of a parametric spline curve

where n is the number of basis functions/control points and $\boldsymbol{c}$ is the curve point at parameter ξ. Likewise, the parametric surface and volume can be expressed as:

$$\boldsymbol{s}(\xi,\eta) = \sum_{i=1}^{n}\sum_{j=1}^{m} N_{ij}\boldsymbol{C}_{ij}, \tag{2.2}$$

$$\boldsymbol{v}(\xi,\eta,\zeta) = \sum_{i=1}^{n}\sum_{j=1}^{m}\sum_{k=1}^{l} N_{ijk}\boldsymbol{C}_{ijk}. \tag{2.3}$$

IGA is an isoparametric formulation which means the same basis can be used to represent fields such as displacement or strain. In such case, the control point coordinates $\boldsymbol{C}$ are replaced by the respective control point values. For instance, the displacement field is expressed using control point displacements $\boldsymbol{d}$ as follows:

$$\boldsymbol{u}(\xi) = \sum_{i=1}^{n} N_i(\xi)\boldsymbol{d}_i, \tag{2.4}$$

Before giving the explicit form of B-Spline and NURBS basis functions, the different types of coordinate systems in IGA must be introduced to provide relationship between the parameters and knot vectors.

2.2 Coordinate systems

The geometry and solution fields are interpolated by the same parameters as previously mentioned. Regardless of the physical dimensions of the geometry, the parametric dimensions are normalized between 0 and 1 by convention (although it is common to see unnormalized parmeters in CAD). The parametric space dictates the topology of the

geometry, i.e., whether it is a curve, surface or volume. A curve is defined by a single parameter, hence *univariate*, whereas a surface is *bivariate* and a volume is *trivariate*. The *parent element* refers to the parametric domain of a NURBS geometry, which is a unit square for a bivariate geometry and a unit cube for a trivariate geometry.

In FE computations, there is a need for numerical integration throughout the structure domain (surface or volume). Gaussian quadrature is commonly used for this purpose; however the Gauss points are defined within the interval $[-1, 1]$ and the basis functions are defined in the parametric space. Therefore, there are primarily three types of coordinate systems (or spaces) in IGA:

1. *parametric space*, where the basis functions are evaluated,
2. *Gauss space*, where the Gauss integration points are defined, and
3. *physical space*, in which the actual geometry and control points exist.

These are illustrated in a univariate example in Fig. 2.2. The dimensionality of physical

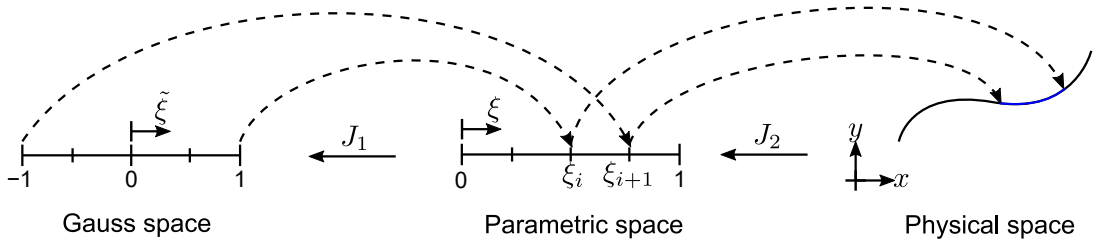

Figure 2.2: Coordinate systems and mappings

space is defined by the control points and is independent of the parametric dimensions. In this thesis, parametric coordinates will be designated by $\{\xi, \eta, \zeta\}$ or $\boldsymbol{\xi}$. The cardinality of the physical space is written as 1D, 2D or 3D, and represented by $\{X, Y, Z\}$ or $\{x, y, z\}$ axes.

The integration domain can be converted from one space to another using partial derivatives or Jacobians. The Jacobian from physical to parametric space can be derived as follows.

$$\boldsymbol{J}_1 = \frac{\partial \boldsymbol{x}}{\partial \xi} = \begin{bmatrix} \frac{\partial x}{\partial \xi} & \frac{\partial y}{\partial \xi} & \frac{\partial z}{\partial \xi} \end{bmatrix}^T, \tag{2.5}$$

$$|\boldsymbol{J_1}| = \sqrt{\left(\frac{\partial x}{\partial \xi}\right)^2 + \left(\frac{\partial y}{\partial \xi}\right)^2 + \left(\frac{\partial z}{\partial \xi}\right)^2}, \tag{2.6}$$

For bivariate surfaces and trivariate volumes, the Jacobian matrices are:

$$\boldsymbol{J}_1 = \begin{bmatrix} \frac{\partial x}{\partial \xi} & \frac{\partial x}{\partial \eta} & 1 \\ \frac{\partial y}{\partial \xi} & \frac{\partial y}{\partial \eta} & 1 \\ \frac{\partial z}{\partial \xi} & \frac{\partial z}{\partial \eta} & 1 \end{bmatrix} \text{ for bivariate surfaces,} \tag{2.7}$$

$$\boldsymbol{J}_1 = \begin{bmatrix} \frac{\partial x}{\partial \xi} & \frac{\partial x}{\partial \eta} & \frac{\partial x}{\partial \zeta} \\ \frac{\partial y}{\partial \xi} & \frac{\partial y}{\partial \eta} & \frac{\partial y}{\partial \zeta} \\ \frac{\partial z}{\partial \xi} & \frac{\partial z}{\partial \eta} & \frac{\partial z}{\partial \zeta} \end{bmatrix} \text{ for trivariate volumes,} \tag{2.8}$$

where the partial derivatives are calculated from the basis functions and control points as

$$\frac{\partial x}{\partial \xi} = \sum_{i=1}^{n} \frac{\partial N_i}{\partial \xi} \boldsymbol{C}_{x,i}, \ \frac{\partial y}{\partial \xi} = \sum_{i=1}^{n} \frac{\partial N_i}{\partial \xi} \boldsymbol{C}_{y,i}, \ \frac{\partial x}{\partial \eta} = \sum_{i=1}^{n} \frac{\partial N_i}{\partial \eta} \boldsymbol{C}_{x,i}, \ \cdots . \tag{2.9}$$

The transformation from Gauss space to parametric space follows a linear mapping:

$$\xi = \frac{1}{2}[(\xi_{i+1} - \xi_i)\tilde{\xi} + (\xi_{i+1} + \xi_i)], \tag{2.10}$$

where ξ_i, ξ_{i+1} is known as a *knot span*. Hence, the Jacobian $\boldsymbol{J}_2$ from parametric space to Gauss space is

$$\boldsymbol{J}_2 = \frac{\partial \xi}{\partial \tilde{\xi}} \text{ for univariate,} \tag{2.11}$$

$$\boldsymbol{J}_2 = \frac{\partial \xi}{\partial \tilde{\xi}} \frac{\partial \eta}{\partial \tilde{\eta}} \text{ for bivariate,} \tag{2.12}$$

$$\boldsymbol{J}_2 = \frac{\partial \xi}{\partial \tilde{\xi}} \frac{\partial \eta}{\partial \tilde{\eta}} \frac{\partial \zeta}{\partial \tilde{\zeta}} \text{ for trivariate.} \tag{2.13}$$

2.3 Basis functions and their derivatives

B-Spline basis functions of order p are defined recursively from Cox-de Boor equations as follows [46].

$$N_i^0(\xi) = \begin{cases} 1, & \text{if } \xi_i \leq \xi < \xi_{i+1}, \\ 0, & \text{otherwise} \end{cases} \text{ and}$$

$$N_i^p(\xi) = \frac{\xi - \xi_i}{\xi_{i+p} - \xi_i} N_i^{p-1}(\xi) + \frac{\xi_{i+p+1} - \xi}{\xi_{i+p+1} - \xi_{i+1}} N_{i+1}^{p-1}(\xi), \tag{2.14}$$

where ξ is the parameter value and ξ_i denotes i^{th} knot value in the knot vector $\Xi = \{\xi_1, \xi_2, \cdots, \xi_{n+p+1}\}$. A knot vector is a non-decreasing set of real numbers in the parameter space and normalized to $[0, 1]$ (more explanation in Section 2.4.1).

The first derivatives of B-Splines basis functions are given by:

$$\frac{\mathrm{d}}{\mathrm{d}\xi}N_i^p(\xi) = \frac{p}{\xi_{i+p} - \xi_i}N_i^{p-1}(\xi) - \frac{p}{\xi_{i+p+1} - \xi_{i+1}}N_{i+1}^{p-1}(\xi). \tag{2.15}$$

Non-Uniform Rational B-Splines (NURBS) basis functions are generalized case of B-Spline basis functions to permit exact representation of conic sections which are widely used in lines plans of ships. NURBS basis functions are calculated by projected transformation of B-Splines by adding an additional weight parameter to each control point and taking the weighted average of B-Spline functions as shown in Eq. (2.16).

$$R_i^p(\xi) = \frac{N_{i,p}(\xi)w_i}{\sum_{i=1}^n N_{i,p}(\xi)w_i} \tag{2.16}$$

where w_i is the weight vector with dimension equal to number of control points.

Bivariate and trivariate NURBS basis functions are defined by projection of tensor products of B-Splines basis functions, as shown in Eq. (2.17) and (2.18).

$$R_{i,j}^{p,q}(\xi,\eta) = \frac{N_{i,p}(\xi)M_{j,q}(\eta)w_{i,j}}{\sum_{i=1}^n\sum_{j=1}^m N_{i,p}(\xi)M_{j,q}(\eta)w_{i,j}} \tag{2.17}$$

$$R_{i,j,k}^{p,q,r}(\xi,\eta,\zeta) = \frac{N_{i,p}(\xi)M_{j,q}(\eta)L_{k,r}(\zeta)w_{i,j,k}}{\sum_{i=1}^n\sum_{j=1}^m\sum_{k=1}^l N_{i,p}(\xi)M_{j,q}(\eta)L_{k,r}(\xi)w_{i,j,k}} \tag{2.18}$$

If all the weight values in w vector are equal, NURBS basis degenerates into B-Spline basis.[1]

The first NURBS derivatives can also be derived from the B-Spline derivatives as follows [3]:

$$\frac{\mathrm{d}}{\mathrm{d}\xi}R_i^p(\xi) = w_i\frac{W(\xi)N'_{i,p}(\xi) - W'(\xi)N_{i,p}(\xi)}{(W(\xi))^2}, \tag{2.19}$$

where $N'_{i,p}(\xi) = \frac{\mathrm{d}}{\mathrm{d}\xi}N_{i,p}(\xi)$ and

$$W'(\xi) = \sum_{j=1}^n N'_{j,p}(\xi)w_j. \tag{2.20}$$

The derivatives with respect to physical coordinates can be calculated by the chain rule as:

$$\frac{\partial}{\partial x}N_{i,p}(\xi) = \frac{\mathrm{d}N_{i,p}(\xi)}{\mathrm{d}\xi}\frac{\partial\xi}{\partial x} = \frac{\mathrm{d}N_{i,p}(\xi)}{\mathrm{d}\xi}|\boldsymbol{J}_1^{-1}|. \tag{2.21}$$

[1] A note on the notation: N_i may also be used to denote a general basis function without a strict reference to B-Spline or NURBS, univariate or multivariate. Its definition should be clear from the context.

2.4 IGA mesh and refinement

2.4.1 Knot vectors

Although control points are analogous to nodes in traditional FEM, knot vectors define the element or mesh boundaries instead of control net in IGA. A knot vector is a non-decreasing set of real numbers in the parametric space. For example, in ξ parametric direction, the knot vector is defined as $\Xi = \{\xi_1, \xi_2, \cdots, \xi_{n+p+1}\}, \xi_i \in \mathbb{R}$. In standard IGA formulations, knot vectors are normalized between 0 to 1. Knot vectors in CAD are usually not normalized but they can be simply normalized by dividing all knots by the largest knot value and adding the offset. A *knot span* is defined as the difference between two consecutive knots. The mapping from knot spans (parametric dimension) to mesh span (physical dimension) only depends on the relative size of knot spans and hence normalizing knots does not change the physical geometry. For surface and volumes, the lines of constant knots define the physical mesh lines. Therefore, an IGA mesh consists of knot spans and associated control points as illustrated in Fig. 2.3.

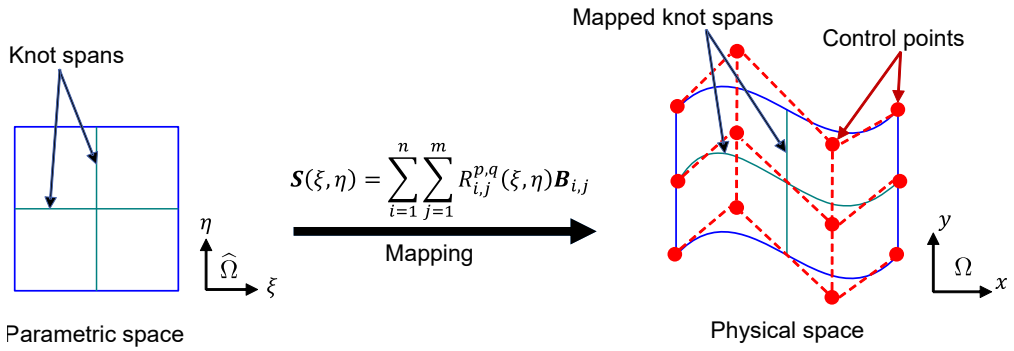

Figure 2.3: Parametrization for a bivariate surface. The knot spans comprise the subdivisions of the parametric domain and mapped knot spans mark the subdivisions in physical space which make up the IGA mesh.

Knot multiplicity is defined by the number of times a knot is repeated. If a knot is repeated m times, the number of continuous derivatives of the basis functions become $(p - m - 1)$. Hence, the continuity of geometry (or fields) can be controlled by the number of repeated knots. In Fig. 2.1, each 'segment' can be identified by the mapped knots. Note the C^0 continuous kink at the 5^{th} knot. The knot vectors in IGA are *open* which means the first and last knots are repeated $p + 1$ times. This has the effect of making boundary knot lines (or surfaces) isolated to the terminal control points. The

following equation shows an open knot vector.

$$\Xi = \left\{ \underbrace{\xi_0, \cdots, \xi_p,}_{p+1 \text{ equal terms}} \, , \xi_{p+1}, \cdots, \underbrace{\xi_{n+1}, \cdots, \xi_{n+p+1}}_{p+1 \text{ equal terms}} \right\} \tag{2.22}$$

The open knot vector facilitates easy extraction of boundary surfaces from a volume by simply copying the desired knot vectors and associated control points.

2.4.2 Mesh refinement

In traditional FEM, each element has its own parametric space or parent element. The IGA parameter space however, maps to the entire patch. A *patch* is the unique mapping from the parent element to the physical space.

The NURBS data (i.e. control points and knot vectors) in each patch can be used as an analysis mesh in IGA. However, refinement of the original mesh is usually required for higher solution accuracy. In principle, there are three types of mesh refinement in IGA:

- *h-refinement*, which subdivides the physical mesh by adding knots and control points,
- *p-refinement*, which increases the order of the basis functions, and
- *k-refinement*, which combines h-refinement and p-refinement.

In all cases, the original geometry is unchanged by the refinement process. In this research, h-refinement is primarily used for mesh refinement since it is the most reliable method to increase accuracy [47].

The h-refinement is a method of subdividing a NURBS patch by adding knots (and hence more control points) while keeping the original geometry unchanged. This can be done by *knot insertion* algorithm [3], [46]. In this process, new knots ξ' are added to the existing knot vector Ξ to create more knot spans. Inserting unique knots preserves the continuity of the original geometry whereas knot multiplicity reduces the continuity.

Let the existing knot vector $\Xi = \{\xi_1, \xi_2, \cdots, \xi_{n+p+1}\}$. If the added knots are $\bar{\xi}_1, \bar{\xi}_2, \cdots, \bar{\xi}_m$, there will be $n + m$ basis functions after refinement. The new control points $\overline{\boldsymbol{C}} = \{\overline{\boldsymbol{C}}_1, \overline{\boldsymbol{C}}_2, \cdots, \overline{\boldsymbol{C}}_{n+m}\}^T$ can be found by:

$$\overline{\boldsymbol{C}} = \boldsymbol{T}^T \boldsymbol{C} \tag{2.23}$$

$$T_{ij}^{0} = \begin{cases} 1 & \text{if } \bar{\xi}_i \in [\xi_j, \xi_{j+1}) \\ 0 & \text{otherwise} \end{cases} \text{ and} \tag{2.24}$$

$$T_{ij}^{q+1} = \frac{\bar{\xi}_{i+q} - \xi_j}{\xi_{j+q} - \xi_j} T_{ij}^{q} + \frac{\xi_{j+q+1} - \bar{\xi}_{i+q}}{\xi_{j+q+1} - \xi_{j+1}} T_{ij+1}^{q}, \; q = 0, 1, 2, \cdots, p-1 \tag{2.25}$$

A 2D example of h-refinement by knot insertion is illustrated in Fig. 2.4 where two knots are inserted to Ξ and one knot is inserted to $\mathcal{H}$. Knot lines in physical space are added accordingly and new control points are computed from Eqn. (2.23).

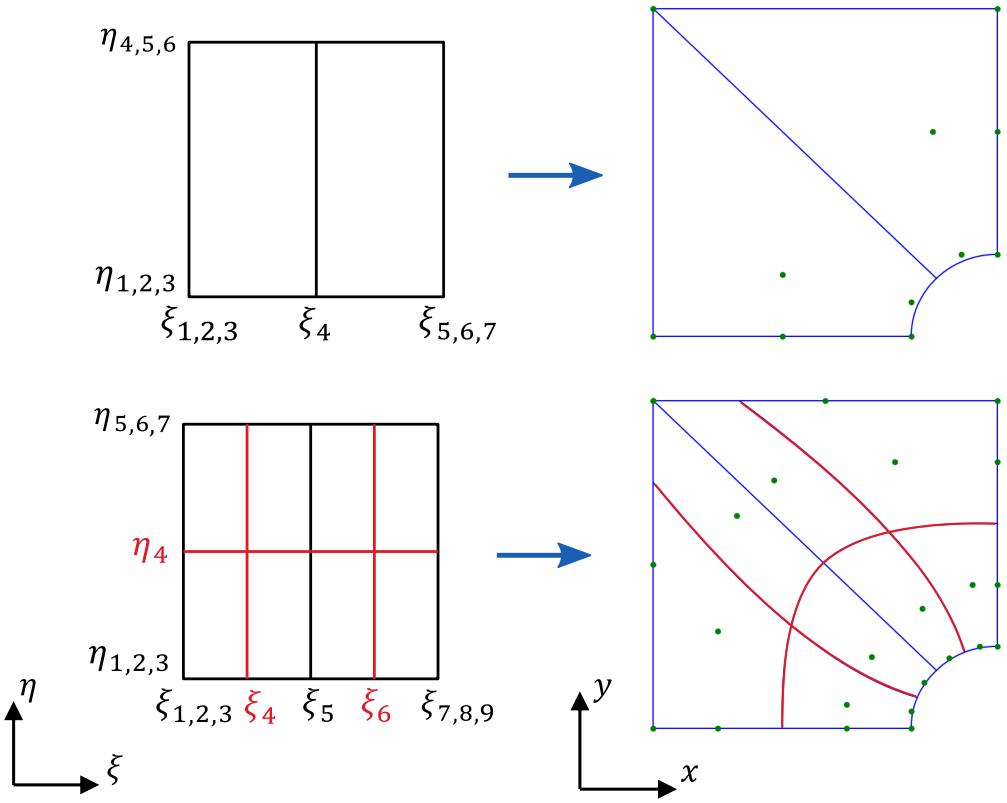

Figure 2.4: Illustration of h-refinement. The knot spans are subdivided and corresponding control points are generated by the h-refinement algorithm.

2.4.3 Applying boundary conditions

Detached control points from the physical mesh makes the application of Dirichlet boundary conditions (BC) non-trivial. If the boundary is on C^0 continuous edges or surfaces, homogeneous BCs (zero displacements) can be directly applied to control points. In general however, BCs cannot be applied directly to control points since NURBS basis functions do not satisfy Kronecker delta property. It is illustrated in Fig. 2.5 where applying a certain displacement to a control point does not move the geometry by the same

amount. In this case, the enforcement of prescribed boundary can be done by deriving control point values by one of the two methods: interpolating points or least-square fit [48]:

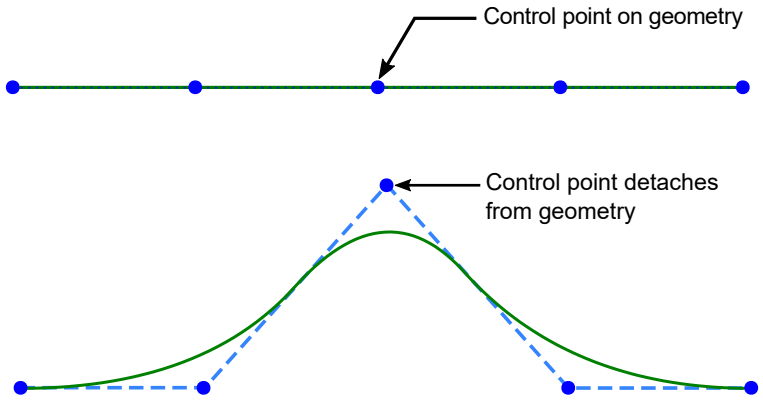

Figure 2.5: Different displacements of control points and geometry

Interpolating points

In this method, sampling points $\boldsymbol{U}$ are chosen on the desired boundary curve or surface. The number of sampling points is equal to the number of control points which has influence on the boundary. Then basis functions are evaluated on the corresponding parametric coordinates of the sampling points to get the basis functions matrix $\boldsymbol{M}$, where M_{ij} is the basis function value of j^{th} control point for the i^{th} sampling point. Finally, the control point values are calculated by the inverse relation.

$$\boldsymbol{U} = \boldsymbol{M}\boldsymbol{C} \tag{2.26}$$

$$\boldsymbol{C} = \boldsymbol{M}^{-1}\boldsymbol{U} \tag{2.27}$$

The sampling points should be fairly distributed on the boundary to prevent singularity of $\boldsymbol{M}$ and to keep numerical stability.

Lease square fit

In contrast to finding the exact inverse in interpolating points, this method uses a least square fit of the boundary over the sampling points. This is advantageous when the sampling points have noise or the NURBS boundary cannot admit all the points. The number of sampling points is more flexible in this method since it does not need to be equal to the number of active control points [49]. The fitting can be done by solving the

least-squares matrix:

$$\boldsymbol{C} = \left[\boldsymbol{M}^T\boldsymbol{M}\right]^{-1}\left[\boldsymbol{M}^T\boldsymbol{U}\right]. \tag{2.28}$$

2.5 Linear elastic IGA

The weak form of the governing equations in a structural system can be derived from the minimum potential energy principle or the virtual work principle. The total strain potential energy of a structural system is given by:

$$\Pi = \frac{1}{2}\int_\Omega \boldsymbol{\sigma}^T\boldsymbol{\varepsilon}\,\mathrm{d}\Omega - \int_\Omega \boldsymbol{b}^T\boldsymbol{u}\,\mathrm{d}\Omega - \int_\Gamma \boldsymbol{h}^T\boldsymbol{u}\,\mathrm{d}\Gamma, \tag{2.29}$$

where $\boldsymbol{u}, \boldsymbol{\varepsilon}, \boldsymbol{\sigma}, \boldsymbol{b}, \boldsymbol{h}$ are displacement, strain, stress, body force and traction force on the boundary Γ, respectively. The first term in Eq. (2.29) is the strain energy, the second term is the work done by the body force and the third term is the work done by the surface traction. After discretization of the domain Ω, displacement distribution can be expressed in terms of interpolation functions $\boldsymbol{N}$ and discretized displacements $\boldsymbol{d}$:

$$\boldsymbol{u}(\boldsymbol{\xi}) = \sum_{i=0}^{n} N_i(\boldsymbol{\xi})\boldsymbol{d}_i, \tag{2.30}$$

where $\boldsymbol{\xi} = (\xi, \eta, \zeta)$ are the parametric coordinates, and $\boldsymbol{d}_i = [d_{ix}, d_{iy}, d_{iz}]^T$ is the displacement vector of i^{th} control point. The symbol N_i is used here instead of $R^{p,q,r}_{i,j,k}$ for brevity and to be consistent with conventional notation. Strain and stress distributions can be obtained using the strain-displacement matrix $\boldsymbol{B}$ and constitutive relation:

$$\boldsymbol{\varepsilon}(\boldsymbol{\xi}) = \boldsymbol{B}(\boldsymbol{\xi})\boldsymbol{d}, \tag{2.31}$$

$$\boldsymbol{\sigma}(\boldsymbol{\xi}) = \boldsymbol{D}\boldsymbol{\varepsilon}(\boldsymbol{\xi}), \tag{2.32}$$

$$\boldsymbol{B} = \begin{bmatrix} N_{1,x} & 0 & 0 & \cdots & N_{n,x} & 0 & 0 \\ 0 & N_{1,y} & 0 & \cdots & 0 & N_{n,y} & 0 \\ 0 & 0 & N_{1,z} & \cdots & 0 & 0 & N_{n,z} \\ N_{1,y} & N_{1,x} & 0 & \cdots & N_{n,y} & N_{n,x} & 0 \\ 0 & N_{1,z} & N_{1,y} & \cdots & 0 & N_{n,z} & N_{n,y} \\ N_{1,z} & 0 & N_{1,x} & \cdots & N_{n,z} & 0 & N_{n,x} \end{bmatrix}, \tag{2.33}$$

where $N_{i,\mathcal{X}}$ means $\frac{\partial N_i}{\partial \mathcal{X}}$ and $\boldsymbol{D}$ is the elasticity matrix. Here, $\boldsymbol{\varepsilon}$ and $\boldsymbol{\sigma}$ are expressed in vectorized form using Voigt notation:

$$\boldsymbol{\varepsilon} = \begin{bmatrix} \varepsilon_{xx} & \varepsilon_{yy} & \varepsilon_{zz} & 2\varepsilon_{xy} & 2\varepsilon_{yz} & 2\varepsilon_{xz} \end{bmatrix}^T, \tag{2.34}$$

$$\boldsymbol{\sigma} = \begin{bmatrix} \sigma_{xx} & \sigma_{yy} & \sigma_{zz} & \sigma_{xy} & \sigma_{yz} & \sigma_{xz} \end{bmatrix}^T. \tag{2.35}$$

Then, the potential energy can be approximated from the discretized variables by piecewise integration on element e with its domain Ω_e and boundary Γ_e:

$$\Pi \approx \sum_{e=1}^{n_e} \left[\frac{1}{2} \int_{\Omega_e} \boldsymbol{B}^T \boldsymbol{d}^T \boldsymbol{D} \boldsymbol{B} \boldsymbol{d} \, \mathrm{d}\Omega_e - \int_{\Omega_e} \boldsymbol{N}^T \boldsymbol{d}^T \boldsymbol{b} \, \mathrm{d}\Omega_e - \int_{\Gamma_e} \boldsymbol{N}^T \boldsymbol{d}^T \boldsymbol{h} \, \mathrm{d}\Gamma_e \right]. \tag{2.36}$$

The stationary condition ($\delta\Pi = 0$) requires that the variation of potential energy is zero with respect to each free variable $\boldsymbol{d}$.

$$\frac{\partial \Pi}{\partial \boldsymbol{d}} = 0, \tag{2.37}$$

$$\sum_{e=1}^{n_e} \left[\left(\int_{\Omega_e} \boldsymbol{B}^T \boldsymbol{D} \boldsymbol{B} \, \mathrm{d}\Omega_e \right) \boldsymbol{d} - \int_{\Omega_e} \boldsymbol{N}^T \boldsymbol{b} \, \mathrm{d}\Omega_e - \int_{\Gamma_e} \boldsymbol{N}^T \boldsymbol{h} \, \mathrm{d}\Gamma_e \right] = 0. \tag{2.38}$$

Then element stiffness matrix $\boldsymbol{K}_e$ and external force vector $\boldsymbol{f}_e$ can be defined as:

$$\boldsymbol{K}_e = \int_{\Omega_e} \boldsymbol{B}^T \boldsymbol{D} \boldsymbol{B} \, \mathrm{d}\Omega_e, \tag{2.39}$$

$$\boldsymbol{f}_e = \int_{\Omega_e} \boldsymbol{N}^T \boldsymbol{b} \, \mathrm{d}\Omega_e + \int_{\Gamma_e} \boldsymbol{N}^T \boldsymbol{h} \, \mathrm{d}\Gamma_e \tag{2.40}$$

and global stiffness matrix and force vector as:

$$\boldsymbol{K} = \sum_{e=1}^{n_e} \boldsymbol{K}_e, \quad \boldsymbol{f} = \sum_{e=1}^{n_e} \boldsymbol{f}_e. \tag{2.41}$$

Then, Eq. (2.38) becomes:

$$\boldsymbol{K} \boldsymbol{d} = \boldsymbol{f}. \tag{2.42}$$

The integrals in Eq. (2.39) and Eq. (2.40) can be numerically evaluated using stan-

dard Gauss-Legendre quadrature:

$$\boldsymbol{K}_e \approx \sum_{i}^{\text{nipt}} \boldsymbol{B}^T \boldsymbol{D} \boldsymbol{B} |\boldsymbol{J}_1||\boldsymbol{J}_2| w_i, \tag{2.43}$$

$$\boldsymbol{f}_e \approx \sum_{i}^{\text{nipt}} \boldsymbol{N}^T \boldsymbol{b} |\boldsymbol{J}_1||\boldsymbol{J}_2| w_i + \sum_{j}^{\text{nipt}} \boldsymbol{N}^T \boldsymbol{h} |\boldsymbol{J}_1||\boldsymbol{J}_2| w_j, \tag{2.44}$$

where nipt is the number of integration points and w_i is the Gauss weight of i^{th} integration point.

2.6 Coupling of multi-patch geometries

While NURBS geometries can accurately represent free-from surfaces and volumes, their grid-like tensor product structure is not suitable for geometries with complex morphology. In such cases, the geometry is divided into multiple patches and the patches are coupled together for analysis. Each patch has its own parametric space and hence independent of other patches in terms of topology. Therefore, the patches must be coupled or 'glued' together in physical space for structural analysis in IGA. The coupling can be achieved by either *weak* or *strong* coupling. In weak coupling, the continuity is enforced by the continuity of the basis functions. In strong coupling, the continuity is enforced by merging the shared control points and knot spans. However, creating a compatible control point mesh between two patches is cumbersome or even impossible in practice. Hence, weak coupling is preferred in practice. It can be achieved by the Nitsche penalty method [50] which is used in this research. The penalty method is applied for the weak enforcement of Dirichlet boundary conditions without increasing the number of equations in the system. It is a variational method that adds a penalty term to the weak form in Eq. (2.29). The penalty term is weighted by a penalty parameter β as follows.

$$\Pi = \frac{1}{2}\int_\Omega \boldsymbol{\sigma}^T \boldsymbol{\varepsilon}\, \mathrm{d}\Omega - \int_\Omega \boldsymbol{b}^T \boldsymbol{u}\, \mathrm{d}\Omega - \int_\Gamma \boldsymbol{h}^T \boldsymbol{u}\, \mathrm{d}\Gamma + \underbrace{\frac{1}{2}\beta \int_{\Gamma_U} \boldsymbol{u}^T \boldsymbol{u}\, \mathrm{d}\Gamma_U}_{\text{penalty term}}. \tag{2.45}$$

The continuity term for displacement between two patches is simply:

$$\boldsymbol{u}^{(1)} - \boldsymbol{u}^{(2)} = 0 \text{ on } \Gamma_U, \tag{2.46}$$

Continuity for stress field can be enforced by the flux equilibrium condition on the shared surface.

$$(1-\gamma)\boldsymbol{\sigma}^{(1)}\boldsymbol{n}^{(1)} - \gamma\boldsymbol{\sigma}^{(2)}\boldsymbol{n}^{(2)} = \boldsymbol{0} \text{ on } \Gamma_U. \tag{2.47}$$

However, the stress continuity is not considered in this thesis due to additional complexity for the calculation of γ. The error in breaching stress continuity is expected to be negligible in the overall solution.

After discretization and numerical quadrature, the governing equation for multi-patch problems can be written as follows.

$$(\boldsymbol{K} + \boldsymbol{K_c})\,\boldsymbol{d} = \boldsymbol{f}, \tag{2.48}$$

where $\boldsymbol{K}_c$ is the coupling matrix with coefficients derived from the basis functions of the shared surface. From Eq. (2.45), the coupling matrix is assembled from the basis functions as follows.

$$\boldsymbol{K_c} = \sum_{\Gamma} \beta \boldsymbol{N}^T \boldsymbol{N}. \tag{2.49}$$

The penalty parameter β can be interpreted as the stiffness of the coupling as illustrated in Figure 2.6. It should be chosen carefully to avoid ill-conditioning of the system matrix. As a rule of thumb, it can be estimated to be on the same order of magnitude as the Young's modulus or mean diagonal of stiffness matrix $\boldsymbol{K}$.

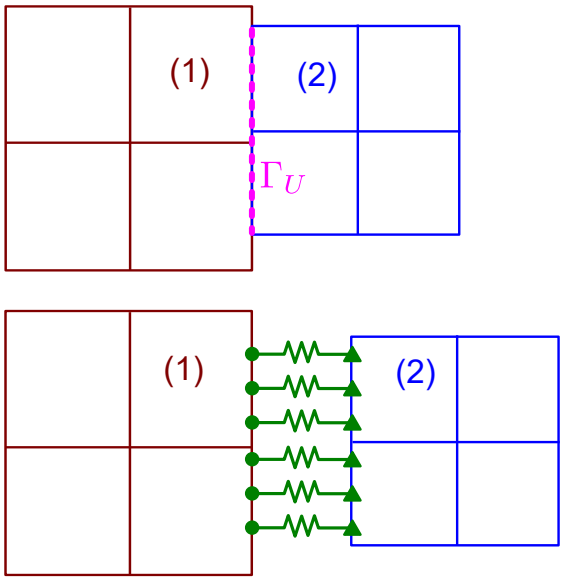

Figure 2.6: (above) Patch (1) and (2) with a shared interface Γ_U. (below) Collocation points on the two patches with the interpretation of penalty parameter as stiffness.

For the coupling of NURBS volume patches, the shared surface is extracted from one of the volumes. The patches are designated as master and slave, and the surface is extracted from the slave patch. A trivariate volume patch consists of six surfaces patches which can be individually extracted using respective knot vectors and control points.

The collocation points are taken from physical mapping of Gauss points on the extracted surface, and the integration is performed on that surface to obtain the coupling matrix $\boldsymbol{K}_c$.

For nonlinear problems, $\boldsymbol{K}_c$ is assumed to be constant and is calculated only once at the beginning of the analysis. It is added to the tangent stiffness matrix $\boldsymbol{K}_t$ in each iteration of the Newton-Raphson method.

2.7 Summary

The mathematical background for isogeometric analysis in the context of solid mechanics was presented in this chapter. The form of B-Spline and NURBS basis functions are given along with the representation of geometry and field variables using the basis functions. Different coordinate systems and Jacobians were introduced. IGA mesh generation for numerical analysis and mesh refinement was explained from the perspective of knot vectors. Finally, the coupling of multi-patch geometries was explained using the penalty method. These concepts lay the foundation for the following chapters in which new methodologies are developed based on NURBS, multi-patch IGA and variational principles.

Chapter 3

Integration of IGA and Distributed Fiber Optic Sensing

3.1 Introduction

This chapter presents the extension of IGA to utilize distributed fiber optic sensing (DFOS) through the development of a mathematical model to represent the optical fiber. This is the first step towards using DFOS in IGA in a unified framework. The properties of the fiber mesh are analytically studied and simulated fiber strains are compared with measurements in an experimental model. Then, the developed model is applied to estimate the deformation and loading condition from DFOS data.

3.2 Development of Fiber Mesh Model for IGA

The quantities of interest of a DFOS fiber in the context of numerical analysis include

- fiber geometry,
- fiber arclength (1D coordinates),
- fiber strain sampling interval, and
- averaging window length.

The fiber geometry is crucial because the fiber coordinates from DFOS measurements are strictly one-dimensional and measured along the arclength. However, the actual fiber exists in a three-dimensional space, is rarely a straight line, and attached to the host structure. The fiber strain sampling interval is the distance between two consecutive strain measurements. Calibration of fiber coordinates can be done on a few points but

translating all measurement points to spatial coordinates is not straightforward. The geometry of the fiber is also important to know the strain sensing direction (or tangential direction) at the sampling position. In addition to these quantities, the relation of fiber sampling points to the deformation of host structure must be considered in order to map the to surface strains 1D fiber strains.

Considering the above factors, the fiber mesh model was developed as an extension of univariate NURBS curve. Hence, the fiber geometry is a parametric curve in 3D space, and the fiber strain sampling interval is the arclength between two consecutive sampling points. Likewise, the fiber coordinate is the arclength of the fiber curve from origin to the sampling point. In accordance with the convention of IGA (as described in Section 2.2), the parametric coordinates are normalized to [0,1] with its associated knot vector $\Xi = \{\xi \mid \xi \in [0,1],\ \xi_{i+1} \geq \xi_i\}$. However, further formulations such as mapping from the fiber to the base structure in terms of global coordinates and calculation of fiber strains still remain. The following section details the mathematical formulation of the fiber based on this foundation.

3.2.1 Fiber curve

An example of a second order NURBS curve and tangent vectors are illustrated in Fig. 3.1. The physical coordinates $\boldsymbol{x}$ of the fiber at the parametric coordinate ξ can be calculated from the basis functions and control points:

$$\boldsymbol{x}(\xi) = \sum_{i=1}^{n} N_i(\xi)\, \boldsymbol{C}_i. \tag{3.1}$$

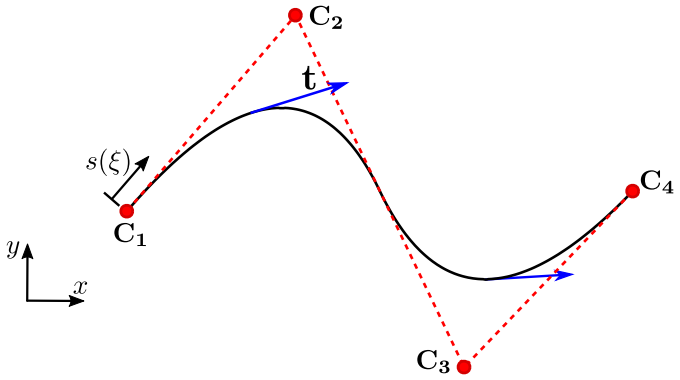

Figure 3.1: A second order NURBS curve showing control points $(\boldsymbol{C}_1, \boldsymbol{C}_2, \boldsymbol{C}_3, \boldsymbol{C}_4)$ and tangent vectors $\boldsymbol{t}$.

The fiber coordinate s is equal to the arclength of the curve from origin, which can

be found as:

$$s(\xi) = \int_0^s ds = \int_0^\xi \|\boldsymbol{J}_2\| d\xi, \tag{3.2}$$

where $\boldsymbol{J}_2$ is the Jacobian from parametric to physical space (see Section 2.2).

Since DFOS measurements are given in terms of fiber coordinates, it is also necessary to convert the physical fiber coordinates to parametric coordinates (i.e, $s \to \xi$). This can be performed using Newton-Raphson iteration or golden section search since s and ξ have a monotonic relationship as $\|\boldsymbol{J}_2\| > 0$ [1].

In the calculation of fiber strains described in the following section, tangent vector at the fiber sampling point is required. The tangent vector $\bar{\boldsymbol{t}}$ of the fiber at parameter ξ can be derived as:

$$\bar{\boldsymbol{t}}(\xi) = \frac{d\boldsymbol{x}(\xi)}{d\xi} = \sum_{i=1}^{n} \frac{dN_i(\xi)}{d\xi} \boldsymbol{C}_i, \tag{3.3}$$

and the unit tangent vector is given by:

$$\widetilde{\boldsymbol{t}}(\xi) = \frac{\bar{\boldsymbol{t}}(\xi)}{\|\bar{\boldsymbol{t}}(\xi)\|}. \tag{3.4}$$

3.2.2 Conversion from strain tensor to fiber strains

The fiber mesh model is based on the assumption that the fiber strains are linearly related to the displacement field in the solid structure. It is also assumed that mass and stiffness of the optical fiber have negligible contribution to the structural system.

Let the distribution of strain tensor $\boldsymbol{E}$ of the base structure have been obtained from a numerical simulation. In order to calculate one-dimensional fiber strains, the strain tensor on the structure's surface can be projected along the fiber tangent direction at the sampling point [51]. The fiber strain at the sampling point s, which corresponds to global coordinates $\boldsymbol{x}$, can be computed by:

$$\varepsilon_f(s) = \widetilde{\boldsymbol{t}}^T \boldsymbol{E}\, \widetilde{\boldsymbol{t}}, \tag{3.5}$$

$$\boldsymbol{E}[\boldsymbol{x}(s)] = \begin{bmatrix} \varepsilon_{xx} & \varepsilon_{xy} & \varepsilon_{xz} \\ \varepsilon_{xy} & \varepsilon_{yy} & \varepsilon_{yz} \\ \varepsilon_{xz} & \varepsilon_{yz} & \varepsilon_{zz} \end{bmatrix}, \quad \widetilde{\boldsymbol{t}}(s) = \begin{pmatrix} t_x \\ t_y \\ t_z \end{pmatrix}. \tag{3.6}$$

To allow the use of vectorized strain tensor in Voigt notation, Eq. (3.5) can be rewritten

[1] Since the basis function derivatives can be undefined at multiplicative knot positions, the implementation of Newton-Raphson iteration should mitigate this scenario.

in vector form exploiting the symmetry of the strain tensor:

$$\varepsilon_f = \boldsymbol{t}^T \varepsilon, \tag{3.7}$$

$$\varepsilon = \begin{bmatrix} \varepsilon_{xx} & \varepsilon_{yy} & \varepsilon_{zz} & 2\varepsilon_{xy} & 2\varepsilon_{yz} & 2\varepsilon_{xz} \end{bmatrix}^T, \tag{3.8}$$

$$\boldsymbol{t} = \begin{bmatrix} t_x^2 & t_y^2 & t_z^2 & t_x t_y & t_y t_z & t_x t_z \end{bmatrix}. \tag{3.9}$$

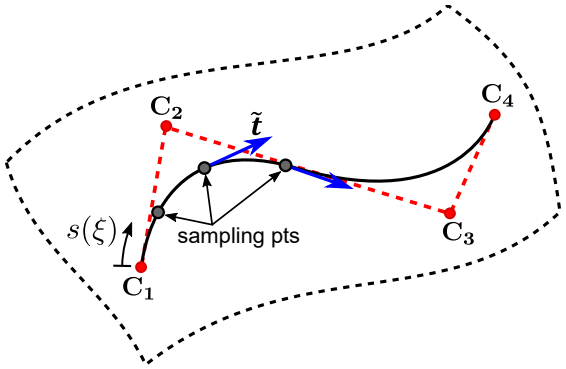

Figure 3.2: Illustration of fiber strain sampling points with sampling interval Δs; sampling resolution is numerically the same as the moving average window.

In practice, fiber strains are not measured as point strains but averaged over a distance Δs as illustrated in Fig. 3.2. Hence, the moving average fiber strain at the mid sampling location s can be expressed as the following.

$$\overline{\varepsilon}_f(s) = \frac{1}{\Delta s} \int_{s-\frac{\Delta s}{2}}^{s+\frac{\Delta s}{2}} \varepsilon_f(s)\, ds, \tag{3.10}$$

$$\overline{\varepsilon}_f(s) = \frac{1}{d} \sum_{i=1}^{\text{nipt}} \varepsilon_f(s_i) \left|\boldsymbol{J}_{1i}\right| \left|\boldsymbol{J}_{2i}\right| \gamma_i, \tag{3.11}$$

where γ is the weighting function to adjust the shape of the moving average window ($\gamma = 1$ for rectangular window).

A flow chart which summarizes the elastic stress analysis and fiber strain calculation at all sampling points, is shown in Fig. A.1.

3.2.3 Validation of the numerical code

In order to validate the numerical implementation of the fiber model in JWRIAN-IGA and investigate the relation of fiber strains to surface strains, a circular fiber on a simply

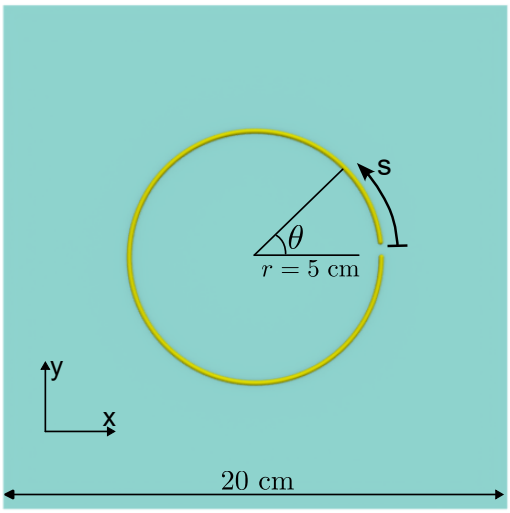

Figure 3.3: Simple validation model for fiber strain calculation

supported plate is devised as shown in Fig. 3.3.

The parametric equation for a unit circle is

$$s(\theta) = (\cos\theta, \sin\theta), \tag{3.12}$$

and the tangent vector is

$$t(\theta) = (-\sin\theta, \cos\theta). \tag{3.13}$$

Firstly, a uniform strain of $\varepsilon_{xx} = 100 \times 10^{-6} = 100\,\mu\varepsilon$ is applied to the plate with other strain components equal to zero[2]. This simplifies the analytical solution of fiber strains to $\varepsilon_f = \varepsilon_{xx}\sin^2\theta$. Figure 3.4 compares the fiber strains from the numerical model with the analytical solution. Note that the total fiber length is $\pi \times 0.1 \approx 0.3\,\mathrm{m}$. The plot also shows the moving average fiber strains with $5\,\mathrm{cm}$ and $10\,\mathrm{cm}$ window lengths. Five integration points were used for numerical quadrature in Eq. (3.11). The analytical and numerical results for continuous (on-point) fiber strains are identical within the numerical precision. There are a few small deviations in moving average fiber strains due to the numerical integration error. The zero fiber strains correspond to the points where the fiber is perpendicular to the strain direction $(\theta = 90°, 270°)$.

Next, the plate is subjected to a biaxial strain state with $\varepsilon_{xx} = 100\,\mu\varepsilon$ and $\varepsilon_{yy} = -30\,\mu\varepsilon$, the analytical solution being $\varepsilon_f = \varepsilon_{xx}\sin^2\theta + \varepsilon_{yy}\cos^2\theta$. From the fiber strain

[2]The unit $(\mu\varepsilon)$ refers to *micro-strain* $(\mu\mathrm{m/m})$ which is a common unit for fiber strain measurements although strain is dimensionless.

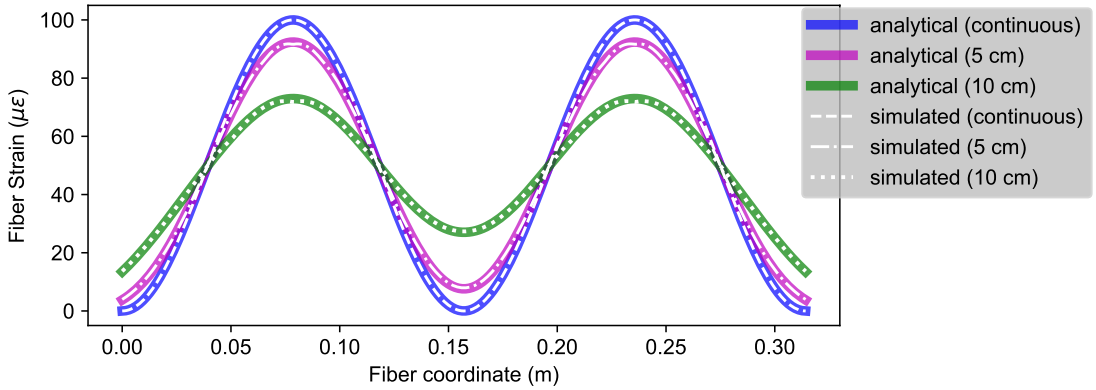

Figure 3.4: Fiber strains from uniform strain $\varepsilon_{xx} = 100\,\mu\varepsilon$. The plot shows analytical and numerical solutions for continuous (on-point), and moving average with $5\,\mathrm{cm}$ and $10\,\mathrm{cm}$ windows.

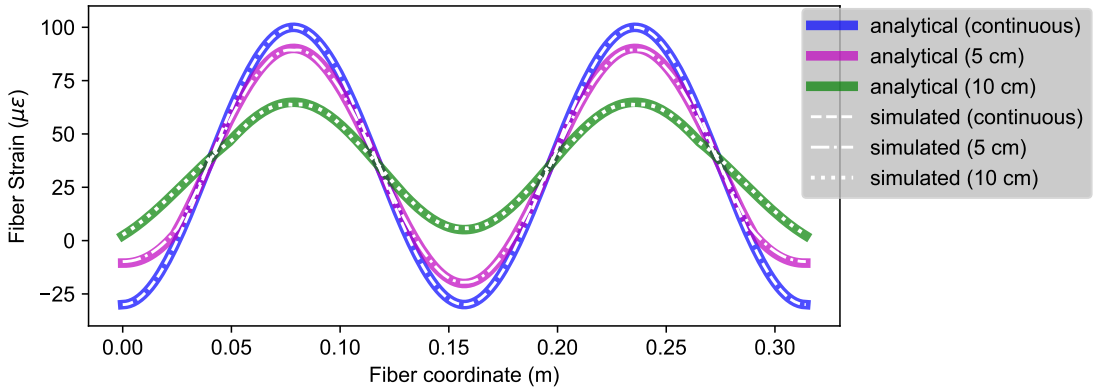

Figure 3.5: Fiber strains from biaxial strain $\varepsilon_{xx} = 100\,\mu\varepsilon$ and $\varepsilon_{yy} = -30\,\mu\varepsilon$.

results shown in Fig. 3.5, two important observations can be made. Firstly, since the fiber strains vary from $-30\,\mu\varepsilon$ to $100\,\mu\varepsilon$, they have to pass through zero at some points. Those points are where positive and negative terms cancel out even though the surface strain is nowhere zero. Secondly, it can be seen that the moving average fiber strains with $10\,\mathrm{cm}$ window are all positive which illustrates that relatively large averaging windows cannot resolve quick variations in the underlying surface strains.

What about shear strains? Equation (3.7) shows that shear strains can be detected by the fiber. To verify that, a pure shear of $\varepsilon_{xy} = 100\,\mu\varepsilon$ is applied to the plate. The analytical solution for fiber strains is $\varepsilon_f = -2\varepsilon_{xy}\sin\theta\cos\theta$ and the results are shown in Fig. 3.6. In fact, all shear strains (and all strain states) can be mapped into normal strains in the principal coordinate system. For the current case of pure shear, the two principal strain directions are $45°$ and $135°$ to X-axis. The fiber points in these directions

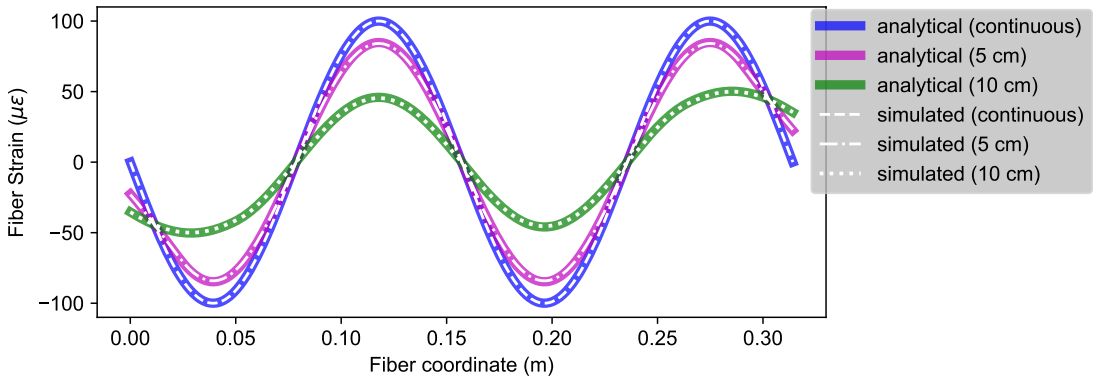

Figure 3.6: Fiber strains from pure shear $\varepsilon_{xy} = 100\,\mu\varepsilon$.

correspond to maximum and minimum fiber strains with their magnitude matching the absolute value of shear strain. In all scenarios, fiber is the most sensitive to the normal strain component that is parallel to the fiber direction.

3.2.4 Merits of Integrated IGA-DFOS

One might wonder what is the advantage of using IGA-DFOS over existing methods. As described in the previous chapters, the merit of IGA is the ability to use exact CAD data directly and the lower effort of setting up the analysis model. The benefits of DFOS are also discussed in Section 1.2 and summarized in Table 3.1. The integrated IGA-DFOS model combines the advantages of both since the fiber model is developed under the same principles as IGA while keeping the practical considerations in mind.

DFOS	Strain Gauge
Distributed measurement data	Discrete sensors for multiple locations
High spatial resolution	Single point measurement
Long range (25 km) in a single fiber	Needs signal multiplexers
Stable in harsh environments	

Table 3.1: Comparison of DFOS and strain gauges

The existing SHM methods, even the ones using IGA, are based on strain readings from point sensors (strain gauges) [32]. This requires accurate positioning of strain gauges between the digital model and real world. In models which assume strain gauge at the center of each element, the structure mesh is tied to the strain gauge positions making mesh generation cumbersome. To relax this constraint, the strain gauge readings can be interpolated to element centroids [52] but it is not straightforward if the direction of strain gauges is changing. Complexity of sensor instrumentation is another problem

as the number of sensors increases. Some studies suggested the optimization of sensor placement to minimize the number of sensors based on predicted deformation modes [53] but it usually requires large mesh sizes to accommodate fewer sensors.

The IGA-DFOS model is independent of the structure mesh and the fiber. The sampling point locations are calculated automatically based on fiber geometry and sampling interval. It is also easier to calibrate the fiber coordinates from a few known distances. Sensitivity of the fiber can be studied during the design cycle from the IGA simulations. Hence, the isogeometric approach combined with high efficiency of IGA offers a potential for a design-analyze-refine workflow.

3.3 Application of Integrated IGA and DFOS

In this section, an application example of the fiber model and IGA for elastic stress-strain analysis is presented to demonstrate the feasibility of the integrated IGA-DFOS model. The DFOS fiber strains are experimentally measured from the deformation of a cylindrical pipe, and then simulated fiber strains are compared with experiment results. The objective of this study is to predict the amount of ovalization (deviation from circular cross section) of the cylindrical pipe using the fiber strain measurements.

3.3.1 Experimental setup

The schematics of the experimental setup is illustrated in Fig. 3.7, and the actual model is s hown in Fig. 3.8. The pipe has a $300\,\mathrm{mm}$ outer diameter with $5\,\mathrm{mm}$ thickness, and made of PVC material with a Young's modulus of $2.8\,\mathrm{GPa}$ and Poisson's ratio of 0.3. The DFOS fiber is wrapped around the pipe's outer surface in four loops with a pitch of $33\,\mathrm{mm}$ and a protective tape was placed over it. The horizontal loading was applied by turning a threaded rod at the mid-section of the pipe, and a pair of rectangular beams distributed the load along the pipe's length as shown in Fig. 3.8. This loading causes an oval deformation which induces surface strains on the outer surface of the pipe. The applied displacements were measured using two dial gauges on the opposite sides of the pipe. DFOS strain data was measured by a Neubrescope (NBX7031) instrument using Rayleigh backscattering (RBS) in $1\,\mathrm{cm}$ intervals under Tunable Wavelength Coherent Optical Time Domain Reflectometry (TW-COTDR) mode [21] for temperature compensated strain measurements.

In order to calibrate the fiber coordinates in the simulation, four fiber locations on the top surface of the pipe were marked from the initial calibration measurements. The fiber coordinate at a particular point was obtained by spot-heating the desired location

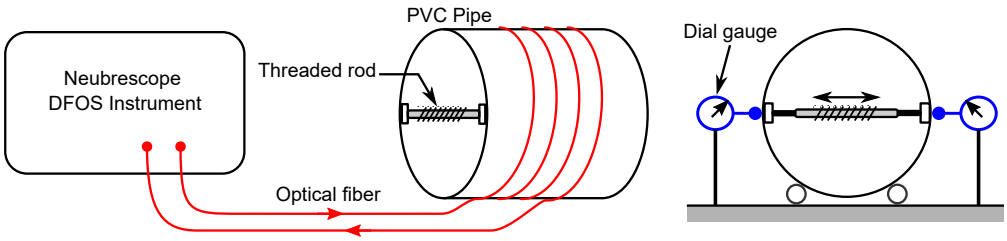

Figure 3.7: Schematics of experiment setup

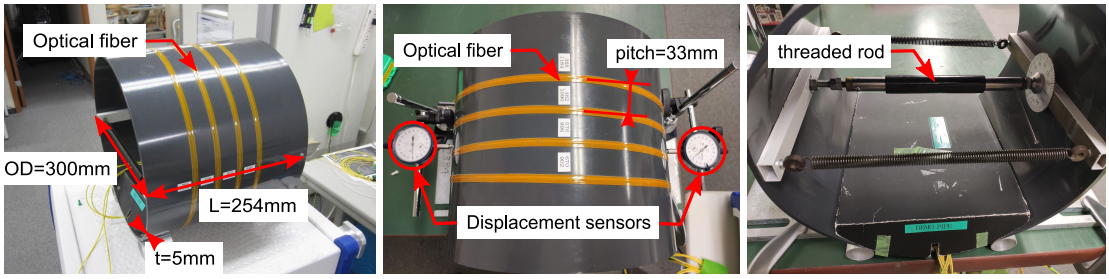

Figure 3.8: The pipe dimensions and experiment setup showing optical fiber, displacement sensors and threaded rod

which can be detected as the change in backscattering frequency at the corresponding coordinate.

3.3.2 Experimental procedure

The experiment was performed at five different prescribed displacements (designated as M1 to M5) from the threaded rod to evaluate the response of the fiber strains with respect to the deformation of the pipe. Table 3.2 shows the experimental parameters such as sampling interval. The spatial resolution determines the length of moving average window between consecutive fiber strain measurements.

Before the experiment, a calibration reading was performed to establish the reference fiber strain distribution in undeformed state of the pipe. Next, the required

Optical technology	TW-COTDR
Fiber type	Single mode optical fiber
Sampling interval	1 cm
Spatial resolution	2 cm
Averaging count	16
Strain range	$-15\,000\,\mu\varepsilon$ to $20\,000\,\mu\varepsilon$
Repeatability	$\pm 0.2\,\mu\varepsilon / 0.01\,^{\circ}\mathrm{C}$

Table 3.2: Measurement parameters in the experiment

amount of displacement was applied incrementally by turning the threaded rod. The net prescribed displacement was taken as the average of the two dial-gauge readings. This displacement caused the pipe to deform in an oval shape, which was detected by the optical fiber as 1D fiber strains. The fiber strain readings were recorded and the reference strain was subtracted from the measured fiber strains to obtain the net fiber strains (strain change). This process was repeated for all load cases by increasing the stroke to obtain the respective fiber strain distributions [54].

3.3.3 Experimental results

Figure 3.9 shows the experimentally measured fiber strains plotted against the fiber coordinates for five load cases. The data shows the net strains which is the difference between loaded and reference strains. Only the data in the region of interest, fiber length from $2.5\,\mathrm{m}$ to $6.5\,\mathrm{m}$ are plotted. It can be clearly seen that the strains oscillate between positive and negative since the oval deformation causes tensile and compressive surface strains on outer surface of the pipe. As expected, bigger displacements produce bigger magnitude of fiber strains. We can also see the experiment data has some noise around $10\,\mu\varepsilon$ which is expected at the high resolution mode. Although the noise error can be improved using larger averaging windows, the small scale of the model warrants high spatial resolution.

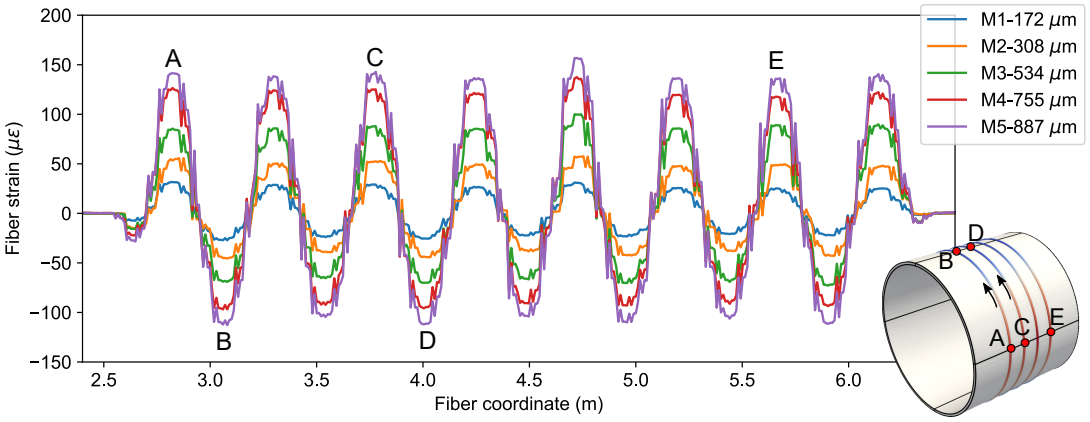

Figure 3.9: Fiber strain measurement data from experiments. A-E corresponds to the approximate locations on the pipe.

In order to check whether the fiber strains have a linear response to applied displacements, the absolute maximum values are plotted against the displacements in Fig. 3.10. It can be seen that the magnitudes of fiber strains follow the linear trend with respect to the displacements within the range of the experiments. This justifies the use of a linear model for the prediction of fiber strains.

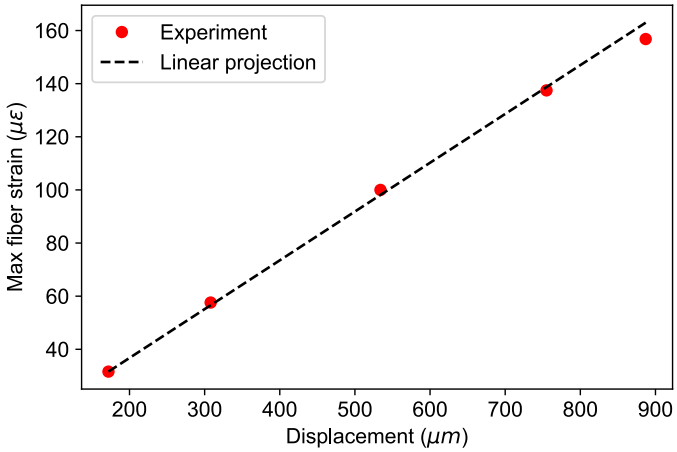

Figure 3.10: Response of fiber strains on applied displacement to the pipe

3.3.4 Simulation model

In this section, the displacement-induced fiber strains will be predicted using linear elastic IGA and developed fiber mesh model. The numerical model includes the pipe geometry, fiber curve, boundary conditions, material properties and DFOS measurement parameters.

The basic NURBS geometry for the pipe, a hollow cylinder, is shown in Fig. 3.11(a). It is a second order, single patch solid with 81 control points (27 in radial direction and 3 in axial direction). Due to the tensor product structure of NURBS, it can be imagined as bending a plate until the two edges meet to get a cylinder. The basic geometry is subdivided by h-refinement to create a finer IGA mesh as in Fig. 3.11(b) which increases the number of control points to 2205 and hence the total DOF to 6615. The fiber geometry is a second order helix-shaped NURBS curve with 33 control points.

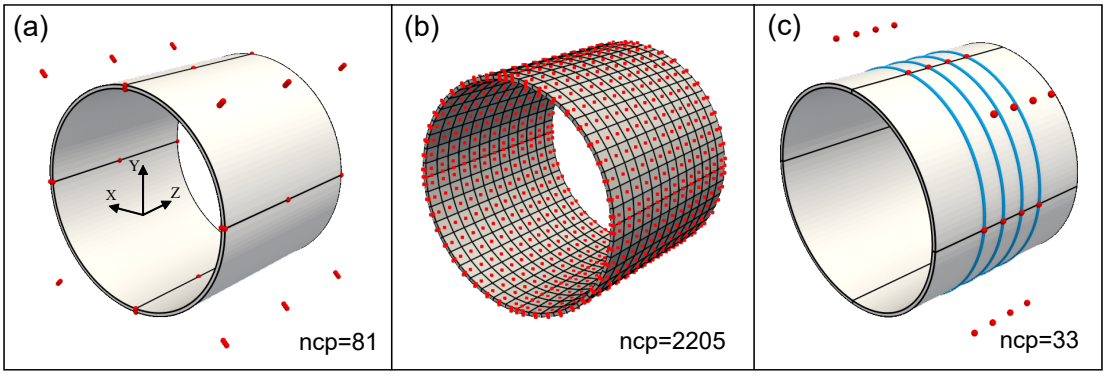

Figure 3.11: (a) Pipe geometry and control points (red points). Black lines show C^0 continuity; (b) Analysis mesh and control points after h-refinement; (c) fiber curve (in blue) with its control points

The pipe model is fixed at YZ plane along the C^0 continuous bottom edge as shown in Fig. 3.12 to prevent rigid body motion. Radial unit displacement $u_x = \pm 0.5$ is applied symmetrically across the diameter of the pipe. The prescribed displacements can be directly applied to the control points at such locations since they are interpolatory at C^0 lines/surfaces. The DFOS parameters, sampling interval and spatial resolution, are the same as Table 3.2.

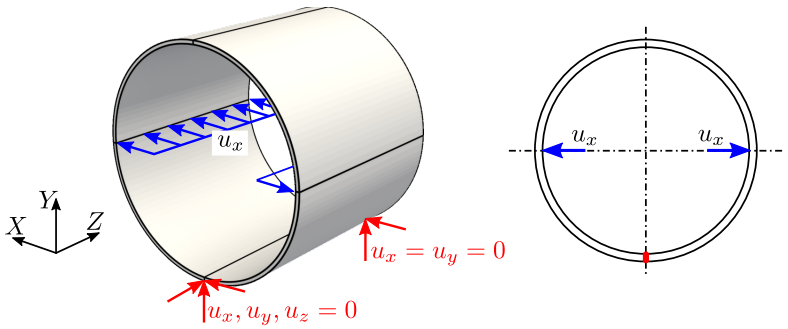

Figure 3.12: Idealized Boundary conditions for the pipe model

The input file for elastic JWRIAN-IGA includes the basic geometry information of control points, knots, boundary conditions and control parameters for mesh refinement. The linear elastic IGA computation is followed by the fiber strains calculation using the methodology described in Section 3.2.2.

3.4 Results and Discussion

Figure 3.13 shows the simulated normal strains ε_{xx} and ε_{yy} distribution in the pipe, and the 1D fiber strain distribution along the fiber. The magnitude of fiber strains have strong correlation with normal strain components near $(\pm r, 0)$ and $(0, \pm r)$ intercepts where the fiber tangent is nearly parallel to the coordinate axes. However, they are not identical because the fiber is not perfectly parallel to the axes and because of the moving average effect.

Figure 3.14 and Fig. 3.15 shows the comparison of fiber strains between simulation and experiment for case M3 and M4, respectively. Exploiting the linearity of the solution, the solution from the unit load was multiplied by the actual displacement value to obtain the corresponding fiber strains. The fiber coordinates from the experiment were adjusted to match those of the simulation. The plots show that the simulated data closely follows the experiment's trend, but the peak values of tensile strains in the simulation are slightly higher than those in the experiment. The reason for this discrepancy may be the idealized concentrated loading in the simulation in contrast to more distributed

loading in the experiment. The concentrated loading caused a sharp peak in the strain distribution, which consequently affected the one-dimensional fiber strain. Moreover, the loading may not have been uniform along the length of the pipe as assumed in the simulation.

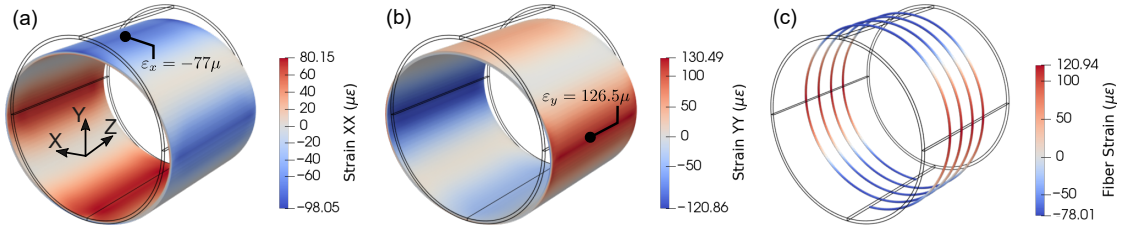

Figure 3.13: Normal strains distributions on the pipe from IGA: (a) strain-XX and (b) strain-YY; (c) simulated fiber strain distribution

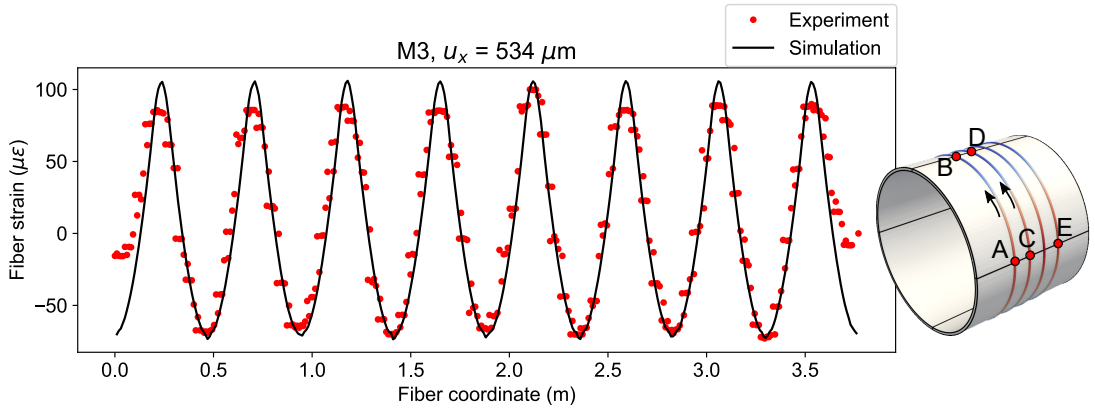

Figure 3.14: Comparison of fiber strains between simulation and experiment for $u_x = 534\,\mu\text{m}$

3.5 Estimation of loading conditions from DFOS measurements

A potential application of integrated DFOS and simulation model is the estimation of loading conditions in real time using measurement data. This can be achieved by matching the observed fiber strains with simulated ones by various candidates of loading conditions. This section presents a preliminary study on the estimation of loading conditions from DFOS measurements. An optimization approach can be used to estimate the boundary conditions by minimizing the discrepancy between observed and simulated fiber strains. It's important to note that an exact reproduction of loading conditions is not achievable since Eq. (3.5) used for calculating fiber strains is irreversible.

To estimate the loading conditions on the pipe, a pressure distribution was assumed

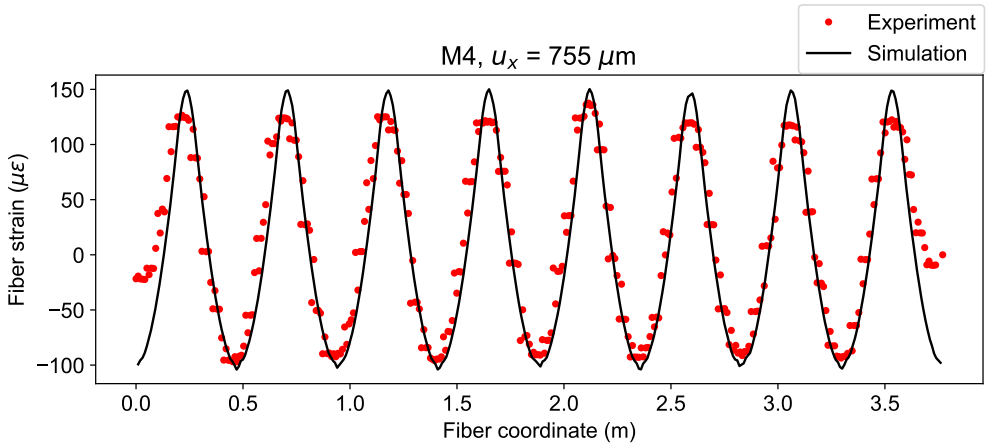

Figure 3.15: Comparison of fiber strains between simulation and experiment for $u_x = 755\,\mu\text{m}$

on the surface area of the pipe that is in contact with the rectangular bars (Fig. 3.8). The variation of pressure along the length (Z) direction of the pipe was represented with a second order B-spline function with five coefficients as free parameters, as shown in Fig. 3.16. A prescribed pressure is preferred over prescribed displacements because the latter imposes hard constraints on the flexibility of a structure, which could lead to spurious local strain concentrations.

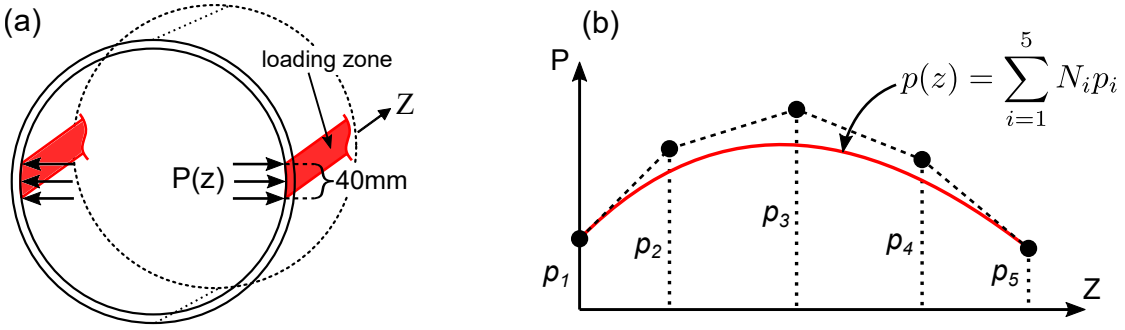

Figure 3.16: (a) Pressure application and loading zone; (b) Parametrization of the pressure distribution function along Z-direction; p_i are free parameters which influence the shape of $p(z)$

The objective function E for the optimization problem is defined as the sum of squared errors between the observed and simulated fiber strains at the measurement locations:

$$E = \sum_{i=1}^{n_s} \left(\varepsilon_{fi}^* - \varepsilon_{fi}\right)^2, \tag{3.14}$$

where ε_{fi}^* and ε_{fi} refer to measured and simulated fiber strains respectively, and n_s is

the total number of sampling points. The error function E was minimized by optimizing the parameters p_i of the pressure distribution function to obtain the best-fit solution. Sequential least squares programming (SLSQP), a gradient-based quadratic optimization method suitable for a small number of parameters, was used to solve the minimization problem. The termination criterion for the optimization was set as $\Delta E < 10^{-4}\ (\mu\varepsilon)^2$ between successive iterations.

As a representative case study, the measured fiber strains from the case M3 were used to run the optimization. Convergence was quickly achieved after fifth iteration and involved a total of 31 objective function evaluations including numerical finite difference calculations. Figure 3.17 shows the resulting pressure distributions after optimization, and Fig. 3.18 shows the fiber strains obtained from the simulation with the optimized pressure. The optimized pressure was found to be higher in the middle part of the pipe which is reasonable from the experimental conditions. This can be attributed to the bending of the rectangular beams during the experiment (Fig. 3.8), which could have resulted in non-uniform loading along the pipe.

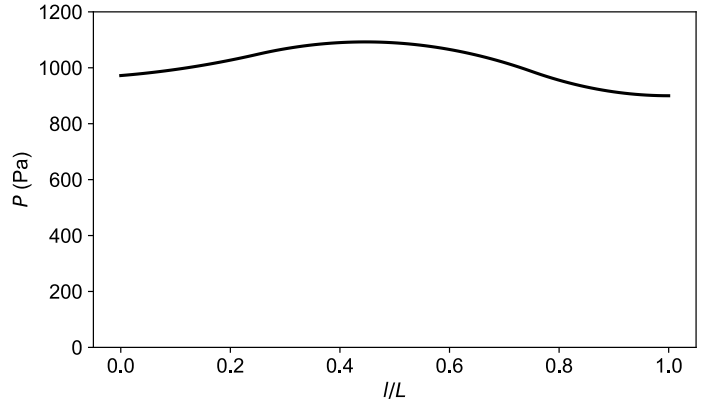

Figure 3.17: Optimized pressure distribution along the longitudinal direction of the pipe

Table 3.3 shows the root-means-square (RMS) and maximum error statistics between uniform and optimized loadings. The optimized loading conditions result in half of fiber strain errors from the idealized uniform loading in the previous section. The average displacement error from optimized loading and the ground truth was less than $4\,\%$, which demonstrates the efficacy of using the IGA-DFOS model for estimating the unknown loading conditions.

The parametrization of the loading (pressure distribution) from Fig. 3.16 is not unique since a different number of coefficients could be used. The choice of parametrization can affect the search space of possible loading distributions and hence must be

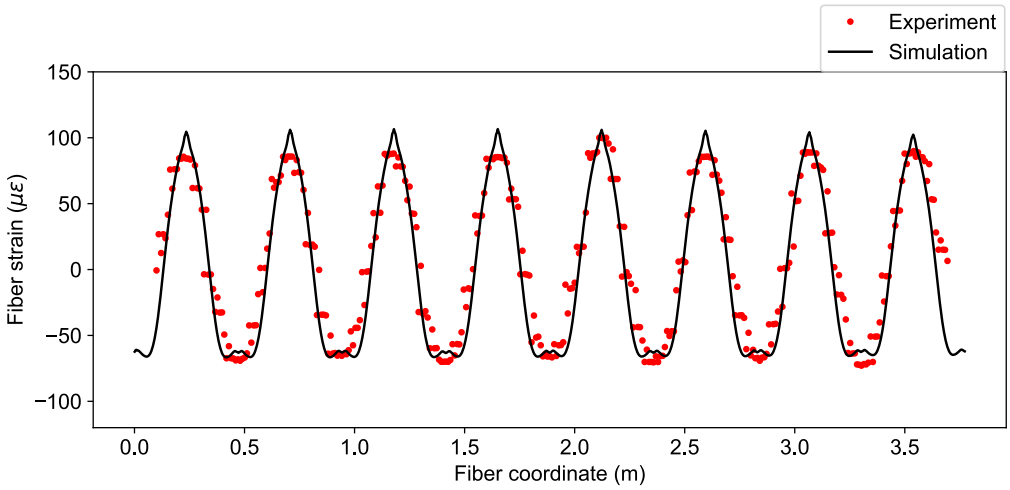

Figure 3.18: Fiber strains reproduced using the optimized pressure distribution

	Uniform loading	**Optimized loading**
RMS fiber strain error	$13.421\,\mu\varepsilon$ $(7.32\,\%)$	$5.863\,\mu\varepsilon$ $(3.19\,\%)$
Max fiber strain error	$30.539\,\mu\varepsilon$ $(16.65\,\%)$	$16.25\,\mu\varepsilon$ $(8.86\,\%)$
Average displacement error	-	$3.91\,\%$

Table 3.3: Comparison of errors between uniform and optimized loading conditions

chosen considering practicality and computation time. In the present model, it was found that five coefficients were adequate to replicate the optimal loading distribution in Fig. 3.17. Another caveat of this approach is the requirement of the initial knowledge of the loading zone. If such information is not available, the loading zone has to be inferred from the observed fiber strains when setting up the optimization problem.

3.6 Summary

In this chapter, a conceptual and numerical model of DFOS fiber was presented and integrated with isogeometric analysis to derive the analytical fiber strains. The developed fiber model combines the geometric accuracy of IGA and versatility of DFOS into a single framework. The properties of the numerical fiber strains were investigated with a validation model under simplified strain states. An experimental model of a cylindrical pipe was used to measure fiber strains during deformation and the results are compared with the numerical simulation. The simulation results with assumed loading conditions showed that the numerical model can closely replicate the experimentally measured fiber strains except in the peak regions.

The numerical model was then used to estimate the loading conditions from the

measured fiber strains via optimization. The fiber strain errors reduced in half (from $7\,\%$ to $3\,\%$) after optimization and the resulting displacement error is less than $4\,\%$ to ground truth. The results show that the methodology can estimate loading conditions with good accuracy in real time, which can be used for structural health monitoring and damage detection. The estimation of loadings however require the prior knowledge of possible loading zones so that proper parameters can be used in optimization.

Chapter 4

Development of Inverse IGA for Structural Monitoring

4.1 Introduction

The previous chapter illustrated that the structural response and loading conditions can be estimated using an optimization approach. However, constructing such an optimization model requires prior knowledge of loading conditions such as the location and direction of applied forces. In addition, setting up and iteratively solving the optimization problem can be time consuming for complex structures. In this chapter, a one-step inverse IGA method for the estimation of deformation and stress distribution from DFOS fiber strains for linear elastic structures will be presented. 'One-step' refers to the type of inverse solver which calculates the solution in single flow (i.e, non-iteratively). The following literature review and the comparison with state-of-the-art will show that the proposed method is a logical step in terms of versatility and accuracy.

This chapter is organized as follows. Firstly, existing literature on inverse methods with FEM/IGA under the context of solid mechanics/structural analysis will be reviewed. Then, the overview of the proposed inverse IGA and merits over the existing methods will be explained. Next, the mathematical formulation of the method is described followed by numerical validations. The fiber mesh model from the previous chapter is used as a base for the development of this method. Finally, the new inverse IGA-DFOS is applied to a practical example to predict the deformation of a flat-plate impeller under rotation.

Numerous techniques for determining the structure state based on measured strains can be found in literature. One such approach, called Ko's Displacement Theory, was

developed by Ko et al. is based on Euler-Bernoulli beam theory [55]. Ko's theory has been applied to aerospace structures such as beams, wing boxes and slender plates [56], [57]. This model calculates deflections along a beam by integrating axial strains measured along a line at a known distance from the neutral axis. Another approach for finding beam deflections is the Modal Method, which fits the coefficients of known mode shapes to observed axial strains [58], [59]. The accuracy of this approach is influenced by sensor placement and number of modes, and requires generating mode shapes in advance from experiments or FEM simulations. On the other hand, a type of transformation methods based on Neural Networks have also been proposed for inverse shape reconstruction from measurements but they are not as prominent because of the need for large amount of training data and the lack of generality [60], [61].

4.1.1 Inverse Finite Element Method

A promising methodology for the generalized inverse analysis of structures is to utilize finite element method and extend it to use measured strains instead of prescribed loading conditions. It can be done in principle by modifying the variational equations at the heart of FEM. One such method is the inverse Finite Element Method (iFEM) invented by Tessler and Spangler et al. [33], [62]. This method, initially developed for plate and shell structures, uses C^0-continuous finite element shape functions and a weighed least-squares variational functional to minimize the error between the analytical and measured surface strains. Since iFEM is based on finite element formulation, several variations of inverse finite elements have been proposed such as-

- three-node inverse shell element iMIN3 with six degrees-of-freedom per node [32],
- quadrilateral shell iQS4 [63],
- eight-node second-order curved shell element using curvilinear coordinates iCS8 [64],
- inverse Timoshenko beam [65], and
- refined zigzag theory for composite structures [53], [66].

A comparative study of iMIN3, iQS4 and iCS8 elements were conducted by Abdollahzadeh et al. using numerical benchmark problems [67]. The iFEM elements have been applied to full-surface field inverse displacement reconstruction of wing shaped plates [30], [31], [53], cylindrical structures [64], wind turbines [68], plate structures [52] and frame structures [69]. Prior studies have shown that iFEM outperforms other competing methods such as Ko's theory, Modal Method, and Neural Networks [70]. The iFEM approach is adaptable to any geometry and sensor placement, with strain rosettes

and Fiber Bragg Grating (FBG) as commonly used sensors. The standard iFEM formulation assumes at least one strain sensor on each element's centroid but it is not feasible in practice to put strain sensors or rosettes on every element in the FEM mesh. To solve this issue, iFEM employs a *weighted* least-squares method and assigns very small weight values where strain measurements are absent in order to regularize the solution.

4.1.2 Drawbacks of iFEM, IGA as savior

The drawbacks of iFEM as opposed to other shape sensing systems are complex sensor configuration and time-consuming development of analysis models due to coupling between FEM mesh and actual sensor placement. Isogeometric Analysis (IGA) is a perfect candidate to tackle these issues since it utilizes Computer-Aided Design (CAD) geometry to streamline the preprocessing of finite element analysis (FEA) models.

Despite the rising popularity of iFEM and IGA by themselves, application of IGA for shape sensing purpose has been relatively few. Kefal et al. [71] extended iFEM formulation using NURBS basis functions in the Isogeometric iFEM method with strain rosettes. The developed IGA-iFEM method was recently applied to cylindrical marine structures [64]. Furthermore, IGA-iFEM has been applied to shape sensing of beam structures. Zaho et al. [72] used NURBS based functions for shape sensing of variable cross-section beams and Chen et al. [65] applied IGA to derive inverse equations for Timoshenko beams under complex loading. The aforementioned iFEM and IGA formulations commonly use point sensors such as strain rosettes attached to each element.

4.1.3 Proposed method

This study presents a new integrated framework for inverse Isogeometric Analysis (IGA) and Distributed Fiber Optic Sensing (DFOS) fiber model to calculate full-field inverse displacement for linear elastic structures. The method uses a least-squares variational formulation and NURBS functions to model both the structure and strain fiber geometry. Displacement variables are discretized using standard IGA formulation with rotation-free control points. Then, strain-displacement relations are used to find constraint conditions to measured strain data along the fiber. Unlike existing iFEM formulations, this approach does not require weight values and uses minimum potential energy principle to regularize the structure's shape.

The proposed method has two main benefits: it allows for the input of structure and fiber geometries from CAD models and can adapt to the distributed sensing parameters such as spatial resolution and sampling locations to match the measurement mode of DFOS instrument. This isogeometric approach is advantageous as the CAD data of the

structure and DFOS fiber should already be available after the design and planning phase. Moreover, the sensing parameters can be adjusted based on the required spatial resolution, accuracy, and sampling frequency without changing the inverse IGA model. This greatly enhances the practical application of Structural Health Monitoring (SHM).

4.2 Formulation of Inverse IGA-DFOS

The inverse IGA-DFOS is formulated as an optimization problem which minimizes the difference between measured and reproduced fiber strains. The variables to be optimized are the displacement DOFs of the control points in the inverse IGA mesh. The control point displacements are then used to interpolate the full displacement field and strain/stress field in the monitored (solid) structure.

4.2.1 Revisiting DFOS fiber mesh model

The formulation and verification of the DFOS fiber mesh is described in the previous chapter (Section 3.2.1). Two important equations for fiber strain projection Eq. (3.7) and moving average fiber strains Eq. (3.10), are repeated below for convenience:

$$\varepsilon_f = \boldsymbol{t}^T \varepsilon, \tag{4.1}$$

$$\overline{\varepsilon}_f(s) = \frac{1}{\Delta s} \int_{s-\frac{\Delta s}{2}}^{s+\frac{\Delta s}{2}} \varepsilon_f(s)\, ds. \tag{4.2}$$

4.2.2 Least-squares objective

The objective function of the inverse IGA-DFOS is defined as the sum of squared difference between the measured and reproduced fiber strains.

$$\mathcal{L} = \frac{1}{2} \sum_{i=1}^{n_s} \left(\varepsilon_{fi}^* - \varepsilon_{fi}\right)^2, \tag{4.3}$$

where n_s is the total number of fiber strain sampling points, ε_{fi}^* is the measured fiber strain, and ε_{fi} is the analytical fiber strain at the i^{th} sampling point. The reproduced fiber strain is calculated from the displacement field in the solid structure using the inverse IGA mesh. From Eq. (4.1), the reproduced fiber strain is given by:

$$\varepsilon_{fi} = \boldsymbol{t}^T \boldsymbol{B} \boldsymbol{d}, \tag{4.4}$$

which, after substituting into Eq. (4.3), gives the objective function in terms of optimization variables $\boldsymbol{d}$:

$$\min_{\boldsymbol{d}\in\mathbb{R}^n} \mathcal{L} = \frac{1}{2}\sum_{i=1}^{n_s} \left[\varepsilon_{fi}^* - \left(\boldsymbol{t}^T\boldsymbol{B}\boldsymbol{d}\right)_i\right]^2. \tag{4.5}$$

Differentiating Eq. (4.5) with respect to $\boldsymbol{d}$ and setting the derivative to zero,

$$\frac{\partial \mathcal{L}}{\partial \boldsymbol{d}} = 0, \tag{4.6}$$

$$\sum_{i=1}^{n_s} \left(\boldsymbol{B}^T\boldsymbol{t}\right)_i \left[\varepsilon_{fi}^* - \left(\boldsymbol{t}^T\boldsymbol{B}\boldsymbol{d}\right)_i\right] = 0, \tag{4.7}$$

$$\sum_{i=1}^{n_s} \left(\boldsymbol{B}^T\boldsymbol{t}\boldsymbol{t}^T\boldsymbol{B}\right)_i \boldsymbol{d} = \sum_{i=1}^{n_s} \left(\boldsymbol{B}^T\boldsymbol{t}\varepsilon_f^*\right)_i. \tag{4.8}$$

Eq. (4.8) represents the *optimality conditions* which must be satisfied in order to solve the least-squares objective in Eq. (4.3). The locality of basis functions implies that each term in the summation can be evaluated element-wise and assembled into the global system using connectivity information.

4.2.3 Isogeometric least-squares fit

The Isogeometric least-squares fit estimates the deformation of a structure from measured surface strains without the information of loading conditions. This is done based on isogeometric framework of structure and fiber as described in Section 4.1.3. In this section, the least-squares objective with analytical fiber strains is combined with isogeometric analysis to derive the global system of equations.

The total potential energy in a structural system has been given in Section 2.5. This equation includes terms for internal energy and external work done by body forces and surface tractions. The least-squares objective can be added to the total potential energy as a constraint to form a new functional:

$$\Pi = \frac{1}{2}\int_\Omega \boldsymbol{\sigma}^T\boldsymbol{\varepsilon}\,\mathrm{d}\Omega - \int_\Omega \boldsymbol{b}^T\boldsymbol{u}\,\mathrm{d}\Omega - \int_\Gamma \boldsymbol{h}^T\boldsymbol{u}\,\mathrm{d}\Gamma + \frac{1}{2}\lambda\sum_{i=1}^{n_s}\left(\varepsilon_{fi}^* - \varepsilon_{fi}\right)^2, \tag{4.9}$$

where λ is the penalty parameter for the constraint. For multi-patch problems, it is extended to include the coupling terms between patches (Section 2.6). Then, the new

functional is given by:

$$\Pi = \frac{1}{2}\int_{\Omega} \boldsymbol{\sigma}^T \boldsymbol{\varepsilon}\, \mathrm{d}\Omega - \int_{\Omega} \boldsymbol{b}^T \boldsymbol{u}\, \mathrm{d}\Omega - \int_{\Gamma} \boldsymbol{h}^T \boldsymbol{u}\, \mathrm{d}\Gamma + \frac{1}{2}\beta \int_{\Gamma_U} \boldsymbol{u}^T \boldsymbol{u}\, \mathrm{d}\Gamma_U + \frac{1}{2}\lambda \sum_{i=1}^{n_s} \left(\varepsilon_{fi}^* - \varepsilon_{fi}\right)^2 . \tag{4.10}$$

Minimizing this functional will simultaneously minimize the potential energy and fiber strain differences assuming appropriate value of λ is used. One might be curious why it is necessary to minimize the potential energy on top of least-squares objective. The reason is that the least-squares objective alone is not sufficient to determine the displacement field. It is a necessary condition which must be satisfied by the displacement variables. However, the displacement field can be any arbitrary function which satisfies the constraint. Therefore, total potential energy is added to the functional to ensure that the displacement field is physically meaningful. In other words, limited measurements from strain rosettes or optical fibers create an ill-posed and unstable system which necessitates a regularization method to prevent undesirable displacement distributions. Previous approaches employed weighting coefficients which were adjusted based on the availability and reliability of the measurements [33], [64]. This required pre-determining weight values in order to accurately interpolate the known data points. In this study, the minimum strain energy principle is applied as an alternative approach.

Following the usual discretization scheme and differentiating with respect to the displacement variables $\boldsymbol{d}$, the final form of matrices is obtained:

$$\left[\boldsymbol{K} + \lambda \sum_{i=1}^{n_s} \left(\boldsymbol{B}^T \boldsymbol{t}\boldsymbol{t}^T \boldsymbol{B}\right)_i\right] \boldsymbol{d} = \lambda \sum_{i=1}^{n_s} \left(\boldsymbol{B}^T \boldsymbol{t} \varepsilon_f^*\right)_i . \tag{4.11}$$

The unknown external force term is removed from the equation by setting $\boldsymbol{f} = \boldsymbol{0}$. Eq. (4.11) is the coupled system of equations which must be solved to obtain the displacement variables $\boldsymbol{d}$. Using the solution from Eq. (4.11), the full field displacement, strain and stress distributions can be calculated from Eqs. (2.31) and (2.32). If the moving average effect from Eq. (4.2) is considered, the equations become:

$$\left[\boldsymbol{K} + \frac{\lambda}{\Delta s} \sum_{i=1}^{n_s} \int_{\Delta s^-}^{\Delta s^+} \left(\boldsymbol{B}^T \boldsymbol{t}\boldsymbol{t}^T \boldsymbol{B}\right)_i \mathrm{d}s\right] \boldsymbol{d} = \frac{\lambda}{\Delta s} \sum_{i=1}^{n_s} \int_{\Delta s^-}^{\Delta s^+} \left(\boldsymbol{B}^T \boldsymbol{t} \varepsilon_f^*\right)_i \mathrm{d}s. \tag{4.12}$$

4.3 Validation of Inverse IGA-DFOS with Simulated Examples

In this section, the proposed inverse IGA-DFOS methodology is validated using four numerical examples of plate, hemisphere and cylinder geometries under various boundary conditions and loading conditions. In these examples, the reference solution and input

fiber strains were computed in prior using high-fidelity IGA simulations. The computed fiber strains and essential boundary conditions were then used as input for the inverse analysis. The benchmark examples were designed to examine the robustness of the formulation when applied to different geometries, loading conditions and deformation modes. Gravitational forces were ignored in the simulations but this did not affect the generalization of the conclusions drawn from the study. The linear elastic material model with Young's modulus of $200\,\mathrm{GPa}$ and Poisson's ratio of 0.3 was used in all simulations.

4.3.1 Plate under twisting load

The first example used for verification involves a flat plate that is clamped at one end and subjected to a twisting load at the other end as shown in Fig. 4.1 [73]. The plate and the DFOS fiber were modeled as second-order solid and curve NURBS geometries, respectively. A single continuous fiber is attached to both top and bottom sides of the plate to capture the bending and membrane strains. The fiber's complex shape can be modeled using only 20 control points for each side of the plate. The reference displacement field of the plate was computed using conventional IGA with a high-fidelity mesh of $20\,\mathrm{mm}$ subdivision size by knot insertion along X- and Y-axes. Then, fiber strains were computed using Eq. (4.4) from the forward solution's strain distribution and used as input for the inverse analysis. In the inverse analysis, only geometric boundary conditions were prescribed since the loading conditions were assumed to be unknown.

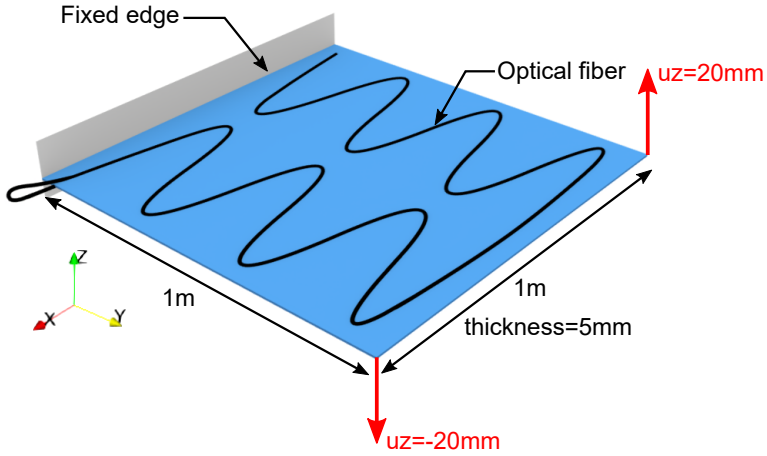

Figure 4.1: Plate with attached optical fiber, boundary conditions and prescribed displacements. The top side of the plate can be seen with the optical fiber running to the bottom side.

The sampling interval of the fiber was set at $50\,\mathrm{mm}$ and the mesh size of the inverse model was $100\,\mathrm{mm}$. There were 117 strain sampling points on each side of the plate.

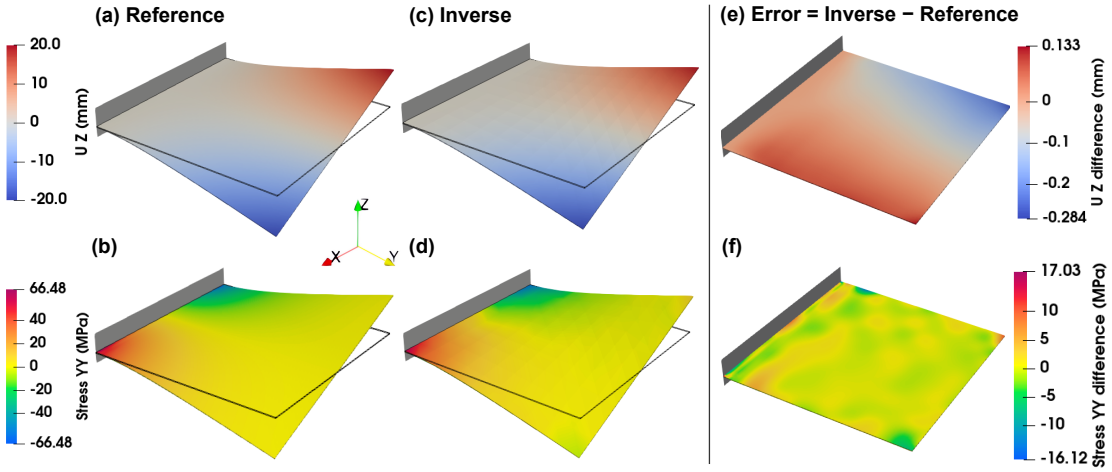

Figure 4.2: Solutions of plate twisting problem: (a, b) Displacement and stress fields of reference solution, (c, d) Displacement and stress fields of inverse solution, (e, f) Error distributions for displacement and stress of the inverse solution. The solutions were computed using fiber strain sampling interval of $50\,\mathrm{mm}$.

The inverse mesh size was selected to ensure the stability of the least-squares solution, with the number of displacement DOF in the IGA mesh being of the same order of magnitude as the number of strain sampling points. Figure 4.2 shows the comparison of the displacement and stress fields between the reference and inverse IGA. The results indicate that the twisting deformation and stress distribution can be reproduced with high accuracy by the inverse analysis. The Z-displacements at the loaded tips from the inverse solution are $-19.87\,\mathrm{mm}$ and $19.72\,\mathrm{mm}$, which translate to the errors of $0.65\,\%$ and $1.4\,\%$ respectively.

In order to check the accuracy of least-square fitting, the input and reproduced fiber strain distributions along the length of the fiber are plotted in Fig. 4.3. The comparison shows little difference between the two which means the fiber strains can be reproduced very well from the inversely computed displacement field. In practice, the true solution is generally not available and the accuracy of inverse solution can be judged from the fiber strain fitting.

The majority of computational effort in this method is dedicated to solving the simultaneous equations outlined in Eq. (4.11), which has the same level of complexity as solving the FE equations. The assembly of fiber strain matrices was a relatively quick process, taking only a few seconds on an Intel Core i7 machine. In contrast, the preparation of the FE model from CAD design and meshing is time consuming and the setup to calibrate strain gauges in conventional iFEM requires additional effort. Additionally, the measurement time of DFOS instruments increases proportionally with the number

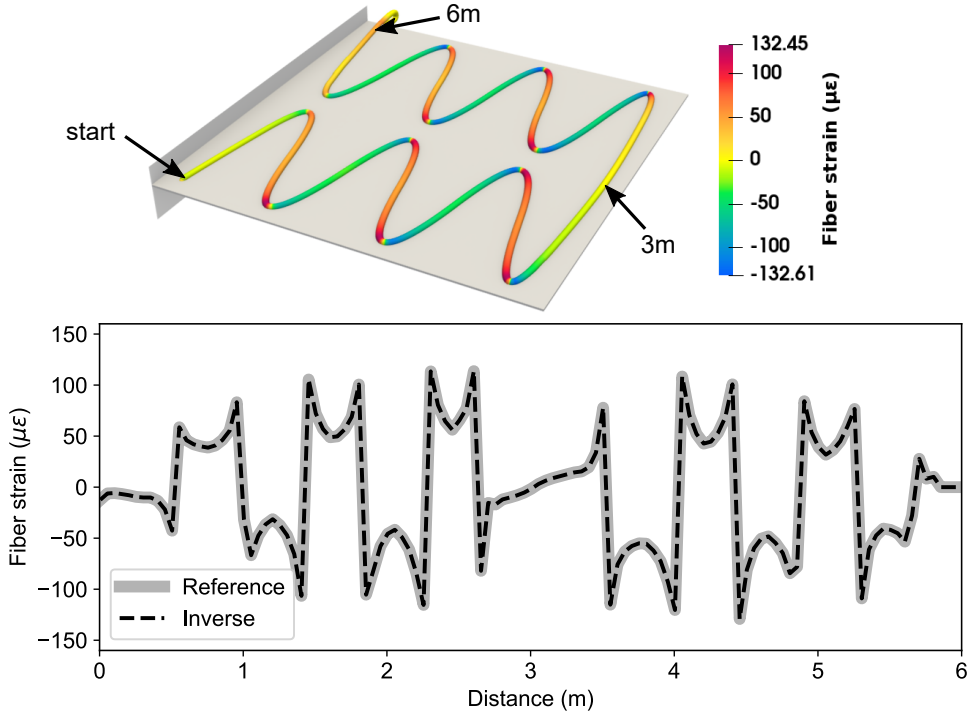

Figure 4.3: Comparison of reference (input) and reproduced fiber strains distributions at the bottom surface of the plate for the plate twisting problem. The jumps in fiber strains correspond to the rapid changes in tangent direction of the fiber curve. The fiber continues to the bottom side of the plate after $6\,\mathrm{m}$ with symmetric fiber strain distributions as the top side.

of sampling points, typically taking several minutes for a fiber of around $100\,\mathrm{m}$ in length with $2\,\mathrm{cm}$ intervals. Therefore, the current method has a comparable computational cost to the existing iFEM methods, but offers greater flexibility and a more efficient workflow due to its fully isogeometric framework.

4.3.2 Plate under bending load

In order to investigate the robustness of the inverse IGA-DFOS under different deformation modes, the boundary conditions on the previous model of plate and fiber geometries are changed to clamped edges on all sides and a uniformly distributed pressure of $10\,\mathrm{kPa}$ was applied to the top surface of the plate as shown in Fig. 4.4.

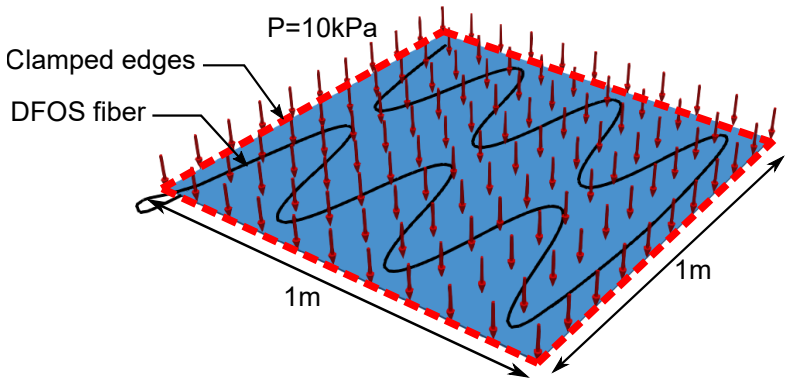

Figure 4.4: Geometry and boundary conditions of the plate bending problem. The plate is clamped (fixed) at all sides and a uniformly distributed pressure of 10kPa is applied to the top surface. The fiber layout is the same as in Fig. 4.1.

The reference solution for this problem was calculated using a mesh size of $20\,\mathrm{mm}$. The fiber strain sampling interval was $20\,\mathrm{mm}$ and the inverse IGA mesh size was $100\,\mathrm{mm}$. The reference and reproduced fiber strains are plotted in Fig. 4.5. The fiber strains show a very different distribution from the twisting mode, with less regularity due to oscillating surface strain between tension and compression.

Figure 4.6 shows the comparisons of reference and inverse solutions for the displacement and stress fields. The RMS relative displacement error and relative fiber strain error are $0.679\,\%$ and $0.715\,\%$ respectively. Hence, the results show that the inverse IGA-DFOS can accurately reproduce the fiber strains and displacement fields under different deformation modes. The average deviation in σ_{XX} between the inverse and reference solution is $3.77\,\mathrm{MPa}$ which is within $2.8\,\%$ of the absolute maximum stress, and the maximum error is $-34\,\mathrm{MPa}$ or $25\,\%$ of the absolute value. The maximum stress errors however are located near the edge of the plate where the fixed boundary induces high local stresses as can be seen in Fig. 4.6 (b, d). The absence of strain sampling points

near the vicinity of the local strain zones results in a large local error in the inverse solution. The distribution of stress errors are shown as a histogram in Fig. 4.7. The majority of the errors are within $10\,\%$ of the absolute value.

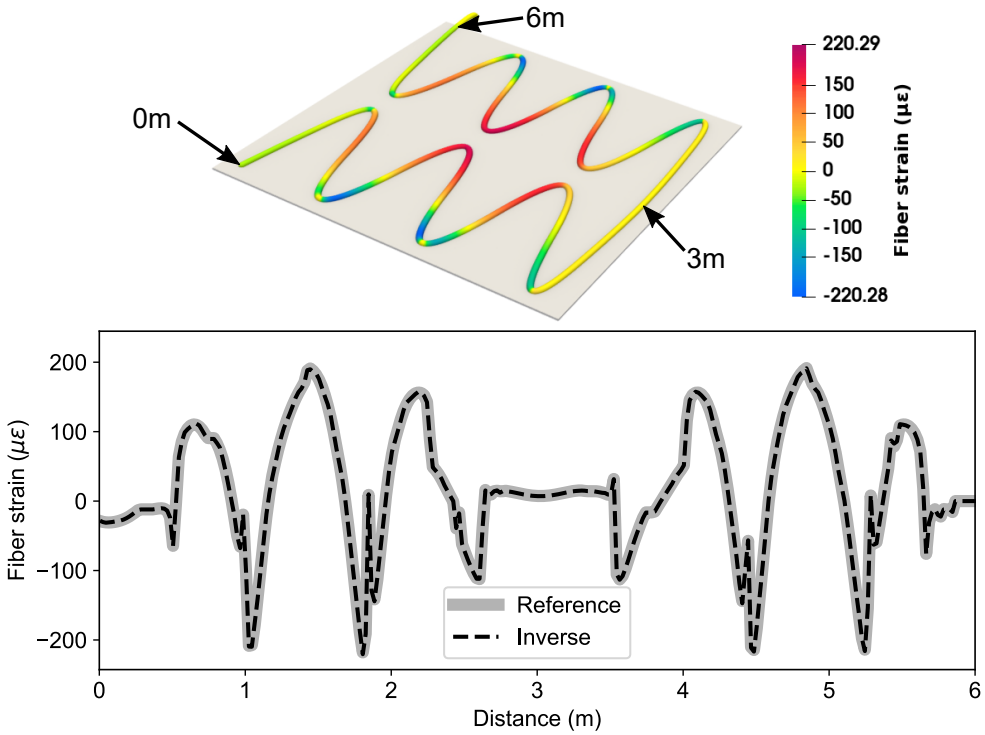

Figure 4.5: Comparison of input and reproduced fiber strains distribution for the plate bending problem (rendering shows the bottom side of the plate). The fiber continues to the top side of the plate after $6\,\mathrm{m}$ with symmetric fiber strain distributions as the bottom side.

4.3.3 Pinched hemisphere

The third validation model is a hemispherical shell under symmetric concentrated loads at the equator as shown in Fig. 4.8. The hemisphere has a thickness of $40\,\mathrm{mm}$ and a radius of $10\,\mathrm{m}$. It is fixed at the uppermost point to prevent rigid body motion. This model is considered as a benchmark problem for assessing the accuracy of IGA since FEM models for thin curved structures are prone to geometric imperfections which can be addressed by using exact geometry [4]. The hemisphere was modelled using third order functions along the surface and second order through thickness. The use of a mixed-order solid mesh helps prevent the locking phenomenon while maintaining the accuracy of through-thickness strain variation. Previous studies have shown that a single second order element through thickness is sufficient for IGA [3].

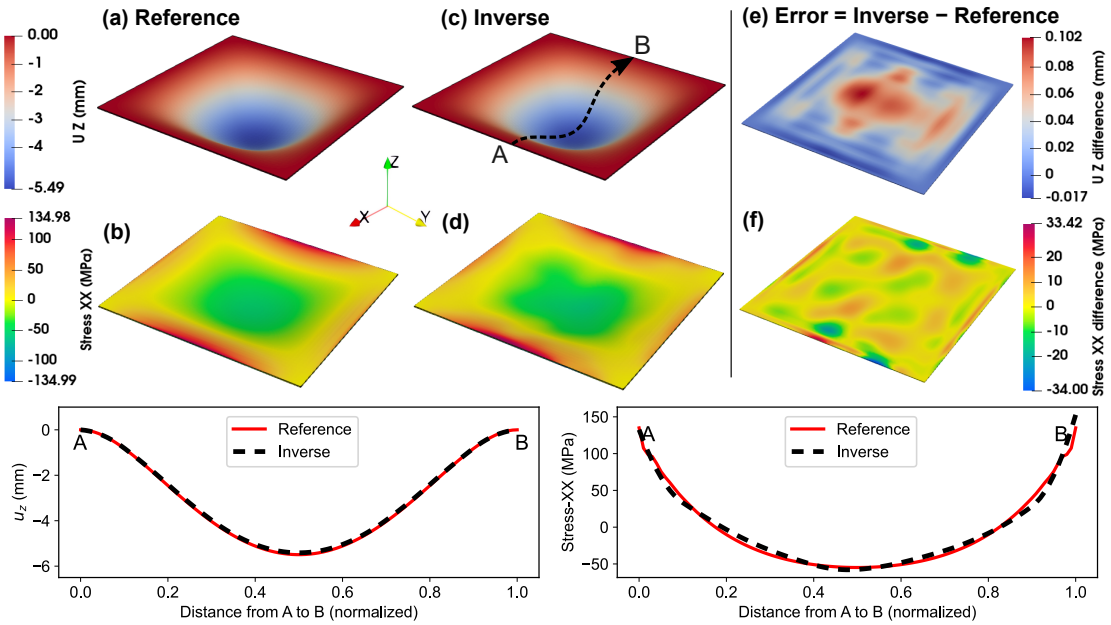

Figure 4.6: Solutions of the plate bending problem: (a, b) Displacement and stress fields of reference solution, (c, d) Displacement and stress fields of inverse solution, (e, f) Error distributions for displacement and stress of the inverse solution. The bottom plots compare the cross-sectional profile and x-component stress along the section A-B in Fig.(c).

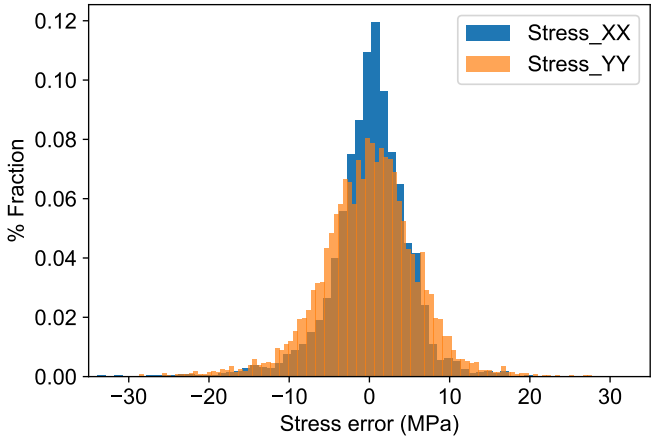

Figure 4.7: Distribution of stress-XX and stress-YY errors for the plate bending problem.

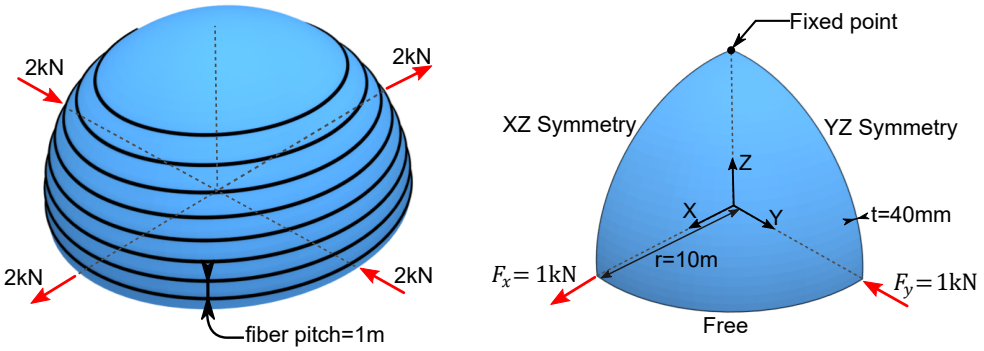

Figure 4.8: Geometry and boundary conditions of the pinched hemisphere problem. The hemisphere is clamped (fixed) at the bottom and a uniformly distributed pressure of 10kPa is applied to the top surface. The fiber layout is the same as in Fig. 4.1.

The DFOS fiber is wrapped around the hemisphere in a helical pattern from the bottom to top with a pitch of $1\,\mathrm{m}$. The numerical analysis utilized a quarter model of the hemisphere exploiting the axial symmetry. Although the fiber layout is not perfectly symmetrical, the variation is insignificant compared to the size of the model. For both forward and inverse models, a mesh size of $500\,\mathrm{mm}$ was used with a single mesh through-thickness, resulting in 2208 control points. Three different fiber sampling intervals were used for the inverse analysis to investigate the variability: $50\,\mathrm{mm}$, $500\,\mathrm{mm}$ and $1000\,\mathrm{mm}$.

The solutions from the forward and inverse IGA for the pinched hemisphere problem are compared in Fig. 4.9. The rendering of the inverse solution in the figure were computed with the sampling interval of $500\,\mathrm{mm}$ whereas the line plots compare the different sampling intervals. As expected, $50\,\mathrm{mm}$ resolution has the highest accuracy closely followed by $500\,\mathrm{mm}$ and least accurate being $1000\,\mathrm{mm}$. It is evident that using a very coarse sampling interval leads to an underestimation of displacements, particularly in the vicinity of loaded points. This outcome is not surprising since the minimum strain energy constraint will favor less deformation when measurement data is too sparse. This phenomena is also consistent with that of existing iFEM elements, which predicted smaller displacements with coarse mesh and measured strains [71]. Hence, it is important to investigate the effect of sampling interval and expected deformation magnitudes for a given structure and fiber configuration to estimate the upper bound of errors.

4.3.4 Pinched cylinder

The final validation model is a slender cylinder subjected to two concentrated loads, as depicted in Fig. 4.10. The cylinder has a length of $600\,\mathrm{mm}$, a radius of $300\,\mathrm{mm}$, and

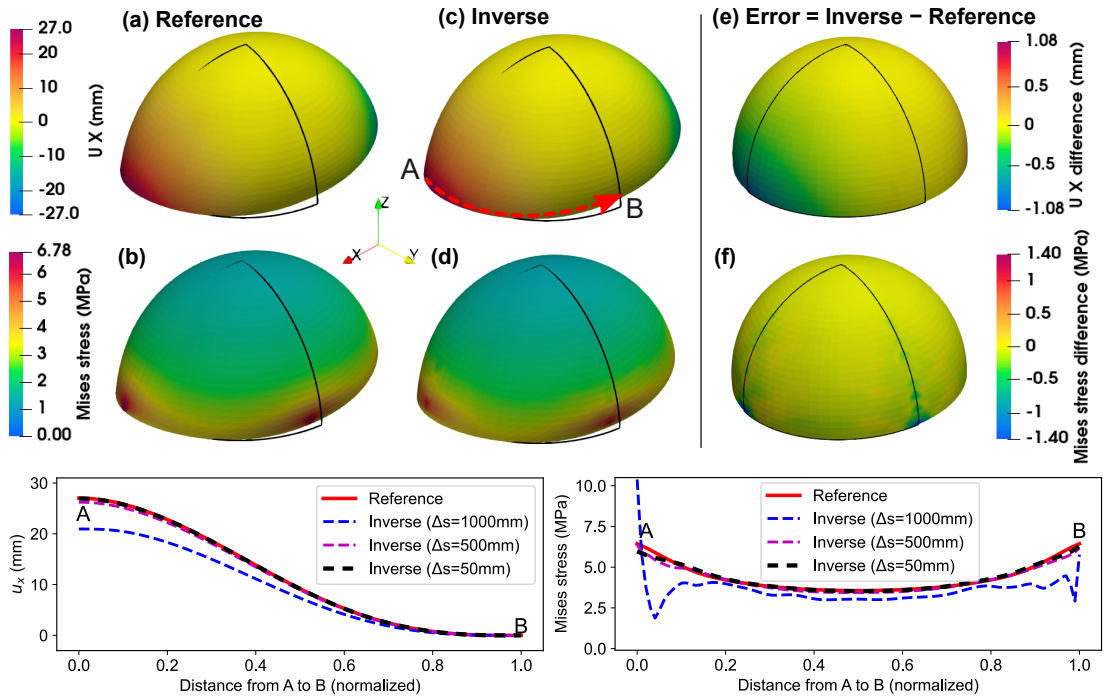

Figure 4.9: Solutions of the pinched hemisphere problem: (a, b) Displacement and stress fields of reference solution, (c, d) Displacement and stress fields of inverse solution, (e, f) Error distributions for displacement and stress of the inverse solution. The bottom plots compare the X-displacement and Mises stress along the line A-B in Fig.(c) under various sampling intervals.

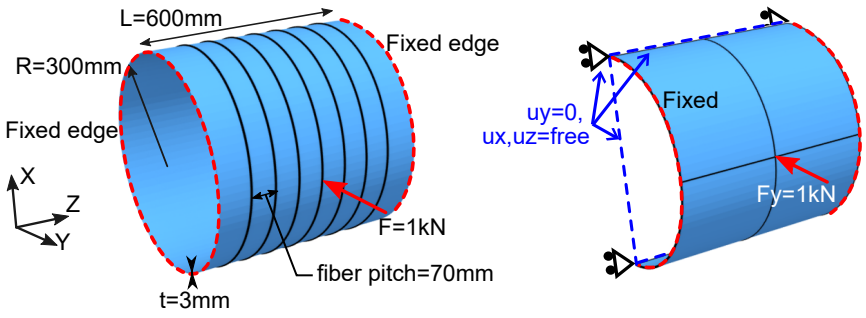

Figure 4.10: (left) Pinched cylindrical pipe with optical fiber, (right) symmetrical model with C0 lines; concentrated load is applied at the mid-span and the symmetric boundary conditions are applied at XZ-plane (dotted blue line)

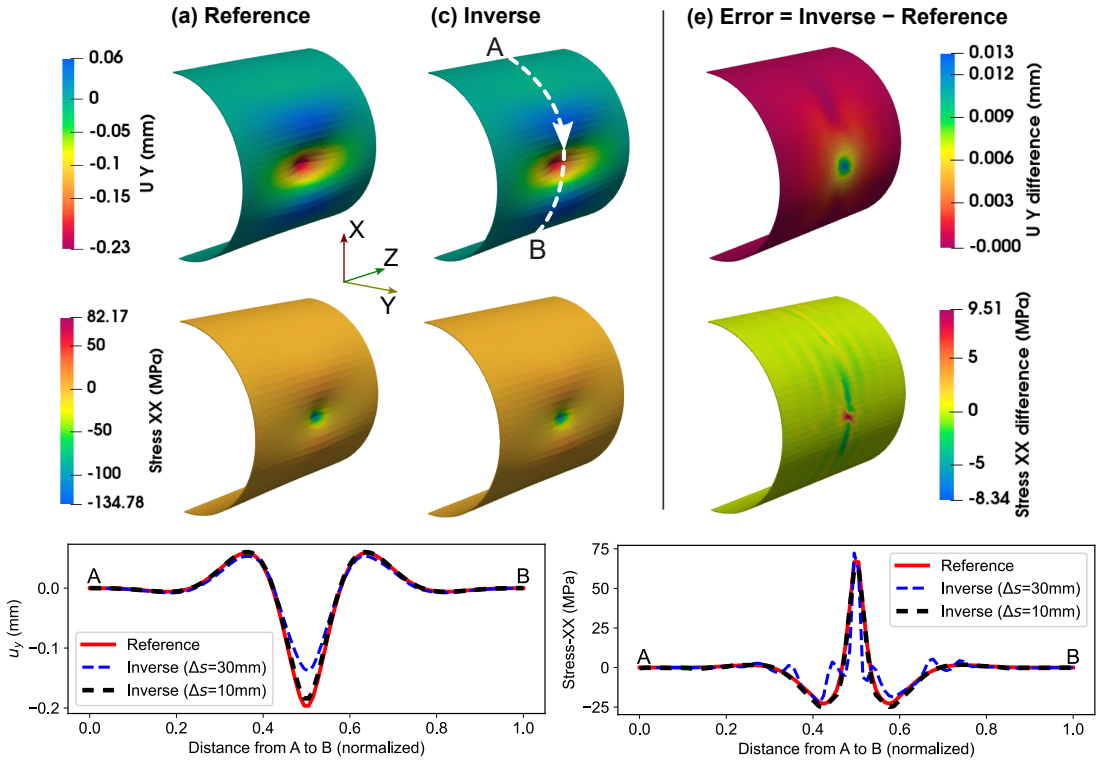

Figure 4.11: Solutions of the pinched cylinder problem: (a, b) Displacement and stress fields of reference solution, (c, d) Displacement and stress fields of inverse solution, (e, f) Error distributions for displacement and stress of the inverse solution. The bottom plots compare the Y-displacement and X-stress along the line A-B in Fig.(c) under various sampling intervals.

thickness of $3\,\mathrm{mm}$. It is supported by rigid diaphragms at both ends and point loads of $1\,\mathrm{kN}$ are applied on the opposite sides of the cylinder, resulting in a highly localized deformation near the point loads. The DFOS fiber is wrapped on the outer and inner surfaces of the pipe with a pitch of $70\,\mathrm{mm}$. A half symmetrical model was used in the analysis. A C^0 line was added at the mid-span via knot multiplicity to enforce the lengthwise symmetry. The cylinder's geometry is second-order throughout and the mesh size is $20\,\mathrm{mm}$, with no subdivision in the thickness direction.

The displacement and stress contours for the reference and inverse solutions using a fiber strain sampling interval of $10\,\mathrm{mm}$ are shown in Fig. 4.11. Another inverse analysis with a larger $30\,\mathrm{mm}$ sampling interval was also performed and the results along the section A-B are compared in the line plots. The inverse solution is nearly identical to the reference solution except in the vicinity of the point load. The concentrated load caused highly localized strains that were difficult to capture even with centimeter resolution. It is noteworthy that this loading condition is an extreme scenario that is unlikely to occur

in real-life situations. Nonetheless, the inverse solution exhibits good accuracy even in unfavorable conditions. Furthermore, these findings demonstrate that the distributed nature of DFOS sampling allows for the detection of local deformations with reasonable accuracy in any location as long as the spatial resolution is sufficient relative to the size of deformation zone.

4.4 Sensitivity analysis

The inverse solutions in the previous section show excellent accuracy but they do not take into account the possible measurement noise. In other words, the input fiber strains were directly fed from the reference solution. In reality, DFOS measurements have a noise floor which depends on the instrument setup, sampling interval, averaging count and the environment. Hence, a study of the robustness of the inverse predictions with respect to measurement noise is necessary. This can be done by adding simulated white noise to the input fiber strains. For each fiber strain data, the noise is randomly sampled from a normal distribution with mean 0 and variance σ^2:

$$\varepsilon_f^* = \varepsilon_f + \mathcal{N}(0, \sigma^2) \tag{4.13}$$

where ε_f is the computed fiber strain using forward IGA. Zero mean indicates there is no systemic bias and variance represents the magnitude of noise.

DFOS sensing has the advantage of being able to adjust spatial resolution to optimize measurement time and accuracy. A large number of sampling points can increase readout time and hence may not be suitable for monitoring dynamic responses. On the other hand, fine sampling provides more information about local strain variation but increases measurement noise due to shorter averaging span. This is further complicated by the fact that changing the sampling interval generally alters the location of sampling points. Common sense tells us that the more data points we have, the more accurate the solution will be. However, a quantitative analysis is needed to determine the optimal sampling interval for a given structure and fiber configuration.

The following is the study of sensitivity on the sampling interval and measurement noise for the four numerical examples in the previous section, namely plate twisting, plate bending, pinched hemisphere and pinched cylinder. The quantitative errors for the reproduced fiber strains and displacement distributions can be evaluated by the root mean square error (RMSE) between the reference and inverse solutions. The RMSE and

Model	Δs	e_f^{RMS} ($\mu\varepsilon$)	e_f^r	e_u^{RMS} (mm)	e_u^r
Plate twisting	$50\,\mathrm{mm}$	4.349×10^{-8}	3.327×10^{-4}	8.091×10^{-5}	4.045×10^{-3}
Plate bending	$20\,\mathrm{mm}$	1.493×10^{-6}	6.792×10^{-3}	3.926×10^{-5}	7.146×10^{-3}
Pinched hemisphere	$50\,\mathrm{mm}$	5.900×10^{-9}	2.664×10^{-4}	8.798×10^{-5}	3.261×10^{-3}
Pinched cylinder	$10\,\mathrm{mm}$	1.567×10^{-8}	1.758×10^{-5}	3.922×10^{-6}	8.610×10^{-3}

Table 4.1: Error matrices for the numerical examples with pure fiber strain inputs

relative RMSE of the fiber strains are defined as

$$e_f^{\text{RMS}} = \sqrt{\frac{1}{n_s}\sum_{i=1}^{n_s}\left(\varepsilon_{fi}^* - \varepsilon_{fi}\right)^2},\ e_f^r = \frac{e_f^{\text{RMS}}}{\max|\boldsymbol{\varepsilon}_{fi}^*|}. \tag{4.14}$$

Similarly, the RMSE and relative RMSE of the displacement distributions can be as

$$e_u^{\text{RMS}} = \left[\frac{1}{\Omega}\int_\Omega (\boldsymbol{u}^* - \boldsymbol{u})^T(\boldsymbol{u}^* - \boldsymbol{u})\,\mathrm{d}\Omega\right]^{\frac{1}{2}},\ e_u^r = \frac{e_u^{\text{RMS}}}{\max|\boldsymbol{u}^*|}, \tag{4.15}$$

where $\boldsymbol{u}^*$ and $\boldsymbol{u}$ refer to the reference and inverse displacement fields respectively. Table 4.1 shows the quantitative errors for the previous analyses (without added noise).

4.4.1 Sensitivity to sampling interval

Figure 4.12 shows the relative displacement errors with respect to the sampling intervals for the validation models. Figure 4.12(a) shows the results for the plate twisting problem from $10\,\mathrm{mm}$ to $150\,\mathrm{mm}$. At sampling intervals greater than $120\,\mathrm{mm}$, the relative displacement errors fluctuate between $3\,\%$ to $6\,\%$. This behavior shows that the accuracy of the inverse solution cannot be readily predicted for sparse data points. This can be explained by fiber strain sampling points having different weights on the accuracy. The sampling points which are closely aligned with principal strain directions at the measurement site contribute more information to the system and hence are more critical in terms of sensing sensitivity. For example, if the fiber tangent direction is perpendicular to the principal strain direction at a sampling point, the principal strain component cannot be measured. On the other hand, if the fiber is parallel to that component, it can fully determine the principal strain (see Section 3.2.3). Therefore, the position and direction of measurement points are critical for sparse sampling conditions. The sampling interval not only affects the position of the sampling points but also changes the strain projection direction, and it has a more significant impact on accuracy at coarse spatial resolutions. At finer sampling intervals ($< 100\,\mathrm{mm}$), influence of ineffective data points decreases and the inverse solution converges to the reference solution.

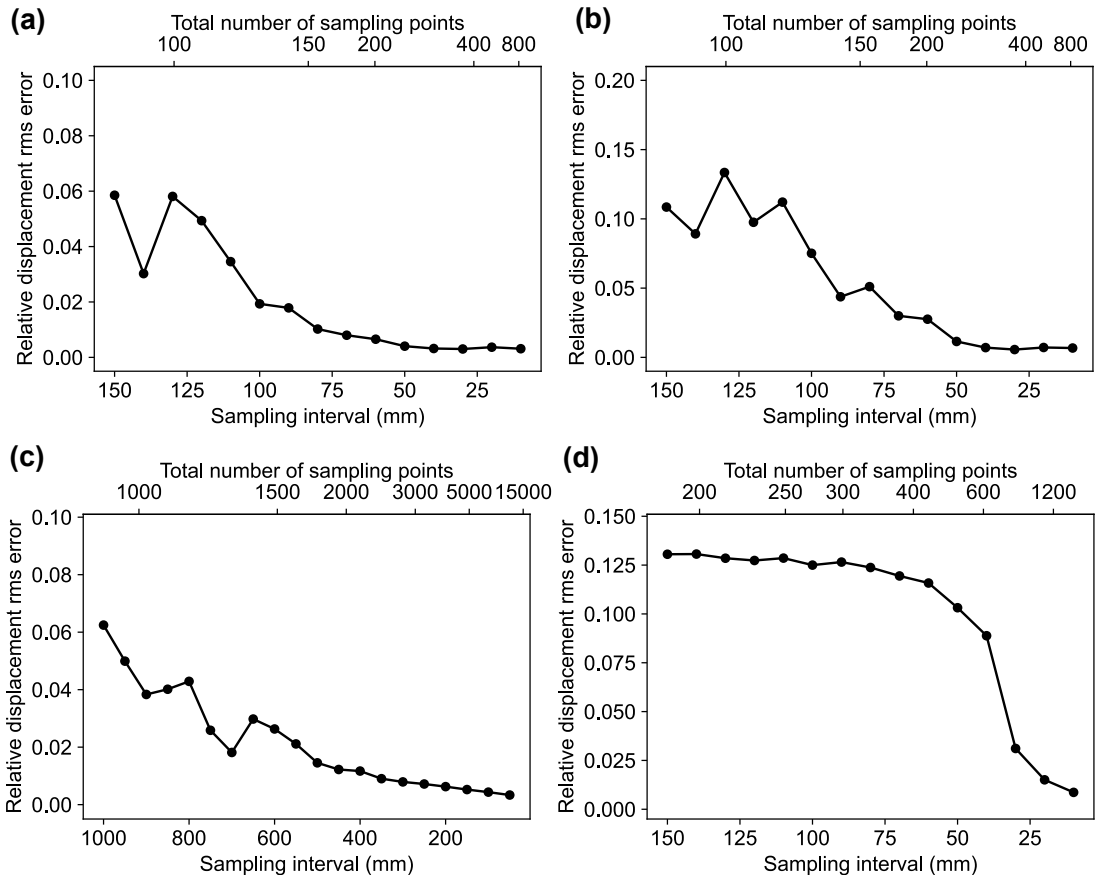

Figure 4.12: Relative RMS displacement errors with respect to sampling interval for (a) plate twisting, (b) plate bending, (c) pinched hemisphere and (d) pinched cylinder problems

The same can be observed for the bending problem in Fig. 4.12(b) and pinched hemisphere problem in Fig. 4.12(c). For the pinched cylinder problem however, the error trend tells a different story. The errors are relatively high for all intervals greater than $30\,\mathrm{mm}$ and then rapidly drops near zero. This is because the model has a highly localized deformation and strain concentration near the point load (Fig. 4.11). The radius of the local deformation zone is about $50\,\mathrm{mm}$ which matches the critical point in the error plot. It is reasonable that large sampling intervals cannot capture the local strain concentration. Although this scenario is unlikely to occur in real word, it shows that caution should be exercised when choosing the sampling interval.

4.4.2 Sensitivity to noise

State-of-the-art DFOS interrogators have typical uncertainty around $5\,\mu\varepsilon$ to $20\,\mu\varepsilon$ depending on the measurement parameters [51]. Hence, variance from $5\,\mu\varepsilon$ to $20\,\mu\varepsilon$ at $5\,\mu\varepsilon$ steps were used for the simulated noise magnitude while keeping a constant sampling interval. Since the noise added to each sampling point is stochastic, inverse simulations were repeated $500\,\mathrm{times}$ for each noise value to obtain the error distribution.

The error distributions for each noise level are summarized in box plots in Fig. 4.13. In all cases, mean displacement errors increase linearly with respect to the noise magnitudes. The variance of errors also increases as noise increases. Since the sampling interval was fixed, the wider spread of displacement errors supports the previous claim that certain sampling points have a greater impact on solution accuracy. The plots also have different error scales on the Y-axis which is the result of different signal-to-noise ratio in each problem.

4.5 Application of inverse IGA-DFOS to an impeller plate

In this section, the inverse IGA-DFOS is applied to predict the deformation of a flat-plate impeller blade under rotation. The impeller is a device used to mix fluids in a vessel for homogeneity. In addition to monitoring mechanical response of the impeller, changes in fluid viscosity can be inferred from the deformation of the impeller. In this study, a flat plate impeller will be used as a lab model to facilitate simple installation of optical fibers.

4.5.1 Experimental setup

The experiment setup of the mixer and impeller is shown in Fig. 4.14. The impeller plate is $2.5\,\mathrm{mm}$ thick and made of stainless steel SUS304. The CAD drawing of the impeller plate is shown in Fig. 4.15.

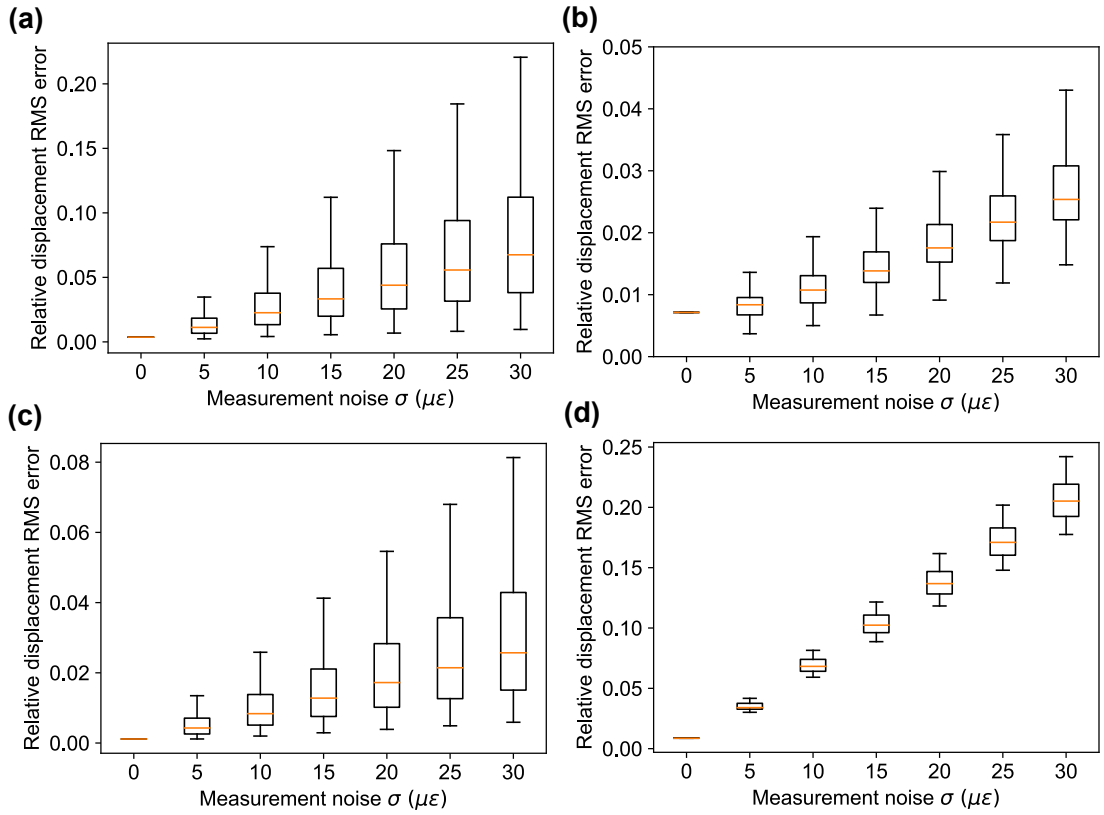

Figure 4.13: Relative RMS displacement errors with respect to noise level and total number of samples (a) plate twisting problem, (b) plate bending problem, (c) pinched hemisphere problem and (d) pinched cylinder problem

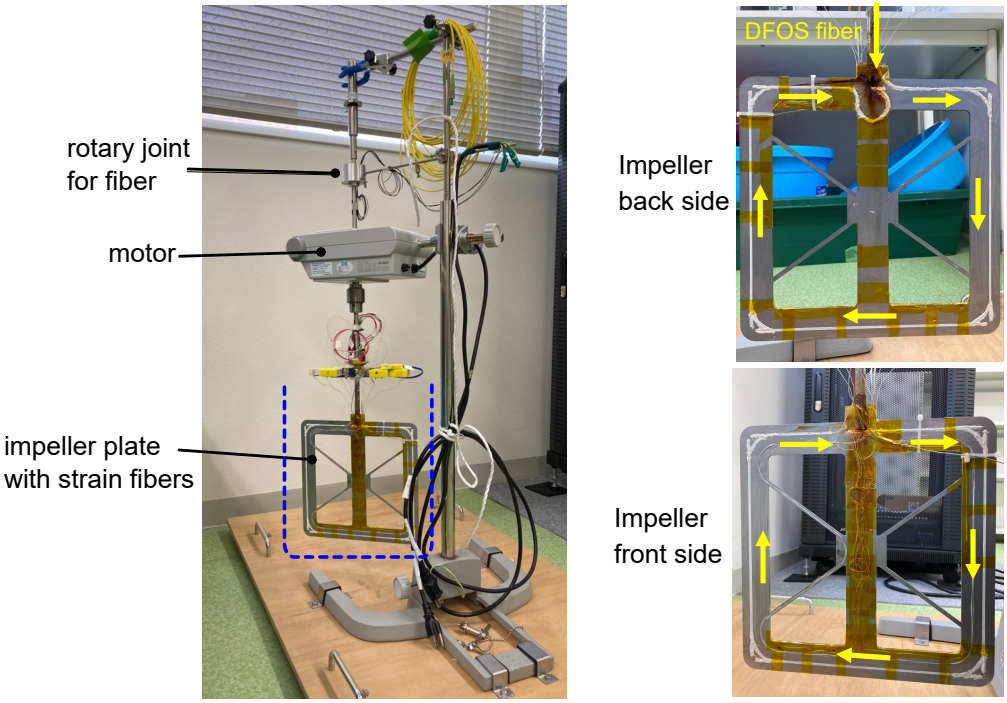

Figure 4.14: Experimental setup of the mixer. The DFOS fiber (under white protective coating) is attached to the front and back sides of the impeller plate. The yellow arrows show the direction of the fiber from the instrument. The dotted blue line is a placeholder for the vessel which holds the fluid.

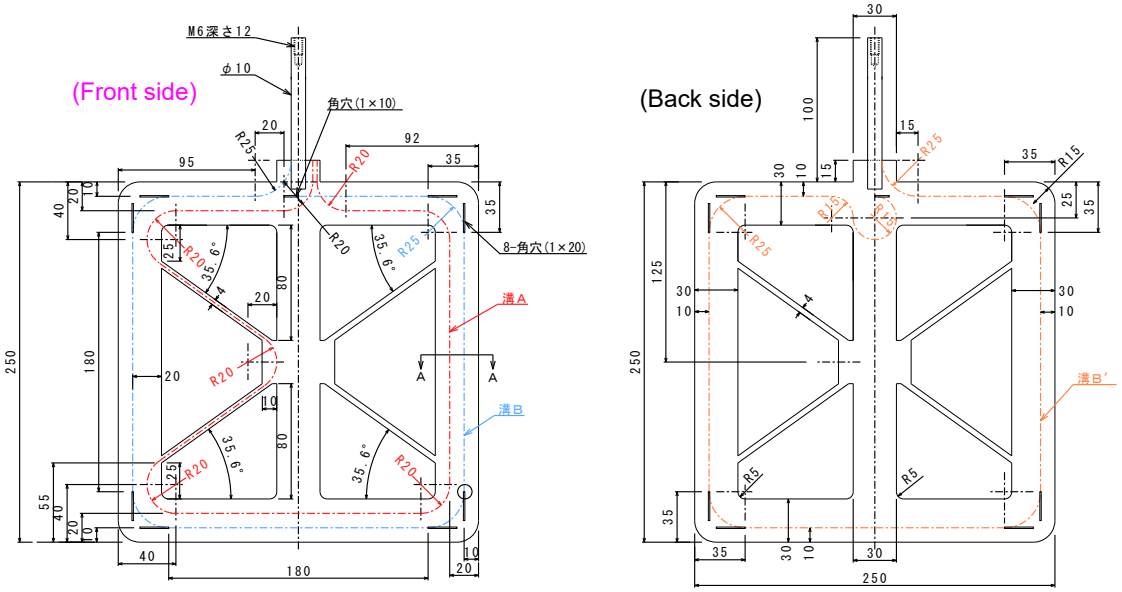

Figure 4.15: Dimensions of the impeller plate. Blue and orange lines show the trace for strain fiber, red line shows the trace for temperature fiber.

The DFOS optical fiber is attached to the front and back sides of the impeller plate with glue which also protects the fiber from the fluid. When the plate rotates with $40\,\mathrm{RPM}$ to $60\,\mathrm{RPM}$, the resistance of the fluid causes the plate to deform. This deformation induces surface strains and fiber strains which are measured by the DFOS instrument.

The fluid used in the experiment was Carboxymethyl cellulose (CMC) solution with viscosity ranging from $5800\,\mathrm{mPa\,s}$ to $10\,000\,\mathrm{mPa\,s}$. The vessel was heated with electric furnace to simulate the industrial mixing process. The temperature of the fluid was measured using thermocouples. Before the experiment, the mixer was run for several hours to distribute the heat and allow the fluid to become homogeneous. After the initial run, the rotation was stopped to take the reference strain readings. Then, the impeller was rotated and the DFOS measurements were taken at 40, 60 and 80 motor RPMs. Each measurement was repeated twice while keeping the motor RPM constant. The sampling interval of fiber strains in all cases was $1\,\mathrm{cm}$. The DFOS instrument gives raw readings in term of frequency shift in GHz which can be converted to strain change after temperature compensation.

4.5.2 Experimental Results

Figure 4.16 shows the fiber strains for two trials using viscosity $5800\,\mathrm{mPa\,s}$ and $60\,\mathrm{RPM}$ at $30\,^{\circ}\mathrm{C}$. The fiber strains on the impeller's front and back sides show similar trends. In order to better understand the fiber strains corresponding to physical locations on the impeller, the fiber strains are visualized on the actual fiber geometry in Fig. 4.17. Since the direction of fiber is opposite on the front and back side of the plate, the fiber coordinates are flipped and superimposed on their relative distances. From this figure, the following observations can be made:

- The magnitude of fiber strains are largest near the centerline of the plate and decreases towards the edges.
- On the top part of plate, fiber strains are tensile on one side and compressive on the other side of the centerline.
- The front-side and back-side fiber strains are mirror image of each other as evident from the line plot.
- The fiber strains on the top part of the plate are larger than those on the bottom part.

These observations can be easily explained by the bending deformation of the plate due to rotation. Bending induces tensile and compressive strains on the opposite sur-

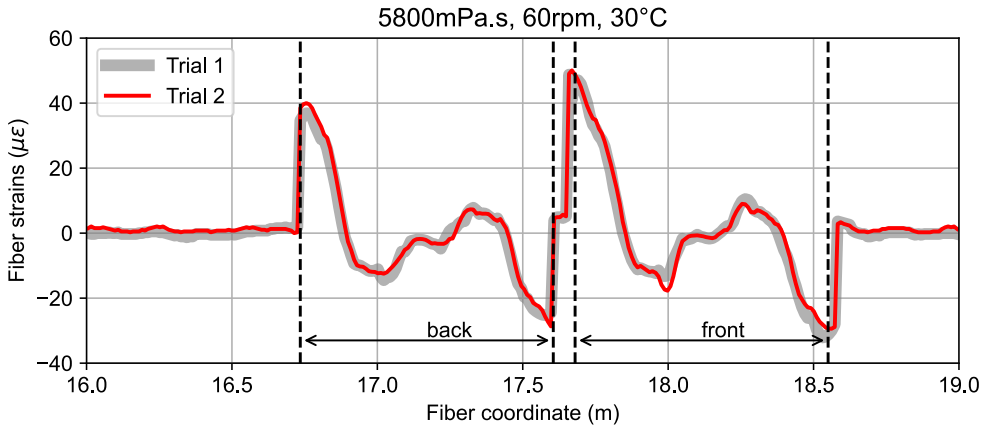

Figure 4.16: Fiber strain difference for the first case with viscosity $5800\,\mathrm{mPa\,s}$ at $60\,\mathrm{RPM}$. The vertical dotted lines mark the portion of fiber corresponding to the front and back sides of the plate.

faces through thickness with equal magnitude (assuming the middle neutral axis). Since the plate is free on the bottom edge, bending strain is highest near the top center where it is attached to the shaft and weaker at the bottom.

4.5.3 Inverse IGA Model

The geometry of the impeller plate is too complex to be modelled with a single patch NURBS structure. Hence, eight second order solid patches are individually modelled as shown in Fig. 4.18. The patches are coupled at their shared interfaces using Nitsche penalty method described in Section 2.6. The plate is fixed at the top-center joint as essential boundary conditions. The fiber curves for front and back side are also modelled with second order geometries after the experiment design.

The coupled impeller plate geometry is then subdivided using h-refinement to create the IGA mesh with $5\,\mathrm{mm}$ mesh size. Since the inverse analysis is linear static and purely mechanical, interaction between the impeller and fluid is assumed to be steady state. The temperature effects on the impeller plate are ignored in this study since the fiber strain measurements were obtained near room temperature. The Young's modulus of the plate is $200\,\mathrm{GPa}$ and Poisson's ratio is 0.3.

4.5.4 Results and Discussion

Figure 4.19 shows the contours of predicted deformation from the inverse analysis for different RPMs under constant viscosity. A key observation is that the deformation is smooth everywhere although the fiber is only a single line near the edge (Fig. 4.15).

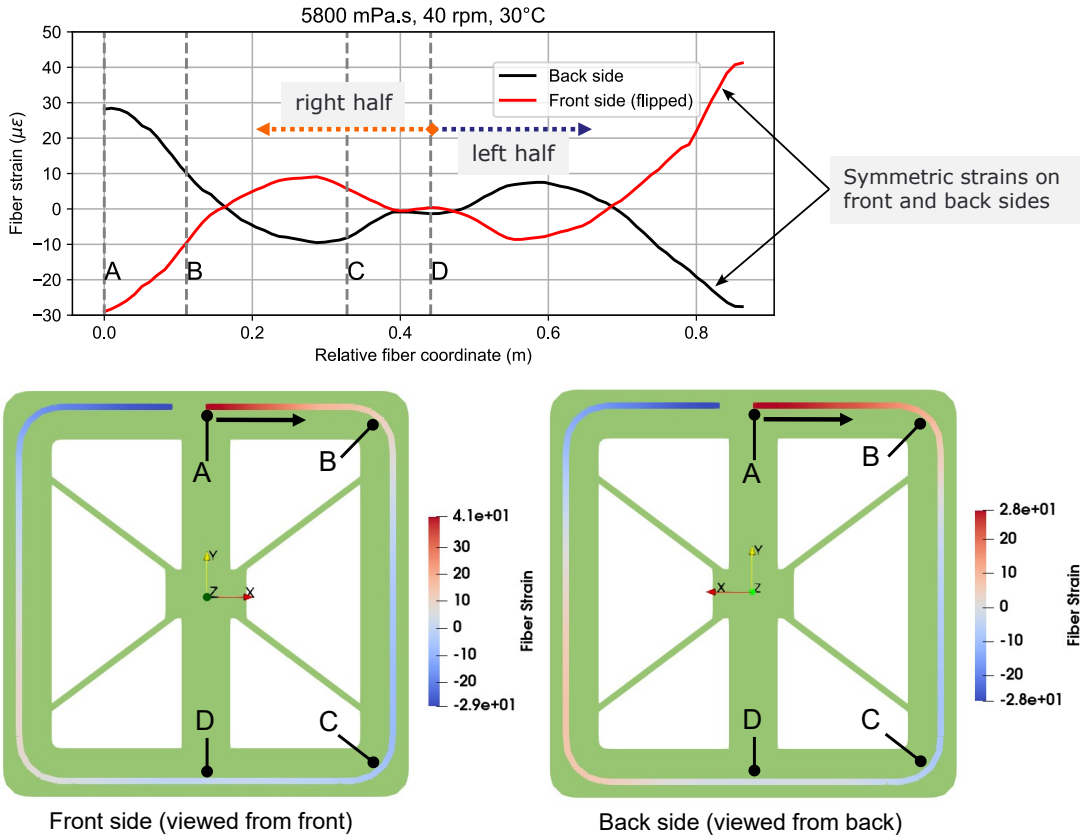

Figure 4.17: Fiber strains at the same positions on the front and back sides of the plate are plotted on the same axis to enable comparison.

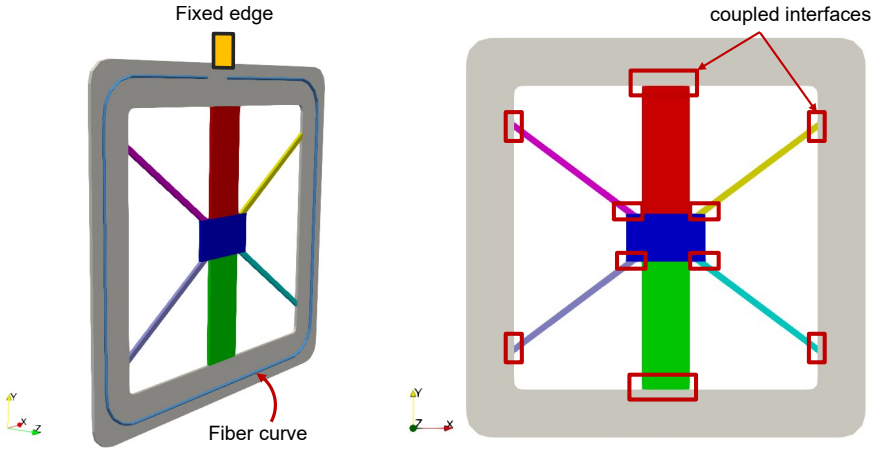

Figure 4.18: CAD model of the impeller plate and fiber geometry. The NURBS patches are color-coded. Shared surfaces are shown in red rectangles.

It shows that the inverse algorithm can infer the unknown displacement DOFs even for the patches with no fiber strain measurements by solving the global least-squares problem. Quantitatively, the inverse model has 4434 control points and 170 total fiber strain measurement points, making known/unknown ratio to be 26. The figure clearly shows the bending deformation mode of the plate and the anti-symmetry on the vertical axis. The shape is the outcome of rotation under fluid resistance. It can be seen that the bending is prominent at the top edge of the plate where it receives torque from the motor shaft. In contrast, the bottom side shows little bending but rigid rotation about the center axis. This is also reasonable since the bottom edge is free and the fiber strains along the bottom are much smaller than those at the top edge (Fig. 4.17) which indicates the bending is much less. As expected, the displacement magnitudes increase monotonically with RPM while the overall shape stayed similar. Interestingly, the magnitude of bending is not linearly proportional to the RPM as can be seen from the displacement magnitudes in Fig. 4.19.

Figure 4.20 compares the measured fiber strains from the experiment and reproduced fiber strains from the inverse analysis for the case with viscosity $5800\,\mathrm{mPa\,s}$ and $40\,\mathrm{RPM}$. The reproduced fiber strains show very good agreement with the experimental data with the average deviation less than $1\,\mu\varepsilon$. It shows that the inverse analysis can be efficiently performed with NURBS model and measured fiber strains with minimal human intervention.

Figure 4.21 shows the horizontal stress contours from the inverse analysis for the case with viscosity $5800\,\mathrm{mPa\,s}$ and $40\,\mathrm{RPM}$. Similarly to displacements, the bending stresses are anti-symmetric along the centerline with the highest magnitudes ($\approx$$10\,\mathrm{MPa}$) near the fixed edge. The upper two arms experience the highest stress since they transfer the torque to the side faces. The four webs connected to the primary frame also experience relative low stresses ($1\,\mathrm{MPa}$ to $2\,\mathrm{MPa}$) except at the joints where stress concentrations occur. The stress color contour shows some irregularities around the corners of the frame where spurious local stress concentrations can be seen. They are most likely numerical anomalies due to the absence of reliable fiber strain measurements in these regions since the fiber direction is rapidly changing in a small length. These anomalies should disappear as the model size gets larger than the fiber length scale.

In this experiment, the inverse analysis was used to calculated the structural response of the impeller plate from the fiber strain measurements. From the outcomes, one can envision a monitoring system which not only gives insight during the operation but also provides feedback for the future design. Structural state such as deformation, stress distribution and stress concentrations can be tracked near real-time since the computational cost of the inverse analysis is quite low after solving the initial prob-

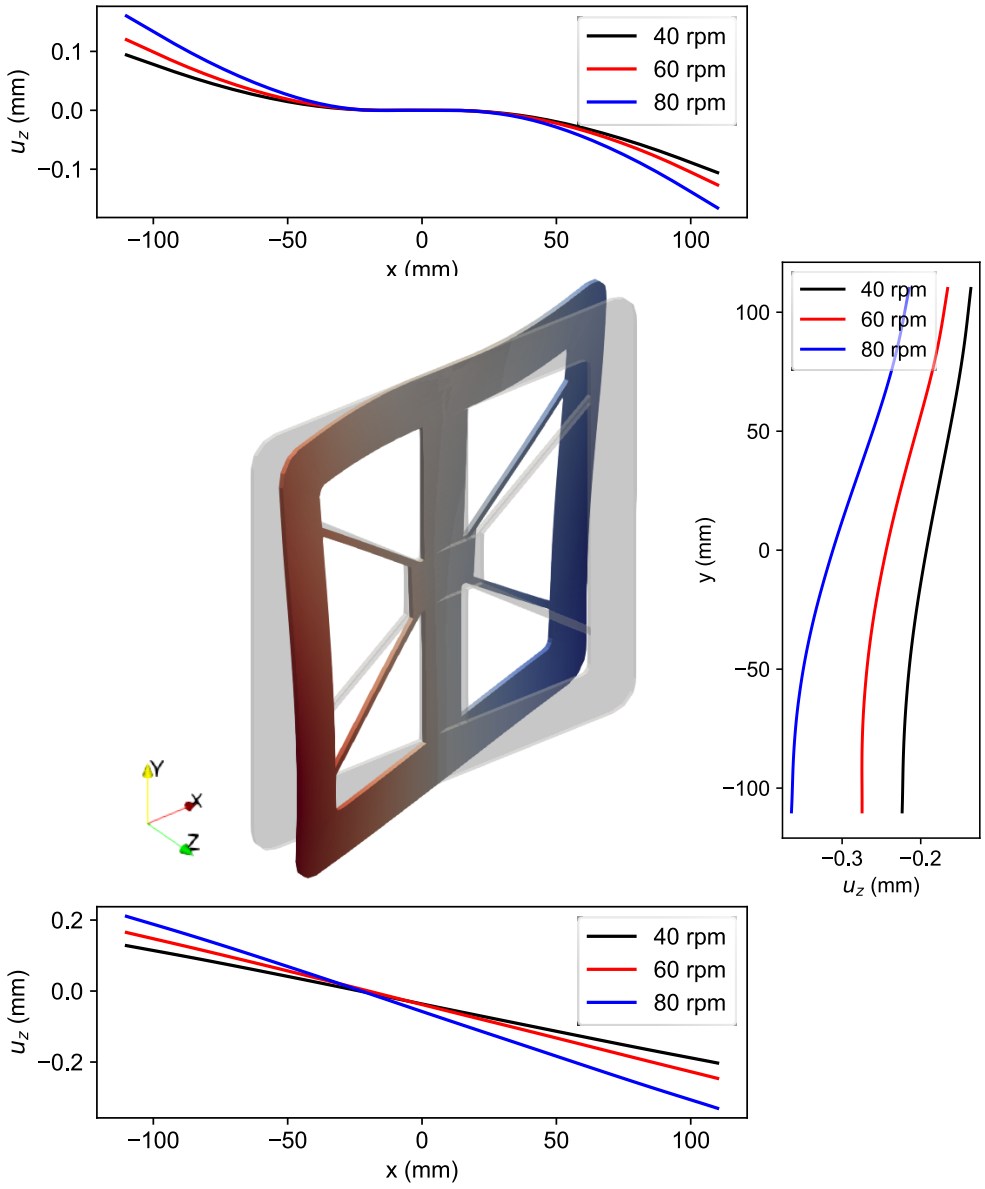

Figure 4.19: Deformation profiles from the inverse IGA-DFOS for variable RPMs (viscosity = $5800\,\mathrm{mPa\,s}$). The middle figure shows the shape of deformation ($\times 200$ times) in 3D under $80\,\mathrm{rpm}$. The line plots show the displacements of top, side and bottom edges.

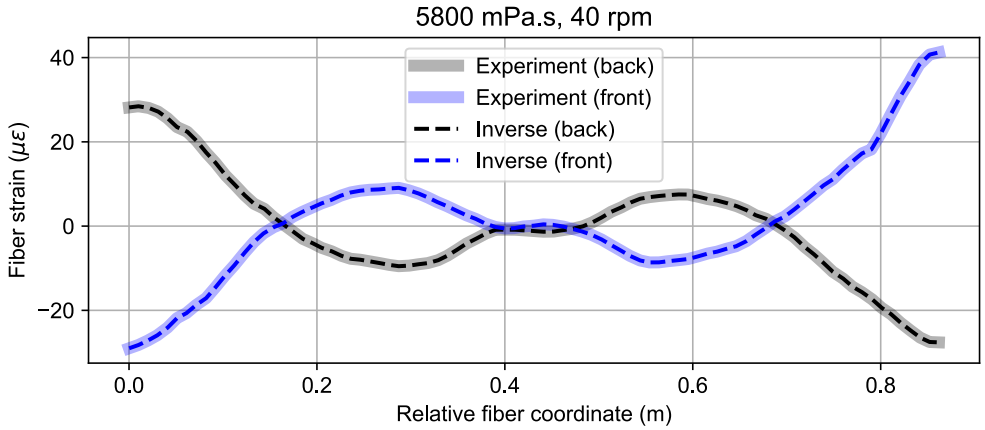

Figure 4.20: Experimental and reproduced fiber strains from inverse analysis for viscosity $5800\,\mathrm{mPa\,s}$ and $40\,\mathrm{RPM}$.

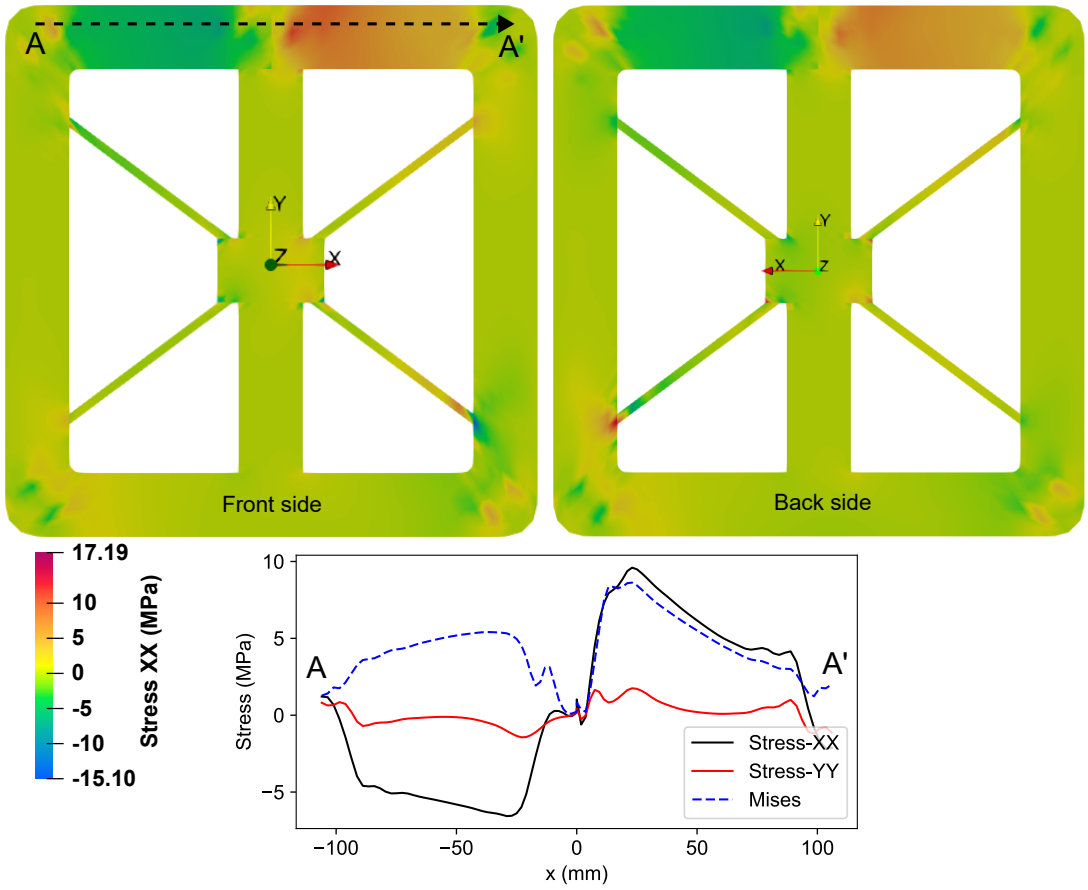

Figure 4.21: X-Stress contours from the inverse IGA-DFOS for viscosity $5800\,\mathrm{mPa\,s}$ and $40\,\mathrm{RPM}$.

lem. Moreover, operational loads (such as fluid viscosity in the current problem) can be indirectly calculated from the mechanical response of the structure. In addition, the remaining fatigue life of the structure can be predicted by continuous monitoring of the stress history. The information from the inverse analysis of the current design can also be used to optimize the design of the next generation of the structure. Hence, the design process is no longer open-ended but utilizes real world data. The connection of IGA with CAD is beneficial for the iterative design since modifications to the CAD model can be easily incorporated into the IGA model.

4.6 Summary

In this chapter, a novel inverse analysis method was developed using IGA and DFOS for linear elastic problems. The integrated fiber model was applied to derive an efficient single-step method for the reconstruction of displacement, strain and stress fields from fiber strain measurements. The methodology used a least-squares variational formulation to add a penalty term which supplements the total potential energy of the system. The constraint conditions were derived by solving the least-squares functional which resulted in a coupled system of equations.

The method was verified using four numerical examples of plate, hemisphere and cylinder geometries with different deformation modes and loading conditions. The results show that the inverse IGA-DFOS can accurately reproduce the displacement field and fiber strains with high accuracy. In addition, sensitivity analysis was performed to investigate the effect of DFOS sampling interval and measurement noise on the accuracy of the inverse solution. While the optimal sampling interval depends on the structure and fiber configuration, the results indicate that the inverse IGA-DFOS is robust to measurement noise and maintains a reasonable accuracy without human intervention. Combined with the modelling benefits of IGA and flexibility of DFOS, this illustrates the potential of the inverse IGA-DFOS method for real-world applications.

In the last part, the method was applied to predict the deformation of an impeller plate under rotation. The inverse IGA-DFOS was able to accurately reproduce the measured fiber strains and predict the deformation of the impeller plate. The deformation is smooth and matches the expected bending mode even though the input data is sparse. The stress distribution shows that there are several stress concentrations under loading in the current design. There are a few anomalies in the stress results due to difficulty in measuring local strains in small length scales. Overall, the results show that the inverse IGA-DFOS can be used to monitor the structural response of the impeller plate and provide information for the future design. Although temperature effects were not

considered in the current study, it may be advantageous to integrate the temperature dependency of the fiber in the model.

The creation of NURBS model for the complex geometries such as the impeller plate in the study is rather difficult and hence could be improved by using more advanced techniques such as T-spline or trimmed surfaces [74]. While the current formulation is for linear elasticity, it can be extended to nonlinear problems by successive linearization. Further investigations on the systemic estimation of errors and optimal fiber layout are also recommended. Other research directions include hybrid inverse analysis by incorporating known information such as sensor fusion to improve accuracy.

Chapter 5

Extension of IGA for Nonlinear Material Models

5.1 Introduction

The material model is a crucial part of elastoplastic simulation especially for large deformation problems. In this chapter, the mechanical behavior of a high strength steel after it has been subjected to plastic strain is experimentally investigated and observed behavior is modelled using an empirical model.

5.2 Mechanical properties of the raw material

The nominal material properties of JSC980YL dual phase high strength cold-rolled steel are listed in Table 5.1 [75]. The uniaxial tensile tests of the raw material specimen were conducted in two directions: the rolling direction (L) and the transverse direction (C). All specimens were cut from $1.6\,\mathrm{mm}$ thick steel sheet and the tensile test specimens had a gauge section of $10\,\mathrm{mm} \times 20\,\mathrm{mm}$. Additionally, an in-plane shear test was performed with the ASTM B831-14 specimen shown in Fig. 5.1. The results from these three tests were utilized to calculate the stress ratio coefficients with respect to L direction. These tests determine the degree of initial anisotropy in the stock material.

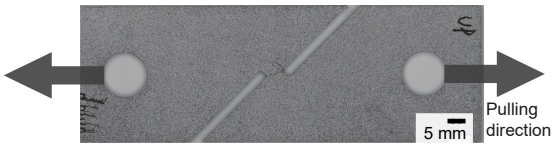

Figure 5.1: Shear test specimen

Quantity	Value	Unit
Yield stress	681	MPa
Tensile strength	1045	MPa
Elongation	14	%
Young's modulus	210	GPa
Poisson's ratio	0.3	

Table 5.1: Mechanical properties of JSC980YL steel

The stress-strain curves from uniaxial tensile tests of the raw material are shown in Fig. 5.3. There is a $2\,\%$ offset between L and C directions. Shear stress is calculated as $F/(bt)$ where F is the measured force and bt is the sectional area. Shear strains on the gauge section were measured using a digital image correlation (DIC) system. Assuming pure shear, equivalent stress and equivalent plastic strain is:

$$\bar{\sigma} = \frac{\sqrt{3}}{R_{xy}}\tau_{xy},\ d\bar{\varepsilon}_p = \frac{2}{\sqrt{3}}R_{xy}d\varepsilon^p_{xy}, \tag{5.1}$$

where R_{xy} is the shear strain ratio defined as the ratio of shear strain to axial strain.

Shear stress-shear strain and equivalent stress-strain curves from the shear test are shown in Fig. 5.2. It can be seen that $R_{xy} = 1.01$ gives a good agreement with the equivalent stress-strain curve measured in the rolling direction. The stress ratios and Swift parameters of the reference Raw L curve are shown in Table 5.2.

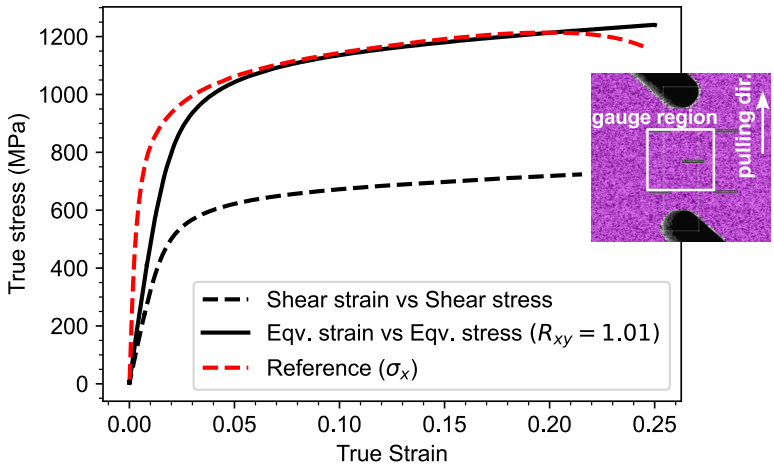

Figure 5.2: Shear stress-strain and corresponding equivalent stress-strain curves

σ^y_{xx} (MPa)	K (MPa)	ε_0	n	$R^0_{xx} = \frac{\sigma^y_{xx}}{\sigma_0}$	$R^0_{yy} = \frac{\sigma^y_{yy}}{\sigma_0}$	$R^0_{xy} = \sqrt{3}\frac{\tau^y_{xy}}{\sigma_0}$
663	1447	2.74×10^{-4}	0.102	1.00	1.02	1.01

Table 5.2: Initial yield stress and Swift parameters of the reference (Raw L) hardening curve, and initial yield stress ratios relative to the reference

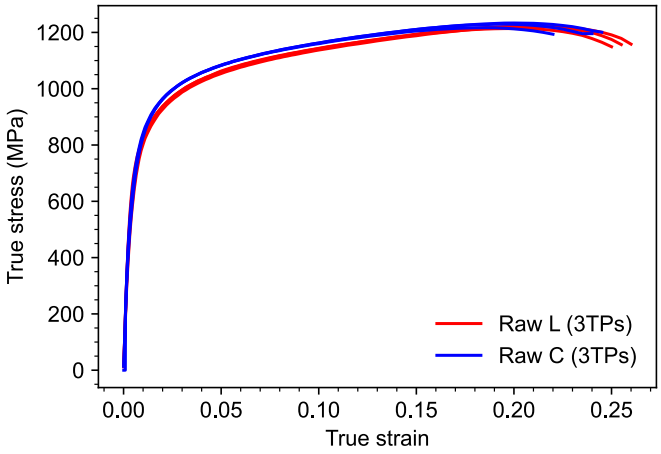

Figure 5.3: Uniaxial stress-strain curves of the raw material in L and C directions (3 test pieces)

5.3 Uniaxial Tensile Tests of Prestrained Specimens

To investigate the effect of prestrain on the mechanical behavior of dual-phase high strength steel DP980, uniaxial tensile tests of prestrained specimens were conducted. The prestrained specimens were prepared by pulling a large tensile test piece and cutting small tensile test pieces after elongation as illustrated in Fig. 5.4. The axial strain during prestraining was monitored with a strain gauge at the middle of the specimen. After a predetermined plastic strain was achieved, the test piece was unloaded and deformations of five inscribed circles on the surface were measured. Then, equivalent plastic (pre)strain was calculated from the average elongation. The direction of prestrain and measured elongations from the experiments are shown in Table 5.3.

Specimen	Elongation (%)					Average	ε_{eq}(logarithmic)
	1	2	3	4	5		
2% plane strain (L)	2.0	2.0	2.0	2.0	2.0	2.0	0.022
5% plane strain (L)	5.2	5.4	5.4	5.2	5.2	5.28	0.059
5% plane strain (C)	4.8	5.2	5.2	5.0	5.4	5.12	0.055

Table 5.3: Measured elongation and equivalent plastic strain values after prestraining

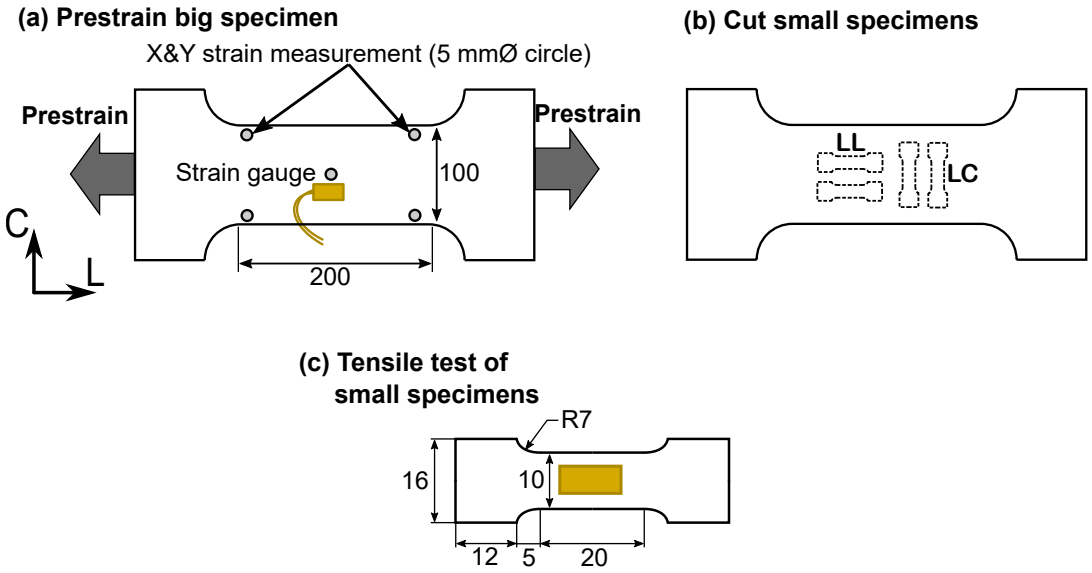

Figure 5.4: Preparation of prestrained specimens for L-prestrain. (a) A big specimen of raw material was pulled. Elongation was measured by the strain gauge at the center and x,y strains were measured using inscribed 5 mm diameter circles. (b) Small test pieces were cut from the large prestrained test piece in L and C directions. (c) Dimensions of small prestrained specimens.

Nominal prestrain elongation	Prestrain direction	Reloading direction	Case designation
2%	L	L	2 LL
2%	L	C	2 LC
5%	L	L	5 LL
5%	L	C	5 LC
5%	C	C	5 CC
5%	C	L	5 CL

Table 5.4: Designation of experiment cases

Since there are four combinations of prestrain and reloading directions, the specimens can be designated according to the prestrain amount, prestrain direction and reloading direction. This resulted in six unique cases as shown in Table 5.4 and each case was repeated twice.

5.3.1 Experiment results

The stress-strain curves from the reloading uniaxial tensile tests of prestrained samples are shown in Fig. 5.5. The following observations can be made from the nonlinear part of the curves:

- yield stresses of LC & CL specimens are lower than predicted by monotonic (raw) S-S curves,
- yield stresses of LL & CC specimens are slightly higher than monotonic S-S curves,
- LC & CL show a wider range of softening after yielding than LL & CC,
- at large plastic strains, flow stresses of LL & CC converge to raw curve, while lower saturation stresses are observed for LC.

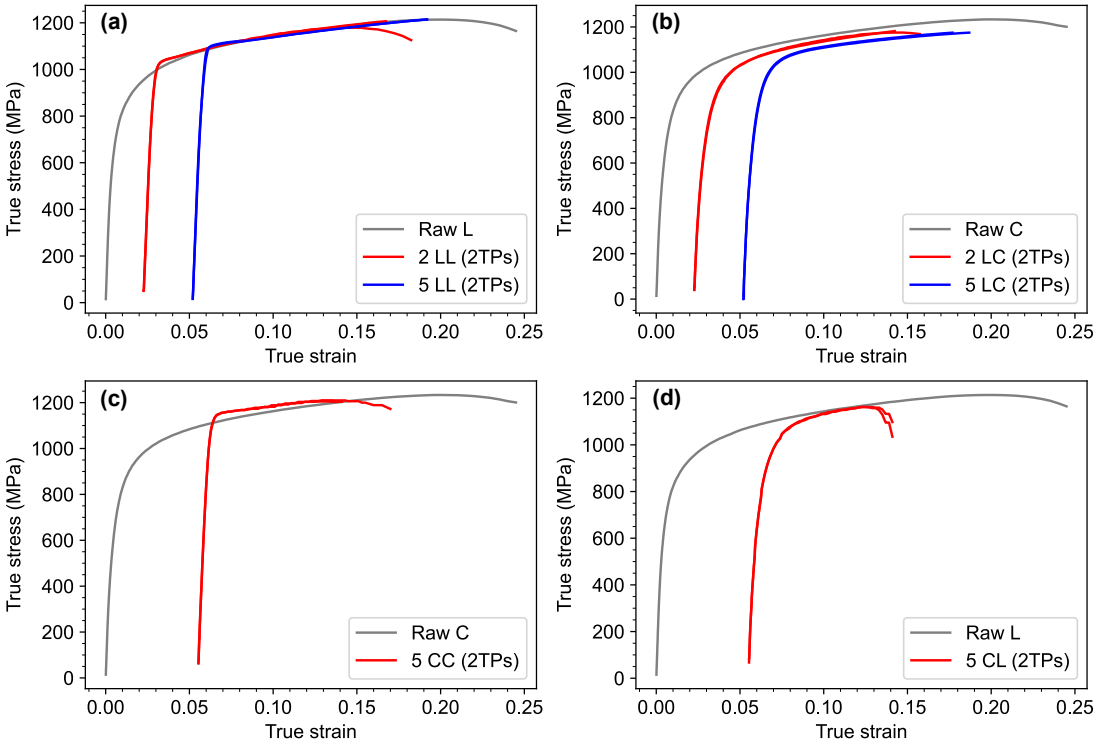

Figure 5.5: Stress-strain curves of (a) LL, (b) LC, (c) CC and (d) CL prestrained samples. The two test pieces with the same case designation are shown in the same color.

It has been reported that dual-phase steels exhibit a temporary increase or decrease in subsequent yield stresses and permanent softening behavior [76], [77]. Comparing S-S curves reveals distinct differences in both reloading yield stress and hardening regions depending on the relative directions of prestrain and reloading. This behavior is known as strain-path dependent anisotropic hardening behavior. Research shows that such history effects are caused by changes in microstructure, such as crystallographic texture, intragranular hardening, the creation of new slip systems, and the rearrangement of dislocation substructure [78], [79].

The traditional yield functions model material anisotropy from initial yield stress ratios or strain ratios but they cannot adequately describe the observed anisotropic hardening phenomena from prestraining. To overcome this limitation, several continuum plasticity models have been proposed for history dependent hardening. Vieira et al. proposed an empirical formula to predict the occurrence of the early plastic instability during reloading [80]. A modified Swift law was proposed by Fernandes et al. for the increase of subsequent yield stress (back extrapolated stress) and reduced hardening rate in uniaxial reloading of prestrained materials [81]. Yoshida et al., [82], [83] modelled the plastic strain induced anisotropy by the nonlinear interpolation function of two yield surfaces. Similarly, He et al. proposed a fourth-order polynomial function to interpolate anisotropy parameters of Yld2000-2d yield criterion at different equivalent plastic strains [84]. Larsson et al. used a non-quadratic yield function Yld2003 [85] with optimized hardening parameters to model the anisotropy evolution of high strength steels [86]. Hu et al. introduced an alternative fourth-order yield function with direction dependent hardening constants to replicate hardening-induced anisotropy [87]. Other approaches such as Teodosiu-Hu [88], Suprun [89], modified Qin-Holmedal-Hopperstad (QHH) [90], Homogeneous Anisotropic Hardening (HAH) [91], manipulate the evolution of yield surface during plastic deformation to connect anisotropic hardening and anisotropic yielding. For example, original HAH yield function coefficients were modified to include latent hardening effects such as overshoot of the reloading yield stress [92], multiple load changes [93] and permanent softening [94]. However, these formulations are complex and require extensive experimental data obtained from uniaxial tensile/compressive tests and biaxial tensile tests.

In this study, a simpler and more practical approach to predict the strain path-dependent anisotropic hardening behavior is presented. The primary objective of this model is to precisely predict different hardening behaviors following a change in strain path, while also fitting the stress-strain curves during reloading of prestrained specimens. This approach is inspired by the work of Fernandes et al. [81], where the Swift equation is supplemented with additional parameters to account for anisotropic harden-

ing. This method uses the data from uniaxial tensile tests with L and C prestrains and a heuristic algorithm is combined with the widely used anisotropic yield function Hill48 for plane stress.

5.4 Development of Prestrain Induced Anisotropic Hardening Model

In this section, an empirical equation for the prestrain-induced anisotropic hardening will be derived. The model is based on a modified Swift equation [81] and with extra coefficients from the prestrain history.

Firstly, let us define the unit vectors of prestrain and reloading directions. It is assumed that the unit vectors are aligned with one of the material orthotropy directions.

$$\boldsymbol{e}_{pre} = \begin{cases} \boldsymbol{e}_L, \ \varepsilon^p_{xx} > 0 \\ \boldsymbol{e}_C, \ \varepsilon^p_{yy} > 0 \end{cases}, \text{after prestrain.} \tag{5.2}$$

The S-S curves for 0-degree reloading (LL/CC) and 90-degree reloading (LC/CL) can be categorized into two types of curves as shown in Fig. 5.6. Let us assume both curves have the form shown in Eq. (5.3):

$$\sigma^* = gK\left(\varepsilon_0 + \varepsilon_{pre}\delta + \varepsilon^*_p\right)^{n^*}, \ \ \varepsilon^*_p \leq \varepsilon_{sat}, \tag{5.3}$$

$$\delta = \boldsymbol{e}_{pre} \cdot \boldsymbol{e}_r. \tag{5.4}$$

5.4.1 Derivation of g and n^*

The two unknowns g and n^* can be determined by the following two conditions: reloading yield stress and saturation stress points which are illustrated as point A and B respectively in Fig. 5.6.

At point A (end of elastic reloading), the plastic strain is equal to the prestrain since no additional plastic strain is accumulated. Hence, $\varepsilon_p = \varepsilon_{pre}$ and $\varepsilon^*_p = 0$. The reloading yield stress is given by:

$$\sigma^*_A = Y_r \ \sigma_A, \tag{5.5}$$

$$gK\left(\varepsilon_0 + \varepsilon_{pre}\delta\right)^{n^*} = Y_r \ K\left(\varepsilon_0 + \varepsilon_{pre}\right)^n, \tag{5.6}$$

$$g = Y_r \frac{\left(\varepsilon_0 + \varepsilon_{pre}\right)^n}{\left(\varepsilon_0 + \varepsilon_{pre}\delta\right)^{n^*}}. \tag{5.7}$$

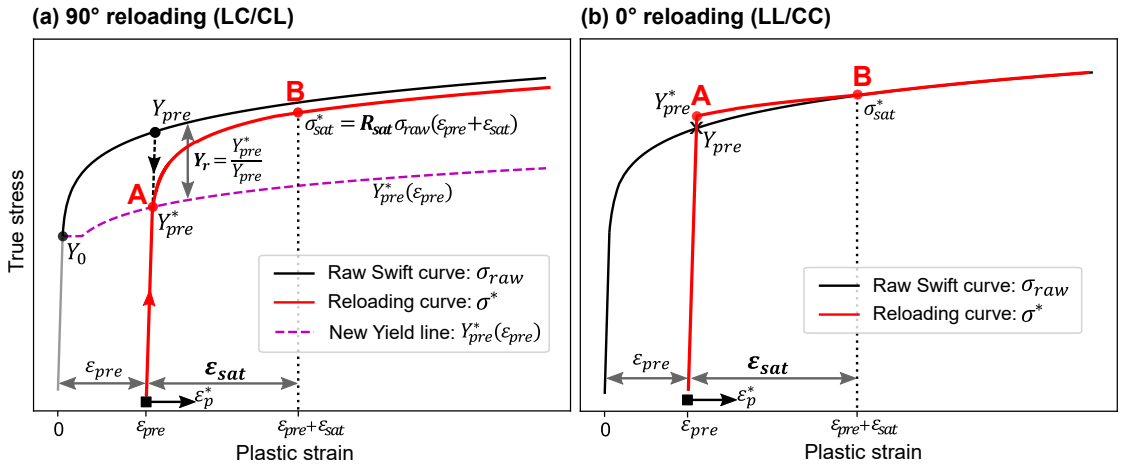

Figure 5.6: Schematic illustration of reloading curves and model parameters for (a) LC/CL and (b) LL/CC

At point B, $\varepsilon_p = \varepsilon_{pre} + \varepsilon_{sat}$, and $\varepsilon^*_p = \varepsilon_{sat}$, where the saturation strain ε_{sat} is defined as the plastic strain offset where the reloading curve converges to the raw Swift curve. The saturation stress σ^*_{sat} is controlled by the *saturation stress ratio* parameter R_{sat} such that $\sigma^*_{sat} = R_{sat}\sigma_{sat}$.

$$\sigma^*_{sat} = R_{sat}\sigma_{sat} = R_{sat}K\left(\varepsilon_0 + \varepsilon_{pre} + \varepsilon_{sat}\right)^n. \tag{5.8}$$

But,

$$\sigma^*_{sat} = gK\left(\varepsilon_0 + \varepsilon_{pre}\delta + \varepsilon_{sat}\right)^{n^*}, \tag{5.9}$$

$$\sigma^*_{sat} = Y_r\frac{\left(\varepsilon_0 + \varepsilon_{pre}\right)^n}{\left(\varepsilon_0 + \varepsilon_{pre}\delta\right)^{n^*}}K\left(\varepsilon_0 + \varepsilon_{pre}\delta + \varepsilon_{sat}\right)^{n^*}, \tag{5.10}$$

$$\sigma^*_{sat} = Y_rK\left(\varepsilon_0 + \varepsilon_{pre}\right)^n\left(\frac{\varepsilon_0 + \varepsilon_{pre}\delta + \varepsilon_{sat}}{\varepsilon_0 + \varepsilon_{pre}\delta}\right)^{n^*}, \tag{5.11}$$

$$\log\sigma^*_{sat} = \log\left[Y_rK\left(\varepsilon_0 + \varepsilon_{pre}\right)^n\right] + n^*\log\left(\frac{\varepsilon_0 + \varepsilon_{sat} + \varepsilon_{pre}\delta}{\varepsilon_0 + \varepsilon_{pre}\delta}\right), \tag{5.12}$$

$$n^* = \frac{\log\sigma^*_{sat} - \log\left[Y_rK\left(\varepsilon_0 + \varepsilon_{pre}\right)^n\right]}{\log\left(\frac{\varepsilon_0+\varepsilon_{sat}+\varepsilon_{pre}\delta}{\varepsilon_0+\varepsilon_{pre}\delta}\right)}. \tag{5.13}$$

Substituting g from Eq. (5.7) and n^* from Eq. (5.13) into Eq. (5.3) gives the reloading hardening curve after prestrain which satisfies the conditions shown in Fig. 5.6.

After the saturation point, the reloading hardening curve follows the raw curve by the factor R_{sat}:

$$\sigma^* = R_{sat}\sigma_{raw} = R_{sat}K\left(\varepsilon_0 + \varepsilon_{pre} + \varepsilon^*_p\right)^n, \quad \varepsilon^*_p > \varepsilon_{sat}. \tag{5.14}$$

	Y_r	ε_{sat}	R_{sat}
LL	1.03	0.06	1.00
LC	0.70	0.035	0.94 - 0.98
CL	0.72	0.035	1.00
CC	1.04	0.08	1.00

Table 5.5: Fitted parameters for the anisotropic hardening model

Hence, the reloading curve for full strain range can be obtained by combing Eq. (5.3) and Eq. (5.14):

$$\sigma^* = \begin{cases} gK\left(\varepsilon_0 + \varepsilon_{pre}\delta + \varepsilon_p^*\right)^{n^*}, \ \varepsilon_p^* \leq \varepsilon_{sat} \\ R_{sat}K\left(\varepsilon_0 + \varepsilon_{pre} + \varepsilon_p^*\right)^{n}, \ \varepsilon_p^* > \varepsilon_{sat} \end{cases}. \tag{5.15}$$

5.4.2 Input parameters

In addition to the raw Swift parameters (K, ε_0, n^*), three additional parameters are needed to determine g and n^* in Eq. (5.15), namely $\{Y_r, \varepsilon_{sat}, R_{sat}\}$. The parameter set was defined for each prestrain-reloading pair, namely LL, LC, CL and CC, resulting in a total of 12 parameters. Putting them into a matrix $\boldsymbol{H}$ allows the use of vector notation for the hardening law:

$$\boldsymbol{H} = \begin{bmatrix} Y_{rLL} & Y_{rLC} & Yr_{rCL} & Yr_{rCC} \\ \varepsilon_{satLL} & \varepsilon_{satLC} & \varepsilon_{satCL} & \varepsilon_{satCC} \\ R_{satLL} & R_{satLC} & R_{satCL} & R_{satCC}. \end{bmatrix} \tag{5.16}$$

The parameters are found by fitting the experimental stress-strain curves to Eq. (5.3). Each parameter has its physical meaning and can be easily identified without complicated inverse optimization analysis. The fitted parameters to the current data are shown in Table 5.5.

5.4.3 2D plane stress condition

In order to implement the anisotropic hardening model in the finite element code, the multiaxial stress state need to be considered. Since the formulation up to here is based on uniaxial loading, it has very limited applicability. The multi-axial stress state (such as biaxial loading) can be commonly converted to an equivalent uniaxial stress by using a yield function such as Mises, Tresca or Hill functions.

$$\sigma_{eqv} = f(\boldsymbol{\sigma}, \varphi), \tag{5.17}$$

where φ is the set of parameters describing the material properties. For plane stress, the independent stress components are σ_{xx}, σ_{yy} and σ_{xy}. In this section, Hill48 yield function is used to convert the multi-axial stress state to equivalent stress with material parameters derived from the anisotropic hardening law in Eq. (5.15).

First, the unit directional vectors for material orthotropy axes $\boldsymbol{e}_x, \boldsymbol{e}_y$ and the prestrain direction $\boldsymbol{e}_{pre}$ which can be determined in priori or during the unloading state of the simulation:

$$\boldsymbol{e}_x = \begin{pmatrix} 1 \\ 0 \end{pmatrix}, \boldsymbol{e}_y = \begin{pmatrix} 0 \\ 1 \end{pmatrix}, \ \boldsymbol{e}_{pre} = \begin{cases} \boldsymbol{e}_x \\ \boldsymbol{e}_y \end{cases}, \tag{5.18}$$

and coefficient matrices for L-prestrain and C-prestrain,

$$\boldsymbol{M}_{pre,L} = \begin{pmatrix} 1 & 0 \\ 0 & 1 \\ 0 & 0 \\ 0 & 0 \end{pmatrix}, \ \boldsymbol{M}_{pre,C} = \begin{pmatrix} 0 & 0 \\ 0 & 0 \\ 1 & 0 \\ 0 & 1 \end{pmatrix}. \tag{5.19}$$

The new parameter matrix $\boldsymbol{H}^*$ can be calculated depending on the prestrain direction (L or C),

$$\boldsymbol{H}^* = \boldsymbol{H}\boldsymbol{M}_{preL/C}^T, \tag{5.20}$$

$$\boldsymbol{H}_x^* = \boldsymbol{H}^*\boldsymbol{e}_x = \begin{pmatrix} Y_r \\ \varepsilon_{sat} \\ R_{sat} \end{pmatrix}_x, \ \boldsymbol{H}_y^* = \boldsymbol{H}^*\boldsymbol{e}_y = \begin{pmatrix} Y_r \\ \varepsilon_{sat} \\ R_{sat} \end{pmatrix}_y. \tag{5.21}$$

δ is calculated from the dot product of material direction vectors and the prestrain direction vector:

$$\delta_x = \boldsymbol{e}_x \cdot \boldsymbol{e}_{pre}, \ \delta_y = \ \boldsymbol{e}_y \cdot \boldsymbol{e}_{pre}. \tag{5.22}$$

Let the right-hand side of Eq. (5.3) represent by function alias f_1. Then, saturation stress is calculated using $\boldsymbol{H}_x^*$ and $\boldsymbol{H}_y^*$ parameter sets:

$$\sigma_{sat,x}^* = f_1\left(\boldsymbol{H}_x^*\right), \ \sigma_{sat,y}^* = f_1\left(\boldsymbol{H}_y^*\right), \tag{5.23}$$

Then, n_x^* and n_y^* can be calculated from Eq. (5.13) which is represented by f_2:

$$n_x^* = f_2\left(\boldsymbol{H}_x^*, \delta_x, \sigma_{sat,x}^*\right), \ n_y^* = f_2\left(\boldsymbol{H}_y^*, \delta_y, \sigma_{sat,y}^*\right). \tag{5.24}$$

Likewise, g_x and g_y can be calculated from Eq. (5.7) which is represented by f_3:

$$g_x = f_3\left(\boldsymbol{H}_x^*, \delta_x, n_x^*\right), \ g_y = f_3\left(\boldsymbol{H}_y^*, \delta_y, n_y^*\right). \tag{5.25}$$

Finally, σ_x^* and σ_y^* can be calculated from Eq. (5.3) for each ε_p^*:

$$\sigma_x^* = f_4\left(g_x, n_x^*, \delta_x, \varepsilon_p^*\right),\ \sigma_y^* = f_4\left(g_y, n_y^*, \delta_y, \varepsilon_p^*\right). \tag{5.26}$$

Equation (5.26) is used to update the anisotropic parameters of the yield function for each strain increment step during the numerical simulation. In this study, Hill quadratic [95] yield criterion was used as it allows the determination of its parameters based solely on two uniaxial tensile tests conducted along the orthotropic axes and an in-plane shear test. In addition,it is a simple and widely accepted representation of the material's anisotropy state in terms of stress ratios in two perpendicular axes (R_{xx}, R_{yy}) and one shear axis (R_{xy}). Moreover, the Bauschinger effect can be accounted for by incorporating a back stress formulation using data from tension-compression tests. While there are more complex anisotropic yield functions, Hill48 has the advantage of being concise and easy to use, which allows fast adoption of the model in the industry. The equivalent stress for this yield criterion is defined as:

$$\bar{\sigma} = \sqrt{F\sigma_{yy}^2 + G\sigma_{xx}^2 + H\left(\sigma_{xx} - \sigma_{yy}\right)^2 + 2N\tau_{xy}^2}, \tag{5.27}$$

$$F = \frac{1}{2}\left[\frac{1}{R_{yy}^2} + \frac{1}{R_{zz}^2} - \frac{1}{R_{xx}^2}\right], \tag{5.28}$$

$$G = \frac{1}{2}\left[\frac{1}{R_{zz}^2} + \frac{1}{R_{xx}^2} - \frac{1}{R_{yy}^2}\right], \tag{5.29}$$

$$H = \frac{1}{2}\left[\frac{1}{R_{xx}^2} + \frac{1}{R_{yy}^2} - \frac{1}{R_{zz}^2}\right], \tag{5.30}$$

$$L = \frac{3}{2R_{yz}^2},\ M = \frac{3}{2R_{zx}^2},\ N = \frac{3}{2R_{xy}^2}, \tag{5.31}$$

$$R_{xx} = \frac{\sigma_x^*}{\sigma(\bar{\varepsilon}_p)}R_{xx}^0, R_{yy} = \frac{\sigma_y^*}{\sigma(\bar{\varepsilon}_p)}R_{yy}^0, R_{xy} = 0.5\left(R_{xx} + R_{yy}\right), \tag{5.32}$$

where $\bar{\varepsilon}_p$ is the equivalent plastic strain. The equation for R_{xy} is an assumption which is validated by fitting the uniaxial tensile tests of 45° specimens to the material axis in Section 5.6.4. Using the proposed hardening model, the anisotropy parameters (R_{xx}, R_{yy}) are dynamically updated in each strain increment step.

5.5 Validation of the Material Model with Simple Nonlinear IGA

A simple IGA model of a thin plate shown in Fig. 5.7 is used to verify the developed material model using JWRIAN-IGA. The strain history is prescribed to match the experiment cases listed in Table 5.4.

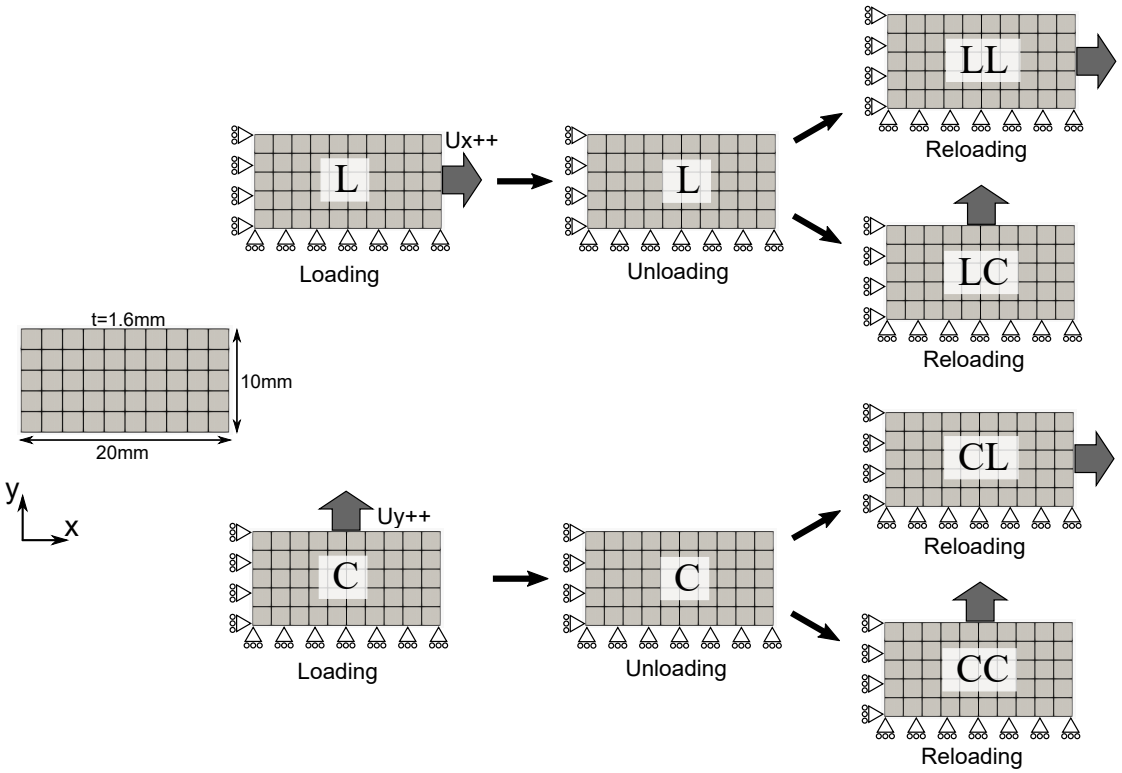

Figure 5.7: Validation model, boundary conditions and loading histories

The traditional return-mapping algorithm is used to calculate trial stress and plastic strain increments in each load step. Once the return-mapping iterations have converged, the prestrained-hardening subroutine uses each integration point to calculate the updated stress in each material axis based on Eq. (5.15). The updated stresses are then used to modify the stress ratios of the Hill48 yield function in which are saved as history variables for the next load step. To ensure the numerical stability of the algorithm, the stress ratios are kept constant during return-mapping iterations, meaning that the yield surfaces can only expand isotropically in each iteration. During highly anisotropic states (just after yielding), the strain increments must be small ($0.02\,\%$ to $0.1\,\%$) to prevent large deviation from the actual yield surface.

5.6 Results and Discussion

5.6.1 Simulation time history for LC configuration

Figure 5.8 shows the evolution of various state variables in the numerical simulation for 5LC case. The time history can be divided into three phases: prestraining, elastic unloading and reloading. During the prestraining phase, a prescribed displacement in the X-direction was incrementally applied until the desired plastic strain was reached. Subsequently, the plate was elastically unloaded until the stress-XX reached zero in the unloading phase. In the reloading phase, a prescribed displacement was applied in the Y-direction to induce stress-YY. Although the specimen cutting operation was not explicitly simulated, the strain paths replicate those of the experiment.

From Fig. 5.8(a) and (c), anisotropic hardening was activated following unloading, as R_x and R_y promptly became equal to $Y_{r,LL}$ and $Y_{r,LC}$, respectively. In the reloading phase, R_y increased and saturated at $R_{sat,LC}.R_y^0$, while R_x saturated at $R_{sat,LL}.R_x^0$ at their respective saturation strains. As a result, the anisotropic uniaxial stress-strain curves can be seen in Fig. 5.8(b).

The equivalent plastic strain which corresponds to the energy conjugate of equivalent stress monotonically increases while individual plastic strain components may decrease. The hardening equation in Eq. (5.3) employs the equivalent reloading plastic strain as its argument. In this case, the reloading plastic strain, denoted as ε_p^*, is calculated as the difference between the total plastic strain $(\bar{\varepsilon}_p)$ and the prestrain (ε_{pre}) which starts from zero during the reloading phase. Since equivalent plastic strain is a scalar, the algorithm necessitates tracking the direction of the prestrain load to correctly calculate the $\boldsymbol{e}_{pre}$ and $\boldsymbol{M}_{pre}$ vectors. Alternatively, if the prestrain direction and pre-plastic strain value are known in advance, they can be manually input into the algorithm.

5.6.2 Simulation time history for LL configuration

Figure 5.9 shows the simulation time history for 5LL case. Following the prestrain phase, the values of R_x and R_y were identical to those of the 5LC case as both cases underwent the same prestrain loading. However, the reloading curve for σ_x shows a slight overshoot as $Y_r = 1.03$ and then converges to the raw curve at saturation. This is in contrast to the slower work hardening of σ_y observed in Fig. 5.8(b).

5.6.3 Comparison with experiments

Figure 5.10 shows the comparison between the stress-strain curves from experiments and simulations for each load case. The dashed curves defining reloading yield stress

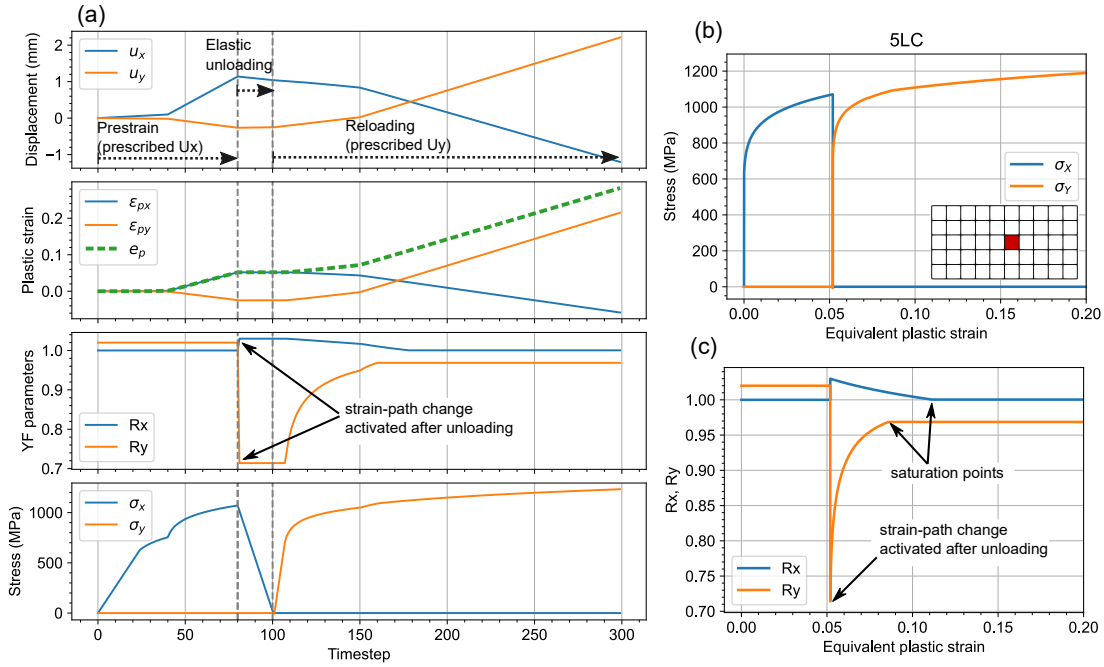

Figure 5.8: Simulation results for 5LC case; (a) Simulation time history of displacements, plastic strain, yield function parameters and stress state, (b) stress-strain curve in X and Y directions, (c) evolution of yield stress ratios with equivalent plastic strain

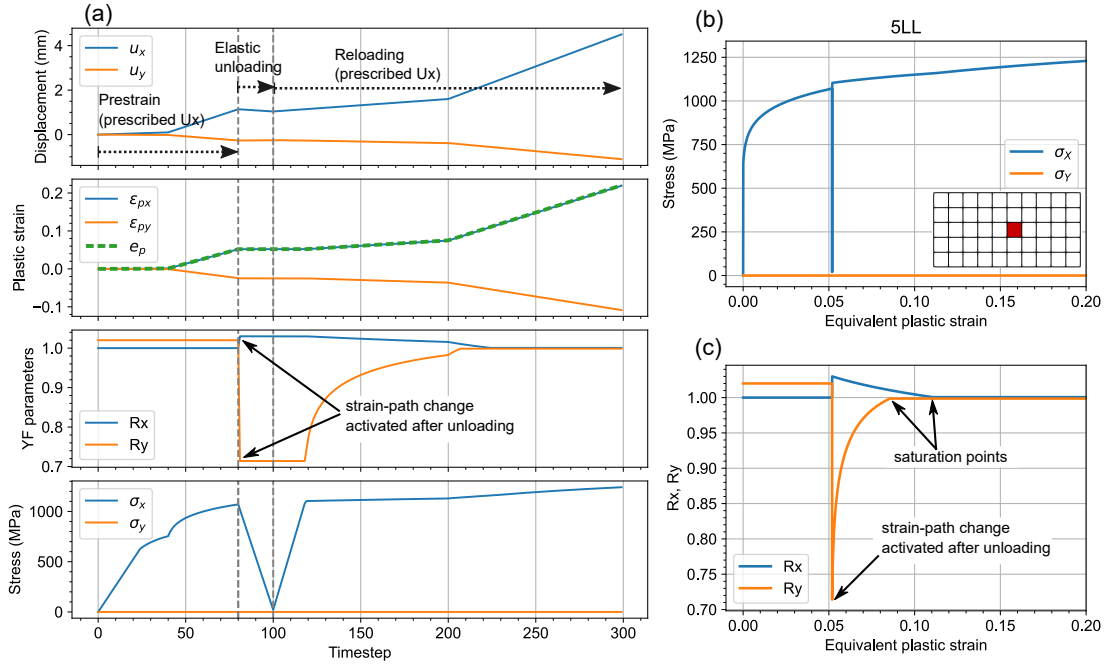

Figure 5.9: Simulation results for 5LL case; (a) Simulation time history of displacements, plastic strain, yield function parameters and stress state, (b) stress-strain curve in X and Y directions, (c) evolution of yield stress ratios with equivalent plastic strain

for LC & CL cases are extrapolated from the experiment data for all strain ranges. The anisotropic hardening model with calibrated parameters show good agreement with the experimental results, capturing essential characteristics such as high-rate, slow work hardening in LC/CL, and low-rate, abrupt hardening behaviors in LL/CC. In the experimental reloading curves for LC and CL, there is a slight change in the elastic modulus compared to the initial value from the raw curve. But this effect is not considered in the current study and hence there are slight differences in the elastic reloading range. Overall, the simulations successfully reproduced the flow stresses at large plastic strains using the strain-path dependent anisotropic hardening model. Optimization of input parameters (Section 5.4.2) is recommended as more experiment data becomes available to improve the predictive ability of the model.

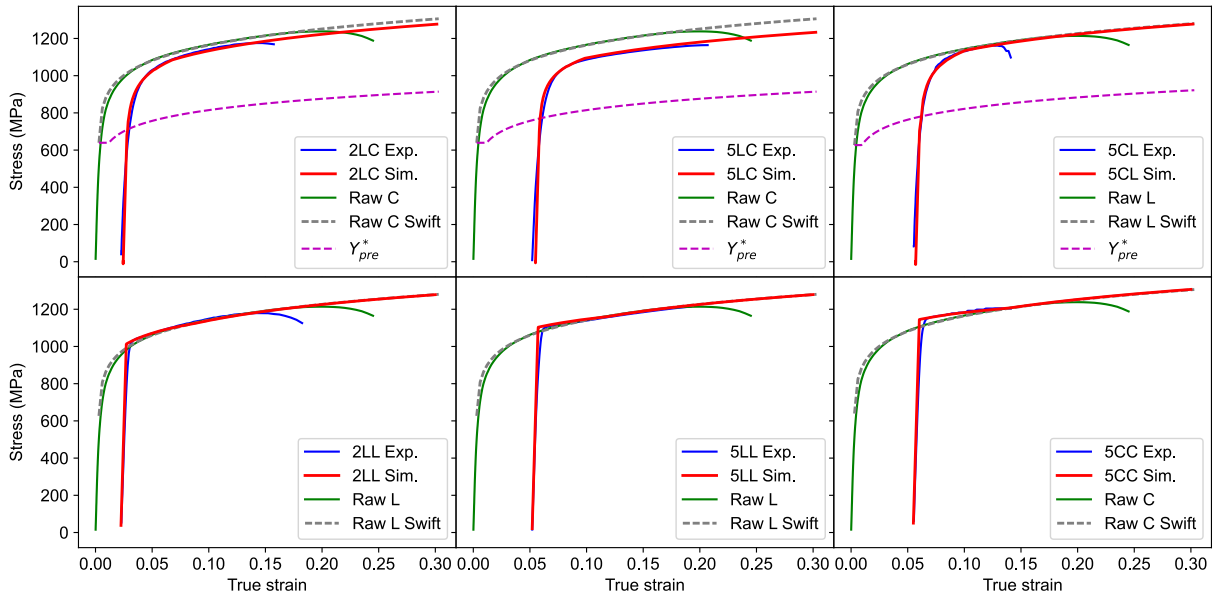

Figure 5.10: Comparison of S-S curves from the experiments and simulation results from the simple validation model

5.6.4 Intermediate reloading angles

The results in the previous section showed that the proposed anisotropic hardening model can accurately predict the anisotropic hardening behavior after prestrain for uniaxial loading along a material axis. In order to check the applicability of the model to stress states other than which the model is calibrated for, two additional tensile tests of $5\,\%$ L-prestrained specimen in $45°$ and $60°$ reloading directions were conducted as shown in Fig. 5.11(a). The reloading yield stress at arbitrary loading angles can be then calculated from the yield function and equivalent stress. The predicted yield stresses in

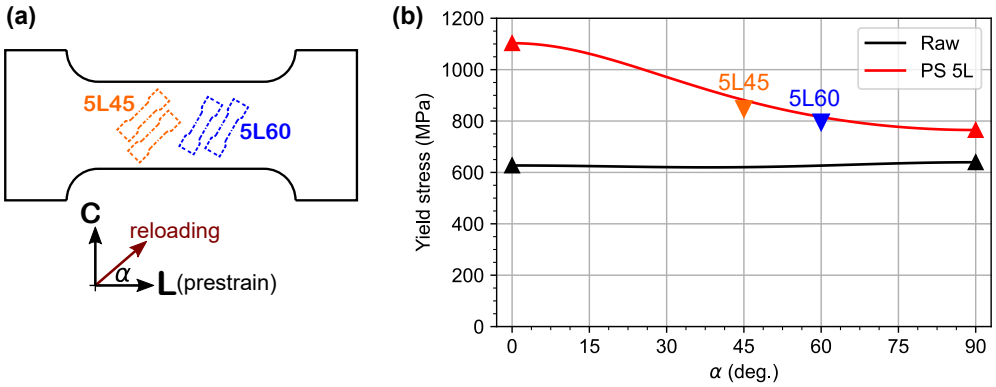

Figure 5.11: (a) Tensile test specimens in $45°$ and $60°$ to 5L prestrain direction, (b) Equivalent stress at arbitrary loading angles calculated from Hill48 function. represent experimental yield stresses at $0.2\,\%$ offset strain for reloading in 00/90 and 45/60 directions, respectively.

Fig. 5.11(b) show good agreement with experimental yield stresses taken at $0.2\,\%$ offset strain. The comparison in Fig. 5.12 shows that the equivalent stress from yield function with the 5LL and 5LC parameters can reproduce the stress-strain curves of 5L45 and 5L60 specimens.

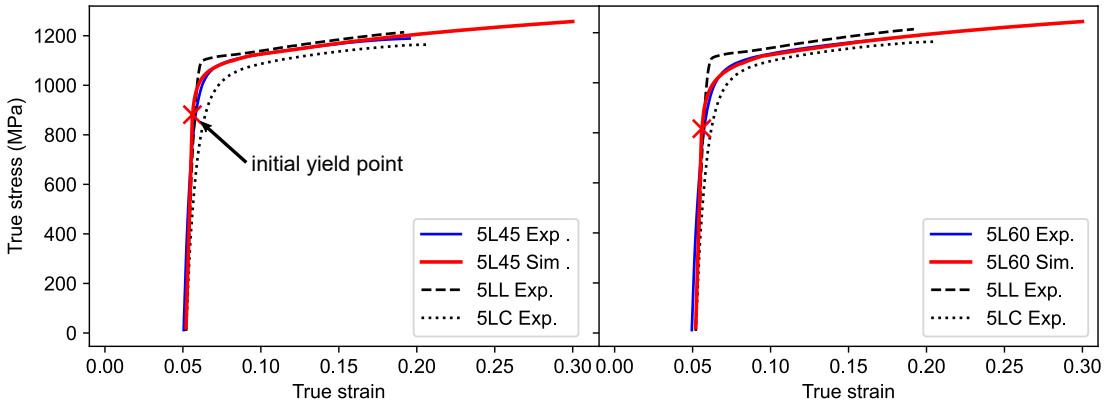

Figure 5.12: Simulation and experimental reloading curves for $45°$ and $60°$ reloading directions after $5\,\%$ L-prestrain

5.7 Summary

In this study, a strain-path dependent hardening model was developed from the experimentally observed anisotropic behavior of prestrained DP980 steel. The anisotropic hardening occurs due to differences in prestraining and reloading axes. The model accurately replicates key characteristics in the uniaxial stress-strain curves, including the

variations in reloading yield stress, hardening rates and permanent softening. It has a straightforward formulation that can be easily implemented in practical applications, and it requires only a few parameters that can be obtained directly from uniaxial tensile tests.

The proposed model is validated using a plane stress case with the Hill48 anisotropic yield criterion in elastoplastic IGA. The results demonstrated good agreement with experimental data across all load cases and successfully reproduced the anisotropic hardening behavior when the strain path was altered. The anisotropy parameters are used to predict equivalent stress in intermediate reloading directions and comparison with experiments showed good accuracy. Future work for this research includes the investigation of Bauschinger effect and evolution of back-stress due to prestraining from cyclic loading experiments. Application of the material model in more complex geometries using IGA is also recommended.

Chapter 6

Conclusions and Outlook

6.1 Conclusions

The main objectives of this research are to develop a numerical framework for isogeometric analysis and to investigate the applicability of IGA in the field of structural health monitoring and nonlinear material models. Specifically, the integration of IGA and distributed fiber optic sensing is one of the outcomes of this research. On top of that, a new anisotropic hardening model was developed for high strength steel subjected to prestrains. All models were implemented in the IGA code and validated with reference solutions and experimental data.

Firstly, in-house code JWRIAN-IGA was developed for linear elastic and elastoplastic solid mechanics as a foundation for IGA-related studies. The code is based on original IGA formulation by Hughes et.al, using NURBS basis functions and was implemented in FORTRAN. The supporting algorithms such as h-refinement, multi-patch coupling, geometric tools and solution interpolation were also developed. Using the IGA code, newly proposed methods for distributed fiber optic sensing and nonlinear material modelling were investigated.

In the first part of the thesis, a method for the integration of IGA and DFOS was proposed using the numerical fiber model. The numerical properties of the fiber model and their effects on the measurability of surface strains were studied. The numerically computed fiber strains were compared with experiment data from the deformation of a cylindrical pipe. The idealized loading conditions showed discrepancy in the simulated fiber strains which was improved by using optimized loading conditions. Hence, the following conclusions were drawn from the study:

- the modelling and analysis of fiber strains is efficient with a few DOF and adaptable

to DFOS parameters thanks to exact geometry representation,

- DFOS strain measurements with centimeter resolution, combined with the digital model, can capture the deformation with high spatial resolution,
- unknown loadings on a structure can also be predicted using IGA and the fiber model with less than $4\,\%$ error in the demonstration model,
- the accuracy of predicted loading is dependent on whether the optimization parameters are set up properly. The optimization parameters can be determined from the observed fiber strain distribution and prior knowledge about the structure.

In the second part, an analytical method of inverse IGA in which the displacement field is reconstructed from measured fiber strains was proposed. In this method, no optimization problem setup is necessary which greatly increases the efficiency and reliability of the solution. The optimality conditions are derived from the variational problem considering the least-squares constraint between the analytical and measured fiber strains. The method was validated with four numerical examples where reference solutions were used to produce fiber strains and to compare against the inverse solutions. The validation and sensitivity studies showed that:

- the inverse IGA-DFOS is accurate (displacement error $< 0.1\,\%$) and robust under various geometry, fiber layout and loading conditions,
- error ceilings dramatically improve when the sampling interval is smaller than geometric features such as curvature of the fiber,
- local stress concentrations can be detected by the inverse analysis although accuracy depends on the relative sampling interval,
- mean displacement errors increase linearly with noise levels,
- signal-to-noise ratio is a crucial factor in determining the error bounds of the inverse solution, with maximum errors up to $25\,\%$ in the case studies.

The inverse IGA-DFOS was applied to estimate the deformation of a rotating impeller plate using measured fiber strains from front and back sides of the plate. The study showed that the inverse analysis can:

- output a smooth displacement distribution even though input fiber strains are sparse and noisy,
- give both global deformation shape and local changes,
- reproduce the measured fiber strains with less than $0.1\,\%$ maximum error,
- estimate stress distribution and stress concentration zones.

Spurious local stress concentrations were found in the stress results which were not visible in the displacement field, the reason being the uncertainty of fiber position in relatively small scales. This is the limitation of the model which can be overcome by using multiple parallel fibers to reduce uncertainty. Temperature effects on the fiber and structure can be integrated into the model in the future to make it fully automated.

In the final part of the thesis, anisotropic hardening of prestrained high strength steel DP980 was experimentally studied and a new hardening model was proposed to replicate the observed phenomena. The uniaxial tensile tests were conducted for small prestrained specimens in four categories of prestrain and reloading directions. The non-linear work-hardening portion of the resulting stress-strain curves are modelled with modified Swift equation and the input parameters are derived. The proposed model has the merit of simplicity since all parameters have physical meaning and can be identified from uniaxial stress-strain curves. Then, the model was implemented in elastoplastic IGA code and numerical simulations were compared with experiments. The following conclusions were drawn from the study:

- subsequent yield stress in 90° reloading direction is much lower than 0° reloading direction,
- the reloading stress strain curves have transient effects such as overshoot or undershoot from the raw curve,
- 90° reloading specimens show wider softening region (higher transient ductility) than 0° counterparts,
- the reloading curves eventually saturate to the raw curve (or Swift extrapolation) although some cases show permeant softening,
- the simulation results show good agreement with experiments for both calibrated cases and arbitrary reloading directions.

The small changes in elastic modulus and evolution of back-stress after prestrain were not considered in this study. Hence, the model can be further improved by considering these effects from cyclic loading tests and biaxial tensile tests.

6.2 Outlook

IGA is an advanced numerical method which has been developed for more than two decades. As it currently stands, the main difficulty in adopting IGA in industry is CAD data interoperability especially for complex geometries. NURBS has limitations in terms of topology and multi-patch separation has to be used which may not be the most prac-

tical approach. There are several proposals to solve this problem using advanced Splines but there is currently no industry standard. This research is a part of the ongoing effort to expand the applicability of IGA to structural monitoring and nonlinear materials. The proposed methods and implementations in this thesis can be modified to utilize different Spline-based geometries without affecting the major conclusions.

The following research directions are suggested for further development of the proposed methods.

Estimating the error or uncertainty is a salient part of any ill-posed inverse analysis which uses noisy measurement data as input. Sensitivity analysis was performed in the current research using numerical case studies. But a posterior error estimator independent of the geometry and loading conditions may be preferred for better generalization. This is not a trivial task since the uncertainty depends on the strain distribution which in turn relates to the load state. If a reliable general error estimator can be realized, the optimal fiber layout can be determined by minimizing the error. It is likely that the uncertainty cannot be estimated using deterministic methods. In this case, probabilistic methods such as Bayesian inference may be used. Probabilistic methods are increasingly popular in SHM field since they can also provide the error bounds by explicitly considering the uncertainty sources.

Inverse analysis for nonlinear problems is worth investigating for large deformation problems. The solving algorithms have to consider the fiber response to the deformation and nonlinear material behavior. Inverse analysis for non-homogeneous materials is also a frontier research as there are recently developed theories such as zig-zag element formulation for composites. Anisotropy in elastic properties prominent in composite materials can be considered in a modified IGA formulation by taking advantage of high order continuity.

Appendix A

Integration of IGA and DFOS

A.1 Modelling of DFOS fiber

The high-level flow chart for the calculation of fiber strains using developed fiber model is shown in Fig. A.1.

Figure A.2 shows the results of fiber strain calculations from the validation model in Section 3.2.3.

Figure A.3 shows the comparisons of experimental and simulated fiber strains for different prescribed displacement values. The experiment setup is described in Section 3.3.1.

A.2 Inverse analysis of the impeller plate

Figure A.4 shows the measured fiber strains from the impeller experiment at fixed viscosity and different RPMs. The fiber goes from back side to front side of the plate as illustrated in Fig. 4.16. In contrast, Fig. A.5 shows the fiber strains at fixed RPM and different fluid viscosities.

Figure A.6 shows the inverse deformation for different viscosities at fixed RPM. As expected, higher viscosity results in bigger deformation of the plate but they are not linearly proportional. By learning this relation, the inverse analysis can be used to infer the viscosity of the fluid from the structural response.

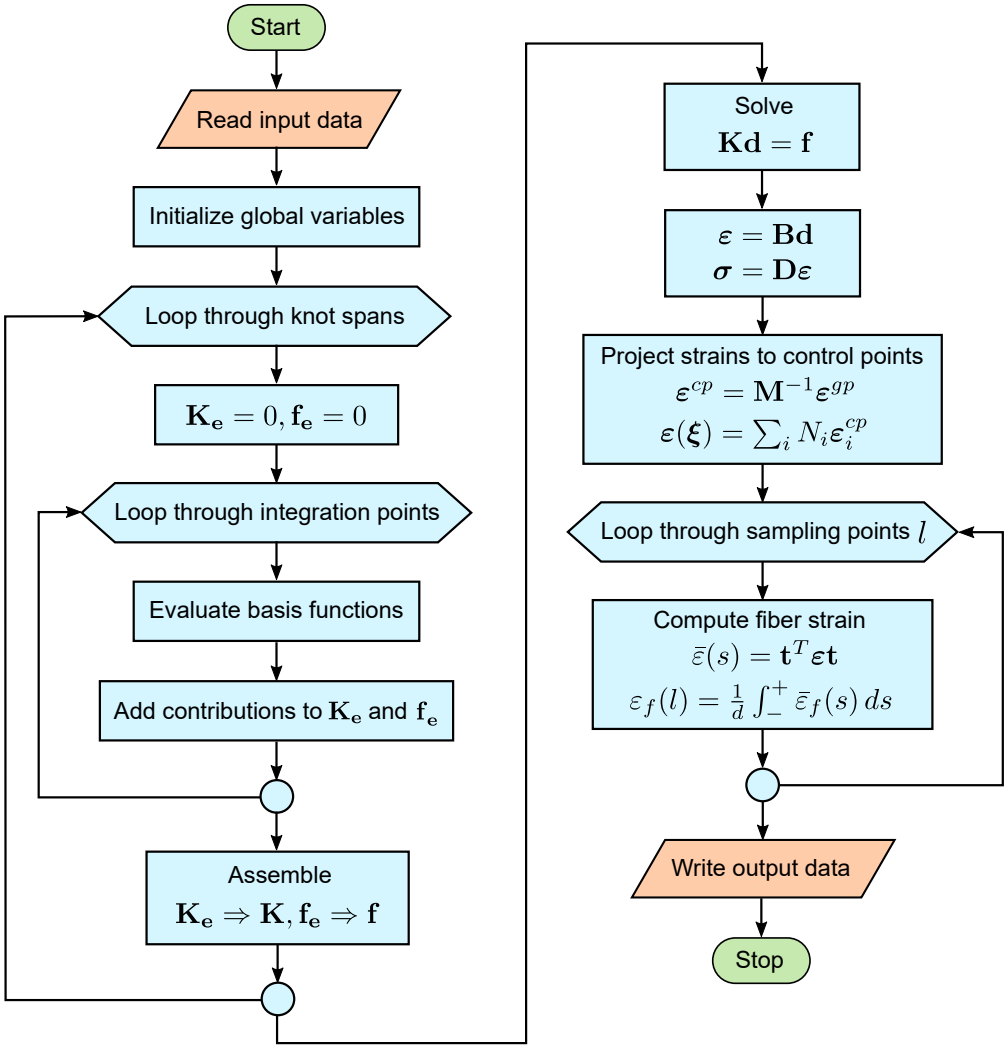

Figure A.1: Flow chart for the calculation of fiber strains from IGA linear elastic analysis

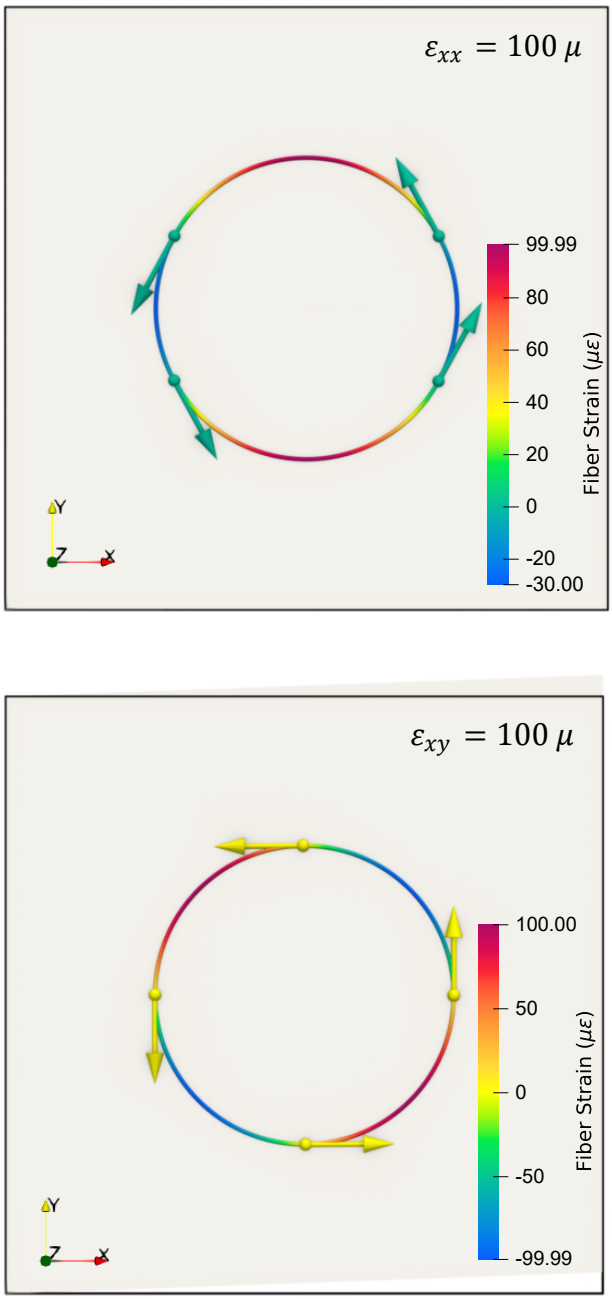

Figure A.2: Simulated fiber strain distributions for (above) pure tensile strain and (below) pure shear strain states. The points and arrows show zero fiber strain positions and their tangential directions.

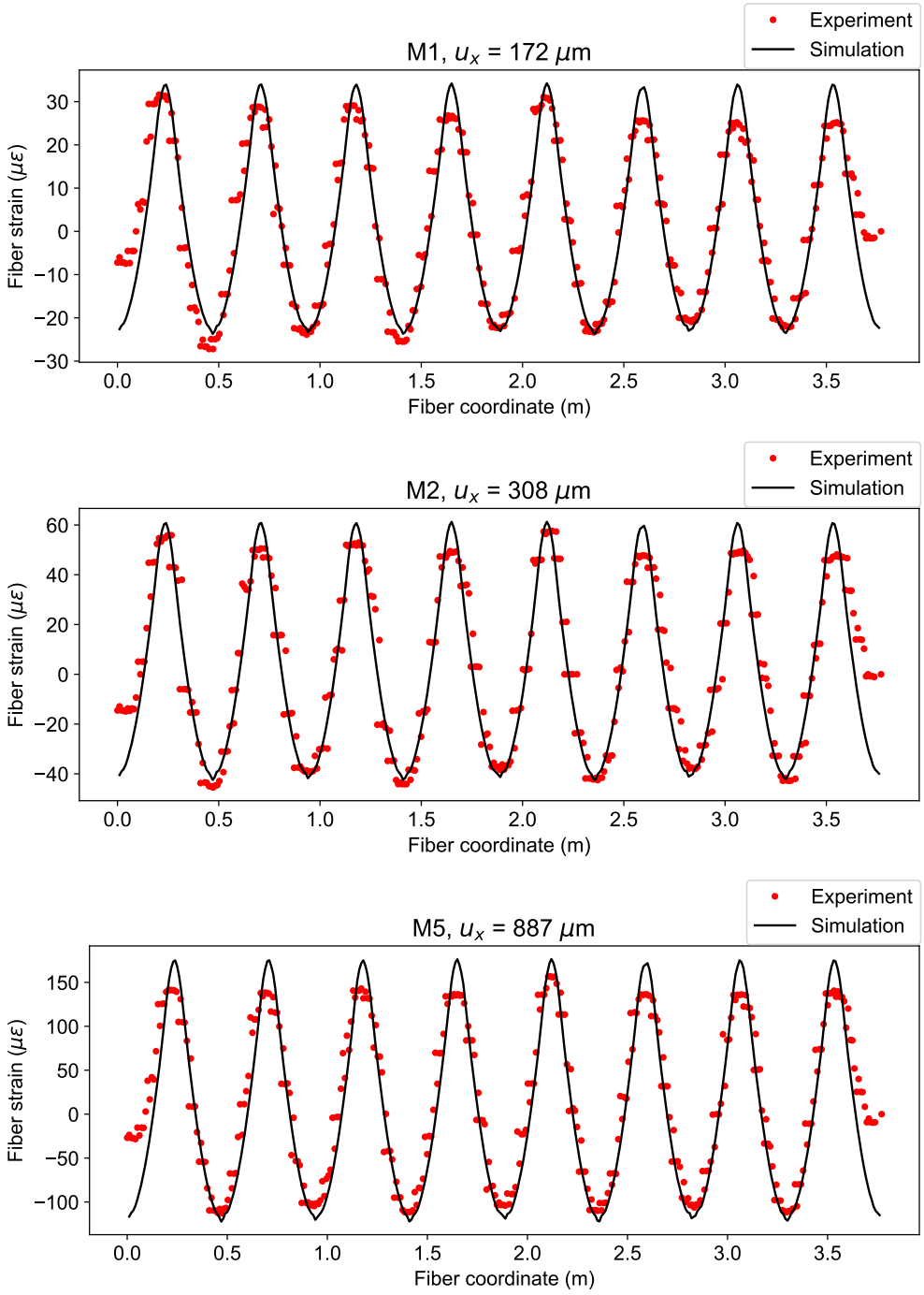

Figure A.3: Fiber strains from PVC pipe ovalization experiment for M1, M2 and M5 load cases. Simulated fiber strains are calculated from point displacements.

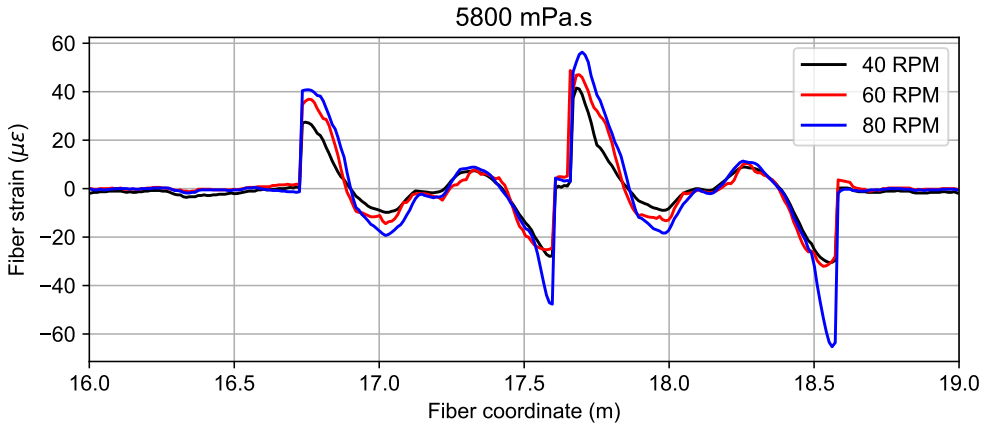

Figure A.4: Measured fiber strains from the impeller experiment at fixed viscosity ($5800\,\mathrm{mPa\,s}$) and different RPMs.

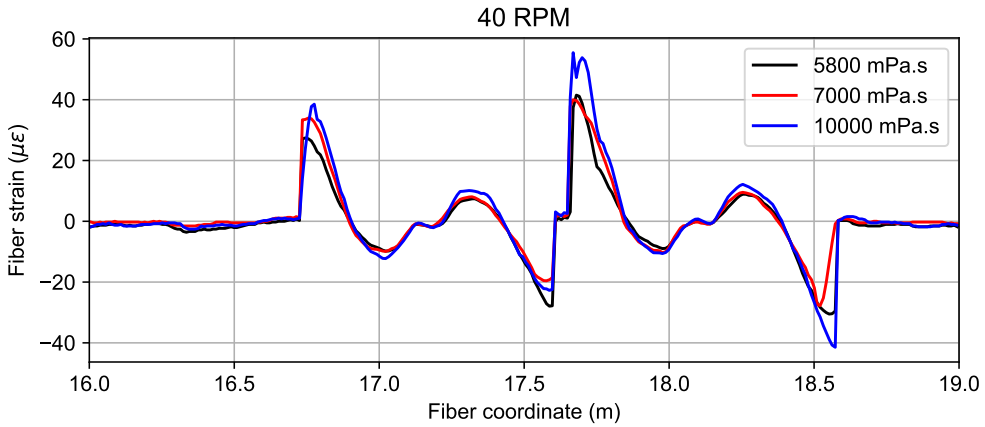

Figure A.5: Measured fiber strains from the impeller experiment at $40\,\mathrm{RPM}$ and different viscosities.

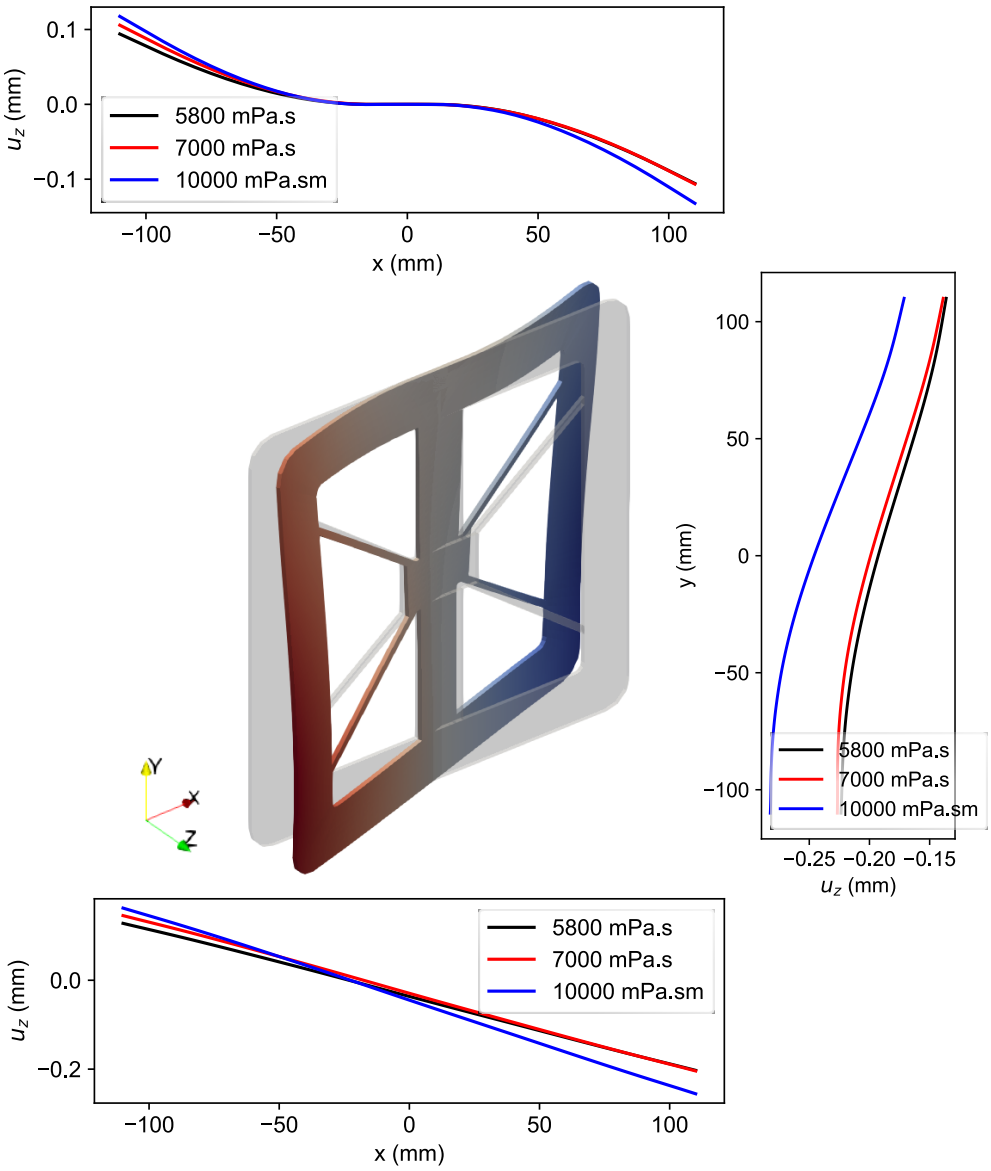

Figure A.6: Deformation profiles from the inverse IGA-DFOS for variable viscosities at 40 RPM.

Bibliography

[1] O. C. Zienkiewicz, R. L. (L. Taylor, J. Z. Zhu, O. C. Zienkiewicz, and O. C. Zienkiewicz, *The finite element method : its basis and fundamentals*. Elsevier Butterworth-Heinemann, 2005, p. 733, ISBN: 9780080472775.

[2] Y. Lai, Y. J. Zhang, L. Liu, X. Wei, E. Fang, and J. Lua, "Integrating cad with abaqus: A practical isogeometric analysis software platform for industrial applications," *Computers and Mathematics with Applications*, vol. 74, pp. 1648–1660, 7 Oct. 2017, ISSN: 08981221. DOI: 10.1016/j.camwa.2017.03.032.

[3] J. A. Cottrell, T. J. R. Hughes, and Y. Bazilevs, *Isogeometric analysis : Toward integration of CAD and FEA*. Wiley, 2009, p. 335, ISBN: 9780470748732.

[4] T. J. Hughes, J. A. Cottrell, and Y. Bazilevs, "Isogeometric analysis: Cad, finite elements, nurbs, exact geometry and mesh refinement," *Computer Methods in Applied Mechanics and Engineering*, vol. 194, pp. 4135–4195, 39-41 Oct. 2005, ISSN: 00457825. DOI: 10.1016/j.cma.2004.10.008.

[5] N. Ma, K. Takata, and N. Shimizu, "Isogeometric analysis and its application to sheet metal forming simulation (in japanese)," *Plastics*, vol. 3, pp. 400–404, 31 2020, ISSN: 2433-8826. DOI: 10.32277/plastos.3.31_400.

[6] W. A. Wall, M. A. Frenzel, and C. Cyron, "Isogeometric structural shape optimization," *Computer Methods in Applied Mechanics and Engineering*, vol. 197, pp. 2976–2988, 33-40 2008, ISSN: 00457825. DOI: 10.1016/j.cma.2008.01.025.

[7] Y. Bazilevs, L. B. D. Veiga, J. A. Cottrell, T. J. R. Hughes, and G. Sangalli, "Isogeometric analysis: Approximation, stability and error estimates for h-refined meshes," *Mathematical Models and Methods in Applied Sciences*, vol. 16, pp. 1031–1090, 07 Jul. 2006, ISSN: 0218-2025. DOI: 10.1142/s0218202506001455.

[8] M. Mishra, P. B. Lourenço, and G. Ramana, "Structural health monitoring of civil engineering structures by using the internet of things: A review," *Journal of Building Engineering*, vol. 48, p. 103 954, 2022, ISSN: 2352-7102. DOI: https://doi.org/10.1016/j.jobe.2021.103954.

[9] S. L. Vazquez, A. Tessler, C. C. Quach, *et al.*, "Structural health monitoring using high-density fiber optic strain sensor and inverse finite element methods," 2005.

[10] C. Kralovec and M. Schagerl, "Review of structural health monitoring methods regarding a multi-sensor approach for damage assessment of metal and composite structures," *Sensors 2020, Vol. 20, Page 826*, vol. 20, p. 826, 3 Feb. 2020, ISSN: 1424-8220. DOI: 10.3390/s20030826.

[11] L. Schenato, "A review of distributed fibre optic sensors for geo-hydrological applications," *Applied Sciences*, vol. 7, p. 896, 9 Sep. 2017, ISSN: 2076-3417. DOI: 10.3390/app7090896.

[12] L. Fan and Y. Bao, "Review of fiber optic sensors for corrosion monitoring in reinforced concrete," *Cement and Concrete Composites*, vol. 120, p. 104 029, Jul. 2021, ISSN: 09589465. DOI: 10.1016/j.cemconcomp.2021.104029.

[13] J. M. López-Higuera, L. R. Cobo, A. Q. Incera, and A. Cobo, "Fiber optic sensors in structural health monitoring," *Journal of Lightwave Technology*, vol. 29, pp. 587–608, 4 2011, ISSN: 07338724. DOI: 10.1109/jlt.2011.2106479.

[14] K. Hotate and M. Tanaka, "Distributed fiber brillouin strain sensing with 1-cm spatial resolution by correlation-based continuous-wave technique," *IEEE Photonics Technology Letters*, vol. 14, pp. 179–181, 2 Feb. 2002, ISSN: 10411135. DOI: 10.1109/68.980502.

[15] K. Lim, L. Wong, W. K. Chiu, and J. Kodikara, "Distributed fiber optic sensors for monitoring pressure and stiffness changes in out-of-round pipes," *Structural Control and Health Monitoring*, vol. 23, pp. 303–314, 2 Feb. 2016, ISSN: 15452255. DOI: 10.1002/stc.1771.

[16] R. D. Sante, "Fibre optic sensors for structural health monitoring of aircraft composite structures: Recent advances and applications," *Sensors*, vol. 15, pp. 18 666–18 713, 8 Jul. 2015, ISSN: 1424-8220. DOI: 10.3390/s150818666.

[17] M. Mieloszyk, L. Skarbek, M. Krawczuk, W. Ostachowicz, and A. Zak, "Application of fibre bragg grating sensors for structural health monitoring of an adaptive wing," *Smart Materials and Structures*, vol. 20, p. 125 014, 12 Nov. 2011, ISSN: 0964-1726. DOI: 10.1088/0964-1726/20/12/125014.

[18] C. Xu and Z. S. Khodaei, "Shape sensing with rayleigh backscattering fibre optic sensor," *Sensors*, vol. 20, p. 4040, 14 Jul. 2020, ISSN: 1424-8220. DOI: 10.3390/s20144040.

[19] I. Floris, J. M. Adam, P. A. Calderón, and S. Sales, "Fiber optic shape sensors: A comprehensive review," *Optics and Lasers in Engineering*, vol. 139, p. 106 508, Apr. 2021, ISSN: 01438166. DOI: 10.1016/j.optlaseng.2020.106508.

[20] Y. Yamauchi and K. Kishida, "A study of the stability, reliability, and accuracy of neubrescope-based pipe thinning detection system," in *The 3rd International Conference on Structural Health Monitoring of Intelligent Infrastructure*, Nov. 2007.

[21] K. Kishida, C. H. Li, K. Nishiguchi, Y. Yamauchi, A. Guzik, and T. Tsuda, "Hybrid brillouin-rayleigh distributed sensing system," in *OFS2012 22nd International Conference on Optical Fiber Sensors*, Y. Liao, W. Jin, D. D. Sampson, *et al.*, Eds., vol. 8421, Spie, Oct. 2012, 84212g-84212g–4. DOI: 10.1117/12.975668.

[22] K. Hotate, "Recent achievements in bocda/bocdr," in *IEEE SENSORS 2014 Proceedings*, vol. 2014-Decem, Ieee, Nov. 2014, pp. 142–145, ISBN: 978-1-4799-0162-3. DOI: 10.1109/icsens.2014.6984953.

[23] M. Froggatt and J. Moore, "High-spatial-resolution distributed strain measurement in optical fiber with rayleigh scatter," *Applied Optics*, vol. 37, pp. 1735–1740, 10 Apr. 1998, ISSN: 15394522. DOI: 10.1364/ao.37.001735.

[24] X. Tan, A. Abu-Obeidah, Y. Bao, H. Nassif, and W. Nasreddine, "Measurement and visualization of strains and cracks in cfrp post-tensioned fiber reinforced concrete beams using distributed fiber optic sensors," *Automation in Construction*, vol. 124, p. 103 604, Apr. 2021, ISSN: 09265805. DOI: 10.1016/j.autcon.2021.103604.

[25] K. Kishida, H. Zhang, C.-H. Li, A. Guzik, H. Suzuki, and Z. Wu, "Diagnostic of corrosion based thinning in steam pipelines by means of neubrescope high precision optical fiber sensing system," 2005.

[26] A. Piccolo, Y. Lecieux, S. Delepine-Lesoille, and D. Leduc, "Non-invasive tunnel convergence measurement based on distributed optical fiber strain sensing," *Smart Materials and Structures*, vol. 28, p. 045 008, 4 Mar. 2019, ISSN: 1361665x. DOI: 10.1088/1361-665X/ab04cc.

[27] M. Kulpa, T. Howiacki, A. Wiater, T. Siwowski, and R. Sieńko, "Strain and displacement measurement based on distributed fibre optic sensing (dfos) system integrated with frp composite sandwich panel," *Measurement: Journal of the International Measurement Confederation*, vol. 175, p. 109 099, Apr. 2021, ISSN: 02632241. DOI: 10.1016/j.measurement.2021.109099.

[28] Y. Sui, X. Cheng, and J. Wei, "Distributed fibre optic monitoring of damaged lining in double-arch tunnel and analysis of its deformation mode," *Tunnelling and Underground Space Technology*, vol. 110, p. 103 812, Apr. 2021, ISSN: 08867798. DOI: 10.1016/j.tust.2021.103812.

[29] Q. Wu, S. Nair, M. Shuck, E. V. Oort, A. Guzik, and K. Kishida, "Advanced distributed fiber optic sensors for monitoring poor zonal isolation with hydrocarbon migration in cemented annuli," Society of Petroleum Engineers, Sep. 2016, ISBN: 9781613994535. DOI: 10.2118/180329-ms.

[30] M. J. Nicolas, R. W. Sullivan, and W. L. Richards, "Fiber bragg grating strains to obtain structural response of a carbon composite wing," in *ASME 2013 Conference on Smart Materials, Adaptive Structures and Intelligent Systems, SMASIS 2013*, vol. 2, American Society of Mechanical Engineers, 2013, ISBN: 9780791856048. DOI: 10.1115/smasis2013-3265.

[31] L. Richards, A. Parker, W. Ko, and A. Piazza, "Fiber optic wing shape sensing on nasa's ikhana uav," in *Proceedings of the NAVAIR Meeting, Edwards, CA, USA*, 2008.

[32] A. Tessler and J. L. Spangler, "Inverse fem for full-field reconstruction of elastic deformations in shear deformable plates and shells," in *Proceedings of the 2nd European Workshop on Structural Health Monitoring*, Jul. 2004.

[33] A. Tessler and J. L. Spangler, "A least-squares variational method for full-field reconstruction of elastic deformations in shear-deformable plates and shells," *Computer Methods in Applied Mechanics and Engineering*, vol. 194, pp. 327–339, 2-5 Spec. Iss. Feb. 2005, ISSN: 00457825. DOI: 10.1016/j.cma.2004.03.015.

[34] A. Kefal, I. E. Tabrizi, M. Yildiz, and A. Tessler, "A smoothed ifem approach for efficient shape-sensing applications: Numerical and experimental validation on composite structures," *Mechanical Systems and Signal Processing*, vol. 152, p. 107 486, May 2021, ISSN: 10961216. DOI: 10.1016/j.ymssp.2020.107486.

[35] J. Bakalyar and C. Jutte, "Validation tests of fiber optic strain-based operational shape and load measurements," in *53rd AIAA/ASME/ASCE/AHS/ASC Structures, Structural Dynamics and Materials Conference*, American Institute of Aeronautics and Astronautics, Apr. 2012, ISBN: 978-1-60086-937-2. DOI: 10.2514/6.2012-1904.

[36] L. Li, D. Benson, A. Nagy, M. Montanari, N. Petrinic, and S. Hartmann, "Recent developments in isogeometric analysis with solid elements in ls-dyna," in *5th International LS-DYNA Users Conference*, 2018.

[37] W. Szczepinski and J. Miastkowski, "An experimental study of the effect of the prestraining history on the yield surfaces of an aluminium alloy," *Journal of the Mechanics and Physics of Solids*, vol. 16, pp. 153–162, 3 Jun. 1968, ISSN: 0022-5096. DOI: 10.1016/0022-5096(68)90024-0.

[38] P. D. Wu, S. R. MacEwen, D. J. Lloyd, M. Jain, P. Tugcu, and K. W. Neale, "On pre-straining and the evolution of material anisotropy in sheet metals," *International Journal of Plasticity*, vol. 21, pp. 723–739, 4 Apr. 2005, ISSN: 0749-6419. DOI: 10.1016/j.ijplas.2004.05.007.

[39] H. Casquero, L. Liu, Y. Zhang, A. Reali, J. Kiendl, and H. Gomez, "Arbitrary-degree t-splines for isogeometric analysis of fully nonlinear kirchhoff–love shells," *CAD Computer Aided Design*, vol. 82, pp. 140–153, Jan. 2017, ISSN: 00104485. DOI: 10.1016/j.cad.2016.08.009.

[40] Y. Bazilevs, V. M. Calo, J. A. Cottrell, *et al.*, "Isogeometric analysis using t-splines," *Computer Methods in Applied Mechanics and Engineering*, vol. 199, pp. 229–263, 5-8 Jan. 2010, ISSN: 00457825. DOI: 10.1016/j.cma.2009.02.036.

[41] X. Li and T. W. Sederberg, "S-splines: A simple surface solution for iga and cad," *Computer Methods in Applied Mechanics and Engineering*, vol. 350, pp. 664–678, 2019, ISSN: 0045-7825. DOI: https://doi.org/10.1016/j.cma.2019.03.035.

[42] K. A. Johannessen, T. Kvamsdal, and T. Dokken, "Isogeometric analysis using lr b-splines," *Computer Methods in Applied Mechanics and Engineering*, vol. 269, pp. 471–514, Feb. 2014, ISSN: 00457825. DOI: 10.1016/j.cma.2013.09.014.

[43] X. Wei, Y. Zhang, T. J. Hughes, and M. A. Scott, "Truncated hierarchical catmull-clark subdivision with local refinement," *Computer Methods in Applied Mechanics and Engineering*, vol. 291, pp. 1–20, Jul. 2015, ISSN: 00457825. DOI: 10.1016/j.cma.2015.03.019.

[44] X. Wei, Y. J. Zhang, and T. J. Hughes, "Truncated hierarchical tricubic c0 spline construction on unstructured hexahedral meshes for isogeometric analysis applications," *Computers and Mathematics with Applications*, vol. 74, pp. 2203–2220, 9 Nov. 2017, ISSN: 08981221. DOI: 10.1016/j.camwa.2017.07.043.

[45] C. Giannelli, B. Jüttler, S. K. Kleiss, A. Mantzaflaris, B. Simeon, and J. Špeh, "Thb-splines: An effective mathematical technology for adaptive refinement in geometric design and isogeometric analysis," *Computer Methods in Applied Mechanics and Engineering*, vol. 299, pp. 337–365, Feb. 2016, ISSN: 00457825. DOI: 10.1016/j.cma.2015.11.002.

[46] L. Piegl and W. Tiller, *The NURBS Book*. Springer Berlin Heidelberg, 1995, ISBN: 978-3-642-97387-1. DOI: 10.1007/978-3-642-97385-7.

[47] V. P. Nguyen, C. Anitescu, S. P. Bordas, and T. Rabczuk, "Isogeometric analysis: An overview and computer implementation aspects," *Mathematics and Computers in Simulation*, vol. 117, pp. 89–116, October 2017 2015, ISSN: 03784754. DOI: 10.1016/j.matcom.2015.05.008.

[48] E. D. Luycker, D. J. Benson, T. Belytschko, Y. Bazilevs, and M. C. Hsu, "X-fem in isogeometric analysis for linear fracture mechanics," *International Journal for Numerical Methods in Engineering*, vol. 87, pp. 541–565, 6 Aug. 2011, ISSN: 00295981. DOI: 10.1002/nme.3121.

[49] O. R. Bingol and A. Krishnamurthy, "Nurbs-python: An open-source object-oriented nurbs modeling framework in python," *SoftwareX*, vol. 9, pp. 85–94, Jan. 2019, ISSN: 23527110. DOI: 10.1016/j.softx.2018.12.005.

[50] V. P. Nguyen, P. Kerfriden, M. Brino, S. P. Bordas, and E. Bonisoli, "Nitsche's method for two and three dimensional nurbs patch coupling," *Computational Mechanics*, vol. 53, pp. 1163–1182, 6 Dec. 2014, ISSN: 01787675. DOI: 10.1007/s00466-013-0955-3.

[51] K. Kishida, Y. Yamauchi, and A. Guzik, "Study of optical fibers strain-temperature sensitivities using hybrid brillouin-rayleigh system," *Photonic Sensors 2013 4:1*, vol. 4, pp. 1–11, 1 Oct. 2013, ISSN: 2190-7439. DOI: 10.1007/s13320-013-0136-1.

[52] R. Roy, A. Tessler, C. Surace, and M. Gherlone, "Efficient shape sensing of plate structures using the inverse finite element method aided by strain pre-extrapolation," *Thin-Walled Structures*, vol. 180, p. 109 798, Nov. 2022, ISSN: 0263-8231. DOI: 10.1016/j.tws.2022.109798.

[53] A. Kefal and M. Yildiz, "Modeling of sensor placement strategy for shape sensing and structural health monitoring of a wing-shaped sandwich panel using inverse finite element method," *Sensors 2017, Vol. 17, Page 2775*, vol. 17, p. 2775, 12 Nov. 2017, ISSN: 1424-8220. DOI: 10.3390/s17122775.

[54] T. L. Aung, N. Ma, K. Kishida, and A. Guzik, "Advanced structural health monitoring method by integrated isogeometric analysis and distributed fiber optic sensing," *Sensors 2021, Vol. 21, Page 5794*, vol. 21, p. 5794, 17 Aug. 2021. DOI: 10.3390/S21175794.

[55] W. L. Ko, W. L. Richards, and V. t. Tran, "Displacement theories for in-flight deformed shape predictions of aerospace structures," Nasa/tp-2007-214612, 2007.

[56] W. L. Ko, W. L. Richards, V. T. Fleischer, W. L. Richards, and V. T. Fleischer, "Applications of ko displacement theory to the deformed shape predictions of the doubly-tapered ikhana wing," Nasa/tp-2009–214652, 2009.

[57] W. Ko and V. Fleischer, "Further development of ko displacement theory for deformed shape predictions of nonuniform aerospace structures," 2009.

[58] G. Foss and E. Haugse, "Using modal test results to develop strain to displacement transformations," in *Proceedings of the 13th International Conference on Modal Analysis*, 1995.

[59] J. W. Lowdon, K. Eersels, B. van Grinsven, *et al.*, "Displacement field estimation for a two-dimensional structure using fiber bragg grating sensors," *Smart Materials and Structures*, vol. 18, p. 025 006, 2 Jan. 2009, ISSN: 0964-1726. DOI: 10.1088/0964-1726/18/2/025006.

[60] R. Bruno, N. Toomarian, and M. Salama, "Shape estimation from incomplete measurements: A neural-net approach," *Smart Materials and Structures*, vol. 3, p. 92, 2 Jun. 1994, ISSN: 0964-1726. DOI: 10.1088/0964-1726/3/2/002.

[61] Z. Mao and M. Todd, "Comparison of shape reconstruction strategies in a complex flexible structure," *https://doi.org/10.1117/12.775931*, vol. 6932, pp. 127–138, Apr. 2008, ISSN: 0277786x. DOI: 10.1117/12.775931.

[62] A. Tessler, J. L. Spangler, M. Mattone, M. Gherlone, and M. D. Sciuva, "Real-time characterization of aerospace structures using onboard strain measurement technologies and inverse finite element method," NASA Langley Research Center, Sep. 2011.

[63] A. Kefal, E. Oterkus, A. Tessler, and J. L. Spangler, "A quadrilateral inverse-shell element with drilling degrees of freedom for shape sensing and structural health monitoring," *Engineering Science and Technology, an International Journal*, vol. 19, pp. 1299–1313, 3 Sep. 2016, ISSN: 2215-0986. DOI: 10.1016/j.jestch.2016.03.006.

[64] A. Kefal, "An efficient curved inverse-shell element for shape sensing and structural health monitoring of cylindrical marine structures," *Ocean Engineering*, vol. 188, Sep. 2019, ISSN: 00298018. DOI: 10.1016/j.oceaneng.2019.106262.

[65] K. Chen, K. Cao, G. Gao, and H. Bao, "Shape sensing of timoshenko beam subjected to complex multi-node loads using isogeometric analysis," *Measurement*, vol. 184, p. 109 958, Nov. 2021, ISSN: 0263-2241. DOI: 10.1016/j.measurement.2021.109958.

[66] F. Zhao and H. Bao, "An improved inverse finite element method for shape sensing using isogeometric analysis," *Measurement*, vol. 167, p. 108 282, Jan. 2021, ISSN: 0263-2241. DOI: 10.1016/j.measurement.2020.108282.

[67] M. A. Abdollahzadeh, A. Kefal, and M. Yildiz, "A comparative and review study on shape and stress sensing of flat/curved shell geometries using c0-continuous family of ifem elements," *Sensors 2020, Vol. 20, Page 3808*, vol. 20, p. 3808, 14 Jul. 2020, ISSN: 1424-8220. DOI: 10.3390/s20143808.

[68] M. Li, A. Kefal, E. Oterkus, and S. Oterkus, "Structural health monitoring of an offshore wind turbine tower using ifem methodology," *Ocean Engineering*, vol. 204, p. 107 291, 2020, ISSN: 0029-8018. DOI: https://doi.org/10.1016/j.oceaneng.2020.107291.

[69] M. Gherlone, P. Cerracchio, M. Mattone, M. D. Sciuva, and A. Tessler, "Shape sensing of 3d frame structures using an inverse finite element method," *International Journal of Solids and Structures*, vol. 49, pp. 3100–3112, 22 Nov. 2012, ISSN: 0020-7683. DOI: 10.1016/j.ijsolstr.2012.06.009.

[70] M. Gherlone, P. Cerracchio, and M. Mattone, "Shape sensing methods: Review and experimental comparison on a wing-shaped plate," *Progress in Aerospace Sciences*, vol. 99, pp. 14–26, May 2018, ISSN: 0376-0421. DOI: 10.1016/j.paerosci.2018.04.001.

[71] A. Kefal and E. Oterkus, "Isogeometric ifem analysis of thin shell structures," *Sensors*, vol. 20, p. 2685, 9 May 2020, ISSN: 1424-8220. DOI: 10.3390/s20092685.

[72] F. Zhao, L. Xu, H. Bao, and J. Du, "Shape sensing of variable cross-section beam using the inverse finite element method and isogeometric analysis," *Measurement*, vol. 158, p. 107 656, Jul. 2020, ISSN: 0263-2241. DOI: 10.1016/j.measurement.2020.107656.

[73] T. L. Aung, N. Ma, K. Kishida, and F. Lu, "Unified inverse isogeometric analysis and distributed fiber optic strain sensing for monitoring structure deformation and stress," *Applied Mathematical Modelling*, vol. 120, pp. 733–751, Aug. 2023, ISSN: 0307-904X. DOI: 10.1016/J.APM.2023.04.013.

[74] C. Giannelli, B. Jüttler, and H. Speleers, "Thb-splines: The truncated basis for hierarchical splines," in *Computer Aided Geometric Design*, vol. 29, North-Holland, Oct. 2012, pp. 485–498. DOI: 10.1016/j.cagd.2012.03.025.

[75] T. L. Aung, N. Ma, Y. Okitsu, S. Hayashi, K. Takada, and T. Naito, "Measurement and modelling of strain-path dependent anisotropic hardening behaviors of high strength steels subjected to pre-strains," *Journal of Materials Research and Technology*, vol. 23, pp. 451–465, Mar. 2023, ISSN: 2238-7854. DOI: 10.1016/j.jmrt.2023.01.010.

[76] L. Sun and R. H. Wagoner, "Proportional and non-proportional hardening behavior of dual-phase steels," *International Journal of Plasticity*, vol. 45, pp. 174–187, Jun. 2013, ISSN: 0749-6419. DOI: 10.1016/j.ijplas.2013.01.018.

[77] Q. Hu and J. W. Yoon, "Anisotropic distortional hardening based on deviatoric stress invariants under non-associated flow rule," *International Journal of Plasticity*, vol. 151, p. 103 214, Apr. 2022, ISSN: 0749-6419. DOI: 10.1016/j.ijplas.2022.103214.

[78] H. Kim, F. Barlat, Y. Lee, S. B. Zaman, C. S. Lee, and Y. Jeong, "A crystal plasticity model for describing the anisotropic hardening behavior of steel sheets during strain-path changes," *International Journal of Plasticity*, vol. 111, pp. 85–106, Dec. 2018, ISSN: 07496419. DOI: 10.1016/j.ijplas.2018.07.010.

[79] E. F. Rauch, J. J. Gracio, F. Barlat, and G. Vincze, "Modelling the plastic behaviour of metals under complex loading conditions," *Modelling and Simulation in Materials Science and Engineering*, vol. 19, p. 035 009, 3 Mar. 2011, ISSN: 1361651x. DOI: 10.1088/0965-0393/19/3/035009.

[80] M. F. Vieira, J. H. Schmitt, J. J. Gracio, and J. V. Fernandes, "The effect of strain path change on the mechanical behaviour of copper sheets," *Journal of Materials Processing Technology*, vol. 24, pp. 313–322, C Dec. 1990, ISSN: 0924-0136. DOI: 10.1016/0924-0136(90)90192-w.

[81] J. V. Fernandes, D. M. Rodrigues, L. F. Menezes, and M. F. Vieira, "A modified swift law for prestrained materials," *International Journal of Plasticity*, vol. 14, pp. 537–550, 6 1998, ISSN: 07496419. DOI: 10.1016/s0749-6419(98)00027-8.

[82] F. Yoshida, H. Hamasaki, and T. Uemori, "A model of anisotropy evolution of sheet metals," *Procedia Engineering*, vol. 81, pp. 1216–1221, Jan. 2014, ISSN: 1877-7058. DOI: 10.1016/j.proeng.2014.10.100.

[83] F. Yoshida, H. Hamasaki, and T. Uemori, "A user-friendly 3d yield function to describe anisotropy of steel sheets," *International Journal of Plasticity*, vol. 45, pp. 119–139, Jun. 2013, ISSN: 0749-6419. DOI: 10.1016/j.ijplas.2013.01.010.

[84] Z. He, K. Zhang, Y. Lin, and S. Yuan, "An accurate determination method for constitutive model of anisotropic tubular materials with dic-based controlled biaxial tensile test," *International Journal of Mechanical Sciences*, vol. 181, p. 105 715, Sep. 2020, ISSN: 0020-7403. DOI: 10.1016/j.ijmecsci.2020.105715.

[85] H. Aretz, "A non-quadratic plane stress yield function for orthotropic sheet metals," *Journal of Materials Processing Technology*, vol. 168, pp. 1–9, 1 Sep. 2005, ISSN: 0924-0136. DOI: 10.1016/j.jmatprotec.2004.10.008.

[86] R. Larsson, O. Björklund, L. Nilsson, and K. Simonsson, "A study of high strength steels undergoing non-linear strain paths—experiments and modelling," *Journal of Materials Processing Technology*, vol. 211, pp. 122–132, 1 Jan. 2011, ISSN: 0924-0136. DOI: 10.1016/j.jmatprotec.2010.09.004.

[87] W. Hu, "Constitutive modeling of orthotropic sheet metals by presenting hardening-induced anisotropy," *International Journal of Plasticity*, vol. 23, pp. 620–639, 4 Apr. 2007, ISSN: 0749-6419. DOI: 10.1016/j.ijplas.2006.08.004.

[88] H. Haddadi, S. Bouvier, M. Banu, C. Maier, and C. Teodosiu, "Towards an accurate description of the anisotropic behaviour of sheet metals under large plastic deformations: Modelling, numerical analysis and identification," *International Journal of Plasticity*, vol. 22, pp. 2226–2271, 12 Dec. 2006, ISSN: 0749-6419. DOI: 10.1016/j.ijplas.2006.03.010.

[89] A. N. Suprun, "A constitutive model with three plastic constants: The description of anisotropic workhardening," *International Journal of Plasticity*, vol. 22, pp. 1217–1233, 7 Jul. 2006, ISSN: 0749-6419. DOI: 10.1016/j.ijplas.2005.07.007.

[90] J. Qin, B. Holmedal, and O. S. Hopperstad, "A combined isotropic, kinematic and distortional hardening model for aluminum and steels under complex strain-path changes," *International Journal of Plasticity*, vol. 101, pp. 156–169, Feb. 2018, ISSN: 07496419. DOI: 10.1016/j.ijplas.2017.10.013.

[91] F. Barlat, J. J. Gracio, M. G. Lee, E. F. Rauch, and G. Vincze, "An alternative to kinematic hardening in classical plasticity," *International Journal of Plasticity*, vol. 27, pp. 1309–1327, 9 Sep. 2011, ISSN: 07496419. DOI: 10.1016/j.ijplas.2011.03.003.

[92] W. J. He, S. H. Zhang, and H. W. Song, "An extended homogenous yield function based anisotropic hardening model for description of anisotropic hardening behavior of materials," *International Journal of Mechanical Sciences*, vol. 77, pp. 343–355, 1-2 Dec. 2013, ISSN: 0020-7403. DOI: 10.1016/j.ijmecsci.2013.05.018.

[93] F. Barlat, J. Ha, J. J. Grácio, M. G. Lee, E. F. Rauch, and G. Vincze, "Extension of homogeneous anisotropic hardening model to cross-loading with latent effects," *International Journal of Plasticity*, vol. 46, pp. 130–142, Jul. 2013, ISSN: 0749-6419. DOI: 10.1016/j.ijplas.2012.07.002.

[94] J. Lee, H. J. Bong, D. Kim, and M. G. Lee, "Modeling differential permanent softening under strain-path changes in sheet metals using a modified distortional

hardening model," *International Journal of Plasticity*, vol. 133, p. 102 789, 12 Oct. 2020, ISSN: 0749-6419. DOI: 10.1016/j.ijplas.2020.102789.

[95] R. Hill, "A theory of the yielding and plastic flow of anisotropic metals," May 1948, pp. 281–297. DOI: 10.1098/rspa.1948.0045.

Publications

Journal papers

1. T. L. Aung, N. Ma, K. Kishida, *et al.*, "Advanced structural health monitoring method by integrated isogeometric analysis and distributed fiber optic sensing," *Sensors 2021, Vol. 21, Page 5794*, vol. 21, p. 5794, 17 Aug. 2021. DOI: 10.3390/S21175794
2. T. L. Aung, N. Ma, K. Kishida, *et al.*, "Unified inverse isogeometric analysis and distributed fiber optic strain sensing for monitoring structure deformation and stress," *Applied Mathematical Modelling*, vol. 120, pp. 733–751, Aug. 2023, ISSN: 0307-904X. DOI: 10.1016/J.APM.2023.04.013
3. T. L. Aung, N. Ma, Y. Okitsu, *et al.*, "Measurement and modelling of strain-path dependent anisotropic hardening behaviors of high strength steels subjected to pre-strains," *Journal of Materials Research and Technology*, vol. 23, pp. 451–465, Mar. 2023, ISSN: 2238-7854. DOI: 10.1016/j.jmrt.2023.01.010

Conference presentations

1. T. L. Aung, S. Matsumoto, N. Ma, *et al.*, "Integrated method of inverse isogeometric analysis and distributed fiber optic strain for monitoring structure deformation and stress," WCCM-APCOM, Jul. 2022, p. 1632
2. T. L. Aung, N. Ma, K. Nakao, *et al.*, "Visualization and estimation of deformation for an impeller plate by inverse isogeometric analysis and fiber optic strain sensing," Visual-JW, 2022
3. T. L. Aung, N. Ma, Y. Okitsu, *et al.*, "Measurement and modelling of pre-strain dependent anisotropic hardening behaviors of steel," JSTP, 2022, pp. 271–272

Acknowledgments

Firstly, I would like to thank my supervisor, Prof. Ninshu Ma for his unwavering support and kindness throughout the course of my study. He has been a great help in providing me with the necessary guidance and knowledge to complete this research. I would also like to thank the Professors and researchers at Ma Lab and the Department of Naval Architecture and Ocean Engineering for their critical feedback of my work. Especially, I am grateful to Prof. Serizawa and Prof. Narasaki for their insightful feedback in the lab meetings, Prof. Rashed for his advice during the initial research, Prof. Osawa for his continuum mechanics class, and Prof. Fujikubo for his academic advice. I would like to express my sincere gratitude to the Head of Department, Prof. Iijima, the secretary Ms. Nakamura, and the former secretary Ms. Takemasa for their invaluable help during my five year study in Osaka University.

I am deeply indebted to my friends and family for their love, encouragement, and moral support during this challenging period.

My heartfelt thanks also go to the funding agency, MEXT for their scholarship that enabled me to purse my academic studies without the financial burden.

I would also like to extend my appreciation to the open-source community for their contributions and providing me with free access to numerous resources and tools that were instrumental to this research. Among them, I would like to thank the developers of the following software packages: *nurbs Octave*, *igafem*, *NURBS-Python*, *FoBis*, *Inkscape*, *ParaView*, and the numerous Python packages which are too many to mention here. I hope to give back to the community in the future.

I would like express my gratitude to Dr. Derek Muller and Dr. Sabine Hossenfelder for their educational videos on YouTube. Their videos have been a great source of motivation and inspiration for me.